Scattering and near field properties of plasmonic na-noparticles for light harvesting in thin film solar cells

Ulriksen, Hans Ulrik

Publication date:
2020

Document Version
Publisher's PDF, also known as Version of record

SCATTERING AND NEAR FIELD PROPERTIES OF PLASMONIC NANOPARTICLES FOR LIGHT HARVESTING IN THIN FILM SOLAR CELLS

BY
HANS ULRIK ULRIKSEN

DISSERTATION SUBMITTED 2020

AALBORG UNIVERSITY
DENMARK

Scattering and near field properties of plasmonic nanoparticles for light harvesting in thin film solar cells

PhD Thesis in Physics

Hans Ulrik Ulriksen

Department of Materials and Production
Aalborg University
Skjernvej 4
DK-9220 Aalborg

Dissertation submitted: February 2020

PhD supervisor: Prof. Kjeld Pedersen
Aalborg University

PhD committee: Associate Professor Leonid Gurevich (chairman)
Aalborg University

Associate Professor Morten Madsen
Southern University of Denmark

Professor, Dr. Kurt Hingerl
Johannes Kepler University Linz

PhD Series: Faculty of Engineering and Science, Aalborg University

Department: Department of Materials and Production

ISSN (online): 2446-1636
ISBN (online): 978-87-7210-554-3

Published by:
Aalborg University Press
Langagervej 2
DK – 9220 Aalborg Ø
Phone: +45 99407140
aauf@forlag.aau.dk
forlag.aau.dk

Printed in Denmark by Rosendahls, 2020

Thesis Title:	Scattering and near field properties of plasmonic nanoparticles for light harvesting in thin film solar cells
Ph.D. Student:	Hans Ulrik Ulriksen
Supervisor:	Prof. Kjeld Pedersen, Aalborg University

List of published papers.

[A] **Ulriksen, H. U.**, & Pedersen, K. (2016). Field enhancement at silicon surfaces by gold ellipsoids probed by optical second-harmonic generation spectroscopy. Journal of Applied Physics, 120(23), [235307]. https://doi.org/10.1063/1.4972190

[B] **Ulriksen, H. U.**, Søndergaard, T. M., Pedersen, T. G., & Pedersen, K. (2019). Plasmon enhanced light scattering into semiconductors by aperiodic metal nanowire arrays. Optics Express, 27, 14308-14320. https://doi.org/10.1364/OE.27.014308

In addition to the main papers, the following publications have also been made.

[C] Villesen, T. F., Uhrenfeldt, C., Johansen, B., Hansen, J. L., **Ulriksen, H. U.**, & Larsen, A. N. (2012). Aluminum nanoparticles for plasmon-improved coupling of light into silicon. Nanotechnology, 23(8), 23. https://doi.org/10.1088/0957-4484/23/8/085202

[D] Johansen, B., Uhrenfeldt, C., Larsen, A. N., Pedersen, T. G., **Ulriksen, H. U.**, Kristensen, P. K., ... Pedersen, K. (2011). Optical transmission through two-dimensional arrays of Beta-Sn nanoparticles. Physical Review B (Condensed Matter and Materials Physics), 84(11), 113405. https://doi.org/10.1103/PhysRevB.84.113405

This thesis has been submitted for assessment in partial fulfillment of the PhD degree. The thesis is based on the submitted or published scientific papers which are listed above. Parts of the papers are used directly or indirectly in the extended summary of the thesis. As part of the assessment, co-author statements have been made available to the assessment committee and are also available at the Faculty. The thesis is not in its present form acceptable for open publication but only in limited and closed circulation as copyright may not be ensured.

Typeset in LaTeX 2ε by the author.

Abstract

Metallic nanoparticles have been heavily studied in the last decade and one of the motivation for that is their possible application with thin film solar cell in order to increase the absorption of incoming solar energy. To achieve this, gaining a deeper understanding of the physical features of metallic nanoparticles is very important. With this in mind, the focus of this thesis is the interaction between light and metallic nanoparticles on a semiconductor surface, with special focus on scattering profile and near field effects.

A technique for direct measurement and analysis of light scattering from nanostructures on a surface was presented and demonstrated. In this work the technique is exemplified with aperiodic patterns of Ag strips placed on a GaAs substrate. Modelling of the complex pattern of scattered light agrees with the experimental results to a very detailed level and, most importantly, it allows for a verification of the angular scattering profile of a single scatterer.

The field enhancements from Au and Ag nanoparticles on a silicon substrate were determined from optical second harmonic generation spectroscopy. Both Au and Ag particles of varying sizes were deposited on a Si substrate passivated by a 1 nm thick surface oxide. Linear optical spectra were measured and modelled to extract the linear properties of the nanoparticles, including the plasmon resonances. Second harmonic generation spectroscopy from these systems shows resonances from the metal particles and the silicon/oxide substrate. The field enhancement at the Si surface was modelled by following the evolution of the Si E_1 resonance for different size of particles. The effect of both the Au and the Ag particles at the E_1 resonance can be explained by a combination of tunneling effects and optical field enhancement at the surface of the Si substrate.

Resumé

Metalliske nanopartikler er blevet undersøgt meget i det sidste årti, og en af motivationerne er deres mulige anvendelse med tyndfilms solceller for at øge absorptionen af solenergien. For at opnå dette er det meget vigtigt at få en dybere forståelse af de fysiske egenskaber ved metalliske nanopartikler. Med dette i tankerne er fokusset på denne afhandling, interaktionen mellem lys og metalliske nanopartikler på en halvlederoverflade med særligt fokus på spredingsprofil og nærfeltseffekter.

En teknik til direkte måling og analyse af lysspredning fra nanostrukturer på en overflade er blevet præsenteret og demonstreret. I dette arbejde er teknikken eksemplificeret med aperiodiske strukturer af Ag-striber placeret på et GaAs-substrat. Modellering af det komplekse mønster af spredt lys er på et meget detaljeret niveau i overensstemmelse med de eksperimentelle resultater, og specielt vigtigt er det, at det er muligt at verificere vinkelspredningsprofilen for en enkelt partikel.

Optisk anden harmonisk generation (SHG) spektroskopi er blevet brugt til at bestemme feltforstærkninger fra Au og Ag nanopartikler på et siliciumsubstrat. Au- og Ag-partikler af forskellig størrelse er blevet deponeret på et Si-substrat passiveret af et 1 nm tykt overfladeoxid. Lineære optiske spektre måles og modelleres for at ekstrahere de lineære egenskaber af nanopartiklerne, herunder plasmonresonanserne. SHG spektroskopi fra disse systemer viser resonanser fra metalpartiklerne og silicium/oxid substratet. Ved at følge udviklingen af Si E_1 resonansen med størrelsen af partiklerne er feltforstærkningen i Si-overfladen modelleret. Virkningen af både Au og Ag partiklerne ved E_1 resonansen er en kombination af ladningsoverførsel og en forstærkning af det optiske felt ved overfladen af Si-substratet.

Contents

Chapter 1

Introduction

1.1 Motivation

The atmospheric carbon dioxide (CO_2) level is at the highest level in 420000 years [1] and together with other greenhouse gases it has a negative effect on the Earth's climate. One is global temperature rise, which again leads to increasing ocean temperatures, shrinking ice sheets, rising sea level and higher number of extreme weather events. The International Panel on Climate Change (IPCC) recommend a 45% reduction in human-caused CO_2 emission from 2010 levels by 2030, reaching net zero around 2050 [2]. One way to achieve this goal is to switch to emission-free energy sources. Lowering the cost of CO_2 emission free energy sources would help reaching those optimistic guidelines.

One of CO_2 emission free energy sources is solar energy. Its potential is vast as only a fraction of the total energy delivered by the sun can cover the global energy consumption for a foreseeable future [3]. One method to harvest solar energy is through photo voltaic (PV) systems where the energy is converted directly to electricity. PVs contain no movable part and can be produced of materials which are abundant on Earth. Thus it has the potential to be low maintenance, long life and low cost, thereby playing a significant role in the transition to emission free energy.

For PVs to play a large role in the global energy production, the price of the produced energy must be comparable or lower than other conventional energy sources. At first, subsidies by political programs have minimized the prize difference and greatly reduced the price through scale of production [4]. As of presently, silicon PVs are the dominant type of panels installed, and material cost still constitutes sizable part of the total cost [5], with the silicon (Si) absorbing layer being the most expensive component.

Thin film solar cells are the immediate way to reduce the material cost of a solar panel. Unfortunately, reducing the absorption layer thickness also reduces the efficiency of the cell to a degree where the cost of installation exceeds that of a standard cell. One method to increase the efficiency is inspired by the patterning of standard thick solar cells to scatter the incidence light into the cell at an angle, and thereby increasing the optical path-length in the absorbing material [6, 7]. The textures on standard cell are typically around 10 μm in size, which is not suitable on a thin film cells with a thickness of 1-2 μm. Instead, it was proposed to use metallic nanoparticles to scatter light and achieve light trapping in thin film cells[6]. When dealing with nanoparticles and Si, light-matter interactions and bulk and interface effects are primordial to investigate.

1.2 Objective

The objective of this project is to obtain a better understanding of the interaction between light and metallic nanoparticles on a semiconductor surface. The project can be divided into three main goals:

- to investigate the scattering properties and in particular the angular distribution of scattered light from a single nanoparticle, in order to verify theoretical models.
- to investigate how metallic nanoparticles affects the electronic properties of the substrate, with special focus on the strong near-field effect of the particles.
- to fabricate nanoparticles on test solar cells using e-beam lithography, with the purpose of testing specific particle parameters.

1.3 Approaches

Different approaches have been used in this work to reach the objectives named previously. The investigations of scattering properties and near-field effects, are preformed by optical methods and scanning electron microscopy (SEM). Optical second harmonic generation (SHG) is a non-linear process which is very surface sensitive, and ideally suited for investigating particle and near-field effects. Linear optical reflection and transmission spectroscopy has a

solid theoretical foundation and is primarily used to assist in the interpretation of the SHG. SEM is used to obtain information of particle size, shape and coverage. The angular scattering profile is addressed with an angle scanning setup.

Fabrication of the metallic nanoparticles is done by two methods, namely Electron beam lithography (EBL) and metal deposition. The use of EBL allows for an excellent control of the shape and position of metallic particles, enabling a variety of experiments with precise control of sample parameters. EBL is time consuming and expensive, thus only used when particle geometry and position is critical. Experiments with lower demands on exact particle size and position, the method of metal deposition at high temperature are used to form nanoparticles. With this method the particles self-assembles on the surface, were the size and shape are governed by temperature, deposition rate and type of material.

1.4 Outline

Chapter 2 gives an overview of thin film solar cells and plasmonics in order to bring this work into perspective. Chapter 3 introduces the theory behind second harmonic generation and spectroscopy, linear spectroscopy and contains a quick summary of the properties of bulk silicon. Chapter 4 presents the sample fabrication techniques used in this work. Chapter 5 relates to unpublished experimental work on SHG spectroscopy of Ag nanoparticles on silicon. A summary concludes the work in chapter 6. All published articles are included as appendices.

References

1. Petit, J. *et al.* Climate and atmospheric history of the past 420,000 years from the Vostok ice core, Antarctica. *NATURE* **399,** 429–436. ISSN: 0028-0836 (6 1999).
2. *IPCC Fifth Assessment Report, Summary for Policymakers.* `https://www.ipcc.ch/2018/10/08/summary-for-policymakers-of-ipcc-special-report-on-global-warming-of-1-5c-approved-by-governments/`.

3. Moriarty, P. & Honnery, D. What is the global potential for renewable energy? *Renewable and Sustainable Energy Reviews* **16,** 244–252. ISSN: 1364-0321 (2012).

4. *Lazard's Levelized Cost of Energy*. https://www.lazard.com/perspective/levelized-cost-of-energy-and-levelized-cost-of-storage-2018/.

5. Green, M. A. Commercial progress and challenges for photovoltaics. *NATURE ENERGY* **1.** ISSN: 2058-7546 (1 2016).

6. Pillai, S., Catchpole, K. R., Trupke, T. & Green, M. A. Surface plasmon enhanced silicon solar cells. *Journal of Applied Physics* **101,** 093105 (2007).

7. Catchpole, K. R. & Polman, A. Design principles for particle plasmon enhanced solar cells. *APPLIED PHYSICS LETTERS* **93.** ISSN: 0003-6951 (10 2008).

Chapter 2

Thin film solar cells and plasmonics

2.1 Introduction

The work presented in this thesis has been motivated by the overall goal of reducing the price of solar cells by improving the absorption properties of thin film solar cells. Plasmonics effects have been suggested as possible solution for increasing absorption of such solar cells. This chapter contains a brief introduction to silicon photovoltaic and localized surface plasmons.

2.2 Silicon photovoltaics

Silicon (Si) has been used for decades to make solar cells and righteously so, as its optical and electrical properties are well suited for light conversion and it is an abundant material on Earth. Moreover, it is non-toxic and a lot of the fabrication methods overlap with the electronics industry.

The basic working principle behind solar cells is quite simple and can be outlined roughly as follows. A photon with sufficient energy excites an electron, and thereby create an electron-hole pair. The high energy electron is then separated from the hole by an internal electric field and led out of the solar cell, where it releases the energy, only then to return to the solar cell an recombine with the hole.

Figure 2.1 show a sketch of a basic solar cell based on a Si p-n junction. Si can be doped with group III or V atoms to provide an excess of free holes

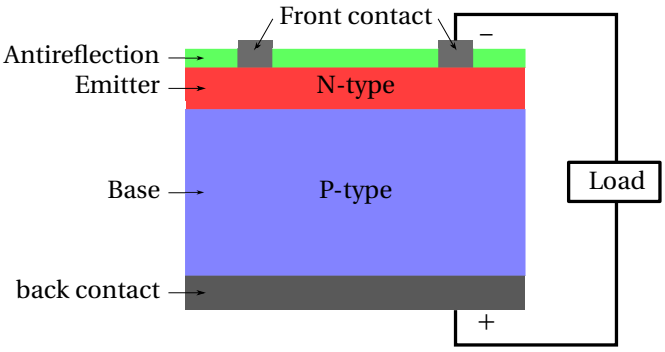

Figure 2.1: Sketch of a p-n junction Si solar cell.

or electrons in the material, called majority carriers. Holes in n-type materials and electrons in p-type materials are called minority carriers. A p-n junction is p-type and n-type Si brought in contact. There is an interchange of free charges from both sides of the interface via diffusion, leaving behind stationary ionized atoms which create an electric field opposing the diffusion. With continued diffusion the electric field will continue to grow until equilibrium. This volume where free carriers have been removed is called the "depletion zone" and it provides the electric field used to separate the electron-hole pair by driving the minority carriers to cross the junction while preventing the majority carriers to do so. Thus, when an electron-hole pair is created, whether in n-type or in p-type regions, the minority carrier is free to cross the barrier. The quality of the Si crystal used in a solar cell must be high and thus rather expensive. Defects and impurities in the material act as traps for minority carriers and greatly reduces the efficiency of the cell. This is also true for interfaces and surfaces in the solar cell.

Absorption in silicon solar cells

Silicon is a semiconductor material with a direct bandgap of ∼3.4 eV and an indirect bandgap of ∼1.1 eV. This means that all photons under 1.1 eV are not absorbed and in order to absorp a photon with an energy between 1.1 eV and 3.4 eV it must be assisted by a phonon to conserve momentum. The probability of a photon-phonon coupling is low and a relatively thick layer of silicon is needed to get a reasonable absorption. This i why modern Si solar cells, even with good light trapping methods, have a Si thickness of about 180 μm [1].

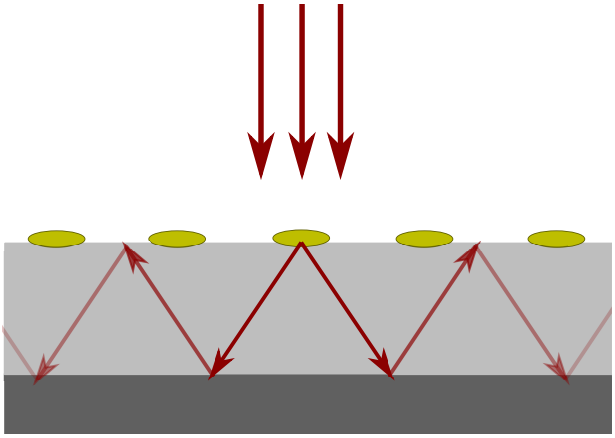

Figure 2.2: Light trapping mechanism in thin film solar cell by metallic nanoparticles on the surface.

For thin-film solar cells where the active region has a thickness of 1-2 μm, the absorption is greatly reduced especially at long wavelengths. To increase absorption a method of light-trapping in must be implemented. A proposed method is the use of metallic nanostructures that support surface plasmons. The main idea is for the nanostructures to facilitate the coupling of light into the thin film structure and use the plasmon resonance to maximize the coupling. The principle is shown in Fig 2.2, illustrating light scattered into an angle above the critical angle and thus trapping the light inside the solar cell. The enhanced coupling light into the semiconductor films was first discovered by Stuart and Hall when investigating photodetectors [2] and then resurfaced a decade later in connection with solar cells [3]. In addition, it was suggested that the strong near field around a nanoparticle at resonance could allow direct absorption of photons below the direct bandgap [4]. However in particular for Si cells the effect is found to be very small [5] or leads to ohmic loses in the nanoparticles [6].

2.3 Localized surface plasmons

Surface plasmons are the collective oscillation of free electrons on the surface of a metal, driven by e.g. the electric field of light incident on the surface. When

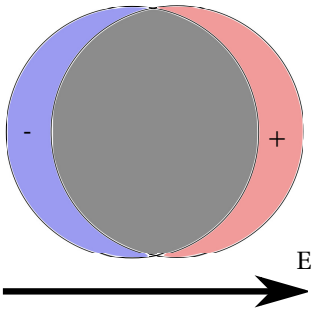

Figure 2.3: Illustration of localized plasmon.

the oscillations occur on the surface of a small particle, it is called a localized surface plasmon (LSP). As illustrated in Fig. 2.3, when the electrons are moved away from their equilibrium position it exposes stationary ionized atoms of the particle creating an electric field in the material, which opposes the external electric field and works as a restoring force on the electrons. A system with a restoring force and inertia can oscillate and it will have a resonance frequency. At resonance, the electrons at the surface react strongly to the external field and the movement may induce intense electric fields.

Rayleigh approximation

When the particles are much smaller than the wavelength of the light, the external electric field can be assumed constant across the particles and is referred to as the Rayleigh (dipole) approximation. Within this approximation the electric field inside and outside a spherical particle can be calculated as [7]

$$\mathbf{E_{in}} = \mathbf{E_0} \frac{3\epsilon_d}{\epsilon_m + 2\epsilon_a} \tag{2.1}$$

$$\mathbf{E_{out}} = \mathbf{E_0} + \frac{3\mathbf{n}(\mathbf{n}\cdot\mathbf{p}) - \mathbf{p}}{4\pi\epsilon_0\epsilon_a r^3} \tag{2.2}$$

where $\mathbf{E_0}$ is the external field, $\mathbf{n}$ is the unit vector pointing from the particle to the observation point and r is the distance between them. ϵ_0 is the dielectric constant of free space, ϵ_a and ϵ_m are the complex dielectric functions of the surrounding material and metal, respectively. $\mathbf{p}$ is the polarization of the

particle and is defined as

$$\mathbf{p} = \epsilon_0 \epsilon_a \alpha \mathbf{E_0} \tag{2.3}$$

where α is the polarizability of the particle, which for a spherical particle is calculated as

$$\alpha = 4\pi a^3 \frac{\epsilon_m - \epsilon_a}{\epsilon_m + 2\epsilon_a} \tag{2.4}$$

where a is the particle radius. From Eq. 2.1 and 2.4 it follows that resonance occurs when $\epsilon_m(\omega) = -2\epsilon_a(\omega)$. Both ϵ_m and ϵ_a are frequency dependent and complex, thus the real part determines the resonance frequency and the imaginary part limits the amplitude. For materials such as silver and gold, resonance occurs where the imaginary part is small and large plasmonic effects can be observed.

Ellipsoidal particles on a surface were studied in this work and in this particular case, the polarizability is modified by including a geometrical factor M_i and is, within the dipole approximation, expressed as

$$\alpha_i = \frac{4\pi a b c}{3} \frac{\epsilon_a(\epsilon_m - \epsilon_a)}{[\epsilon_a + M_i(\epsilon_m - \epsilon_a)]}. \tag{2.5}$$

where $i = x, y, z$ and a, b and c are the semi axes of the ellipsoid. M also includes effect of the substrate and will, because of geometry and surroundings, depend highly on direction, leading to three contributions. As for the spherical case, resonance conditions occur when the denominator of Eq. 2.5 is zero. From Eq. 2.5, it can be shown that both particle shape and surroundings can be used to move the plasmon resonance of a particle. In general, increasing the aspect ratio of the particle or the refractive index of the surrounding media, will red shift the resonance [8].

The scattering and absorption properties can also be calculated via the particle polarizability. For small particles with respect to the wavelength of the incoming light, the scattering and absorption cross sections are given by

$$C_{scat} = \frac{1}{6\pi} \left(\frac{2\pi}{\lambda} \right)^2 |\alpha|^2 \tag{2.6}$$

$$C_{abs} = \frac{2\pi}{\lambda} \mathrm{Im}[\alpha] \tag{2.7}$$

where λ is the wavelength of the incident light. The polarizability increases

with the volume of the particles (see Eq. 2.5), thus the absorption will dominate for small particles and scattering will take over when the particles grow in size. The particle size for which this transition occur, depends on both particle material and surrounding media. For metals such as Ag and Au, studies have shown that for disk shaped particles scattering dominates for diameters above 100 nm and 140 nm, respectively [9]. Such dimensions is in the vicinity of the limits of the dipole approximation and dynamic depolarization and radiation dampening effects must be considered by renormalizing the polarizability [10, 11].

2.3.1 Scattering properties of nanoparticles

Two remarkable features of nanoparticles on (or close to) a surface are presented in Fig. 2.4, where subfigure (a) is a reprint from paper B and are calculated using the Green's function surface integral equation method (GFSIEM) [12]. The sample used to produce the results shown in Fig. 2.4 is a single silver wire on a GaAs substrate.

The scattering cross section, i.e., the total scattered power normalized to the incident power per unit area, is shown in Fig. 2.4 (a) as a function of strip width. By normalizing the scattering cross section with the strip width plasmon resonances can be identified. The resonances are due to the excitation of surface plasmon polaritons propagating back and forth across the Ag strips (along x) and being reflected at the strip edges. This leads to standing-wave resonances when the total round-trip propagation and reflection phase is an integer multiple of 2π. The peaks in Fig. 2.4 (a) are due to excitation of the 1st and 3rd order standing-wave resonances. The 2nd order resonance cannot be excited when using normally incident light due to symmetry considerations [12].

Figure 2.4 (b) shows scattered radiation pattern (or differential scattering cross section) for a 130-nm-wide silver strip on a GaAs substrate. Most of the scattered light goes into the semiconductor substrate, which is a consequence of the large refractive index of GaAs compared with air [12]. In addition, a large fraction of the scattered light is at angles that are above the critical angle of the GaAs-Air interface (red solid line), thus trapping the light inside the GaAs which can be useful in thin film solar cells.

The radiation pattern in Fig. 2.4 (b) is not seen exclusively for plasmonic metal particles, but are a general characteristic for small particles on or close

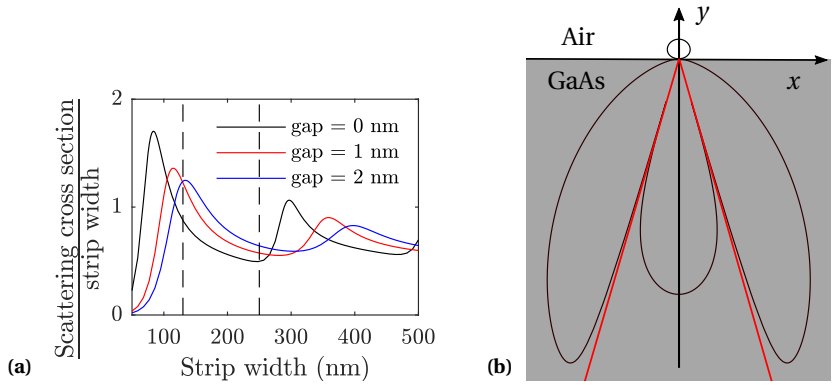

Figure 2.4: (a) (Reprint from paper B) Scattering cross section as a function of strip width for 3 different gap sizes. (b) Scattering per unit angle into both air and substrate for a 130 nm strip. The red solid lines represent the critical angle of the GaAs-Air interface.

to a surface. in this case the strip width is significantly smaller than the wavelength, and the radiation pattern is similar to that of a dipole [12]. The advantage of plasmonic structures is the increased scattering cross section at resonance, enabling them to scatter a larger part of the incidence light than the geometrical area would suggest.

2.4 Summary

This chapter has introduced the basic principle behind silicon photovoltaics and plasmonics that originally motivated the work presented in this thesis. Scattering properties of nanoparticles, including scattering cross section and scattering into a substrate, were also introduced.

References

1. *Photovoltaics Report* *(Fraunhofer Institute for Solar Energy Systems, 2015)* `https://www.ise.fraunhofer.de/content/dam/ise/de/documents/publications/studies/Photovoltaics-Report.pdf`.

2. Stuart, H. R. & Hall, D. G. Absorption enhancement in silicon-on-insulator waveguides using metal island films. *Applied Physics Letters* **69,** 2327–2329 (1996).

3. Schaadt, D. M., Feng, B. & Yu, E. T. Enhanced semiconductor optical absorption via surface plasmon excitation in metal nanoparticles. *Applied Physics Letters* **86,** 063106 (2005).

4. Kirkengen, M., Bergli, J. & Galperin, Y. M. Direct generation of charge carriers in c-Si solar cells due to embedded nanoparticles. *Journal of Applied Physics* **102,** 093713 (2007).

5. Jung, J., Trolle, M. L., Pedersen, K. & Pedersen, T. G. Indirect near-field absorption mediated by localized surface plasmons. *Phys. Rev. B* **84,** 165447 (16 Oct. 2011).

6. Spinelli, P. *et al.* Plasmonic light trapping in thin-film Si solar cells. *Journal of Optics* **14,** 024002 (2012).

7. Bohren, C. F. & Huffman, D. R. *Absorption and Scattering of Light by Small Particles* (Wiley Interscience, 1983).

8. Lance Kelly, K., Coronado, E., Zhao, L. L. & Schatz*, G. C. The Optical Properties of Metal Nanoparticles: The Influence of Size, Shape, and Dielectric Environment. *The Journal of Physical Chemistry B* **107,** 668–677 (2003).

9. Langhammer, C., Kasemo, B. & Zorić, I. Absorption and scattering of light by Pt, Pd, Ag, and Au nanodisks: Absolute cross sections and branching ratios. *The Journal of Chemical Physics* **126,** - (2007).

10. Meier, M. & Wokaun, A. Enhanced fields on large metal particles: dynamic depolarization. *Opt. Lett.* **8,** 581–583 (Nov. 1983).

11. Mendoza-Galván, A. *et al.* Optical response of supported gold nanodisks. *Opt. Express* **19,** 12093–12107 (June 2011).

12. Søndergaard, T. M. *Green's Function Integral Equation Methods in Nano-Optics* (Chap. 4). ISBN: 9780815365969 (CRC Press, 2019).

Chapter 3

Theory

3.1 Introduction

Second harmonic generation (SHG) spectroscopy has been used to investigate silicon surfaces and interfaces [1, 2], amongst other thing. In this work, it was used to probe changes in surface properties when introducing metal nanoparticles on a semiconductor surface.

This chapter contains a brief summary of the theory behind SHG and SHG spectroscopy and the effect of introducing metal particles. The linear optical properties of metal particles on a surface are also introduced. A brief description of Si bulk properties concludes this chapter.

The essence of the theory presented in Sections 3,2.4-6 and 3.3 can also be found in Paper A, but is included in this Chapter to place it in a broader context of SHG spectroscopy on nanoparticles on a Si surface.

3.2 Second harmonic generation

High intensity light induces a second harmonic polarization which is then a source for generating second harmonic field. This polarization can with the right tools and analysis provide much information on the geometric and electronic structure of the material.

Second harmonic generation spectroscopy is used to investigate electronic properties of silicon surfaces. In centrosymmetric materials, such as silicon, second harmonics can only be generated at the surface where symmetry is broken.

At low intensity the polarization of a material is proportional to the electric field of the incidence radiation, which in a lossless and dispersionless medium is given as:

$$\mathbf{P} = \epsilon_0 \overleftrightarrow{\chi}^{(1)} \cdot \mathbf{E} \tag{3.1}$$

where $\mathbf{P}$ is the polarization, ϵ_0 is the vacuum permittivity, $\overleftrightarrow{\chi}^{(1)}$ is the linear susceptibility and $\mathbf{E}$ is the electric field. Here, $\overleftrightarrow{\chi}^{(1)}$ is a second rank tensor describing the medium response.

For high intensity incidence fields the linear model is not always sufficient to describe the polarization of the medium. In most cases the nonlinear generation is relatively small and if we assume that only dipoles contribute to the polarization, it be expressed as a power series in $\mathbf{E}$:

$$\mathbf{P} = \epsilon_0 \overleftrightarrow{\chi}^{(1)} \cdot \mathbf{E} + \epsilon_0 \overleftrightarrow{\chi}^{(2)} \cdot \mathbf{E}^2 + \epsilon_0 \overleftrightarrow{\chi}^{(3)} \cdot \mathbf{E}^3 + ... \tag{3.2}$$

where $\overleftrightarrow{\chi}^{(1)}$ is the linear susceptibility, and $\overleftrightarrow{\chi}^{(2)}$ and $\overleftrightarrow{\chi}^{(3)}$ are the third and fourth rank tensor describing the second and third order nonlinear susceptibility. SHG is related to $\overleftrightarrow{\chi}^{(2)}$ and the generated 2^{nd} harmonic polarization, defined as

$$\mathbf{P}^{(2)} = \epsilon_0 \overleftrightarrow{\chi}^{(2)} \mathbf{E}^2 \tag{3.3}$$

3.2.1 SHG at surfaces

Centrosymmetric materials such as e.g. Si, have inversion symmetry, implying that the following must be true

$$\begin{aligned} \mathbf{P}^{(2)} &= \epsilon_0 \overleftrightarrow{\chi}^{(2)} (\mathbf{E})^2 \\ -\mathbf{P}^{(2)} &= \epsilon_0 \overleftrightarrow{\chi}^{(2)} (-\mathbf{E})^2 \end{aligned} \tag{3.4}$$

which is only possible if $\overleftrightarrow{\chi}^{(2)} = 0$. Hence, there is no bulk second harmonic dipole response due to symmetry. At surfaces and interfaces the symmetry is broken, thus SHG can be used as a surface sensitive probe. This holds only for local dipole contributions and the full picture is obtained when including the non-local higher order terms. The first order non-local terms are the electric quadrupole and magnetic dipole contributions, and they can not be expected to be zero in the bulk material. The nonlinear polarization is expected to be frequency dependent and in the case of SHG the components of the induced

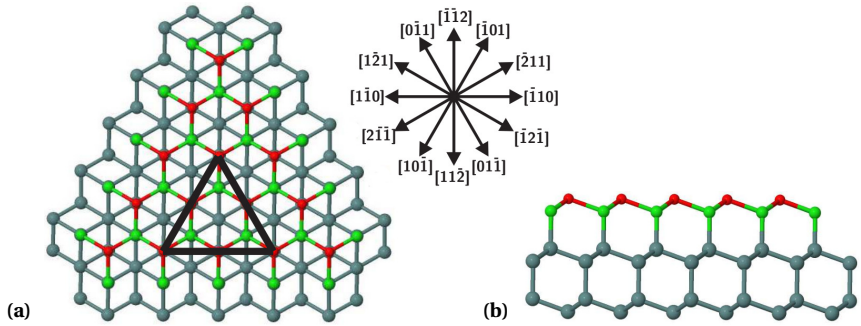

Figure 3.1: Reprint from [3]. (a) Top view of Si (111) crystal surface with crystal directions indicated next to the structure. (b) Side view of Si (111) crystal surface. In both (a) and (b) the red atoms are the topmost atom, the green atoms are second topmost atoms, and the grey atoms are the lower atoms. The black triangle represents the primitive cell of the (111) surface

second harmonic polarization can be described as

$$\begin{aligned} P_i(2\omega) &= \epsilon_0 \chi^{(2)\,local}_{ijk} (E_j(\omega) E_k(\omega) \\ &= \epsilon_0 \chi^{(2)\,nonlocal}_{ijkl} E_j(\omega) \nabla_k E_l(\omega) \\ &= ... \end{aligned} \tag{3.5}$$

which means that in general, one will get both surface and bulk contributions to the generated second harmonic signal. To interpret and separate the two contributions it is necessary to have deep understanding of the investigated system.

3.2.2 SHG from (111) crystal surfaces

The symmetry and structural properties of the investigated material is important to the generated second harmonic signal. Figure 3.1a shows the top view of the atomic structure for a (111) surface of a diamond cubic lattice, the equivalent of Si. Different crystal directions are also shown i the figure. Figure 3.1b is a sideview of the surface as seen along the $[0\bar{1}1]$ crystal direction. The colors of the atoms indicate different positions in the crystal. At this point it is

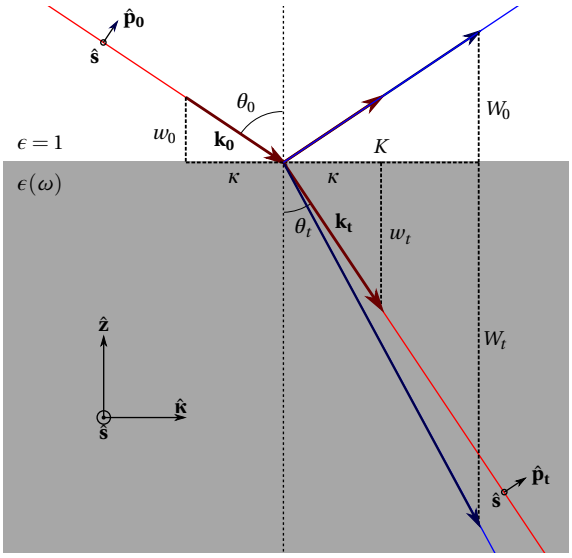

Figure 3.2: Geometry and vectors for the fundamental and harmonic field.

convenient to introduce a new coordinate system on the (111) surface. In this system the new $\hat{z}'$ axis is along the $[111]$ crystal direction and the $\hat{x}'$ axis is parallel to the surface in the $[2\tilde{1}\tilde{1}]$ crystal direction. The structural symmetry is reflected in the nonlinear surface susceptibility tensor and for the (111) surface it has three independent isotropic elements, $\chi^{(2)}_{zzz}$, $\chi^{(2)}_{zxx}$ and $\chi^{(2)}_{xzx}$ [4]. Moreover, the $3m$ symmetry of the surface gives rise to an anisotropic in plane element $\chi^{(2)}_{xxx}$. A detailed analysis by Sipe et al.[5] of the signal from the surface of a centrosymmetric crystal, including bulk contributions, gives some insights to the origin of the signal and means to separate different contributions. The analysis is based on the sample and beam parameters illustrated in Fig. 3.2. Here, the incident field, which is the driving field for the second harmonic polarization, is described as

$$\mathbf{E_0}(\mathbf{r},t) = \mathbf{E_0} e^{i(\mathbf{k_0}\cdot\mathbf{r}-\omega t)} + c.c. \tag{3.6}$$

where ω is the (fundamental) frequency and $\mathbf{k_0}$ is the incidence wavevector, which conveniently can be expressed in components parallel and normal to the surface

$$\mathbf{k_0} = \kappa\hat{\boldsymbol{\kappa}} - w_0\hat{\mathbf{z}} \tag{3.7}$$

where $\kappa = |\mathbf{k_0}|\sin(\theta_0) = (\omega/c)\sin(\theta_0)$ and $w_0 = ((\omega/c)^2 - \kappa^2)^{1/2}$. The incidence angle θ_0 and the directions $\hat{\kappa}$ and $\hat{z}$ are as defined in Fig. 3.2. $\mathbf{E_0}$ is the amplitude and can be expressed as a superposition of the components polarized parallel ($E_{0,p}$) and perpendicular ($E_{0,s}$) to the plane of incidence. In terms of $\hat{\kappa}$ and $\hat{z}$ the two polarization directions of the incidence beam are $\hat{\mathbf{s}} = \hat{\boldsymbol{\kappa}} \times \hat{\mathbf{z}}$ and $\hat{\mathbf{p}}_\mathbf{0} = c(\kappa\hat{\mathbf{z}} + w_0\hat{\boldsymbol{\kappa}})/\omega$. The field transmitted into a material with dielectric constant $\epsilon(\omega)$ is then given as

$$\mathbf{E_t}(\mathbf{r}, t) = \mathbf{E_t} e^{i(\mathbf{k_t}\cdot\mathbf{r} - \omega t)} \tag{3.8}$$

where $\mathbf{k_t} = \kappa\hat{\boldsymbol{\kappa}} - w_t\hat{\mathbf{z}}$ and $w_t = ((\omega/c)^2\epsilon(\omega) - \kappa)^{1/2}$. The field amplitudes for the two polarizations can be calculated via the Fresnel equations. The s-polarization direction is unchanged whereas the p-polarization is now $\hat{\mathbf{p}}_\mathbf{t} = c(\kappa\hat{\mathbf{z}} + w_t\hat{\mathbf{z}})/(n\omega) = f_s\hat{\mathbf{z}} + f_c\hat{\boldsymbol{\kappa}}$ where $n = \sqrt{\epsilon(\omega)}$. The generated second harmonic (SH) field is expressed with the equivalent symbols in capital letters, such that $\Omega = 2\omega$, $K = 2\kappa$, $W_0 = ((\Omega/c)^2 - K^2)^{1/2}$ and $W_t = ((\Omega/c)^2\epsilon(2\omega) - K^2)^{1/2}$. For the p-polarization of the SH the equivalent factors $F_s = cK/(N\Omega)$ and $F_c = cW/(N\Omega)$ where $N = \sqrt{\epsilon(\Omega)}$ is found. Within this picture the total second harmonic field signal from the (111) surface for the different polarizations is

$$\frac{E(2\omega)_{(p\to p)}}{E_p^2 A_p} = a_{p\to p} + c_{p\to p}\cos(3\phi) \tag{3.9}$$

$$\frac{E(2\omega)_{(s\to p)}}{E_s^2 A_p} = a_{s\to p} + c_{s\to p}\cos(3\phi) \tag{3.10}$$

$$\frac{E(2\omega)_{(p\to s)}}{E_p^2 A_s} = b_{p\to s}\sin(3\phi) \tag{3.11}$$

$$\frac{E(2\omega)_{(s\to s)}}{E_s^2 A_s} = b_{s\to s}\sin(3\phi) \tag{3.12}$$

where the notation $(a \to b)$ stands for fundamental polarization (a) and the detected SH polarization (b). ϕ is the angle between the $\hat{x}'$ axis and $\hat{\boldsymbol{\kappa}}$ axis. The

remaining factors are calculated as

$$A_p = \frac{4\pi\Omega N}{c\,(W_0\epsilon(\Omega)+W_t)} \tag{3.13}$$

$$A_s = \frac{4\pi\Omega}{c\,(W_0+W_t)} \tag{3.14}$$

$$\begin{aligned} a_{p\to p} = {} & \Gamma\zeta\left(\frac{4}{3}F_s f_c - \frac{2}{3}f_s F_c f_c^2 - \frac{8}{3}F_s f_s^2 f_c + \frac{4}{3}f_s^3 F_c\right) \\ & + i\frac{\Omega}{c}F_s\left(2\epsilon(\Omega)\chi^{(2)}_{zxx}+\gamma\right) \\ & + 2i\frac{\Omega}{c}\epsilon(\Omega)F_s f_s^2\left(\chi^{(2)}_{zzz}-\chi^{(2)}_{zxx}\right) - 4i\frac{\Omega}{c}f_s f_c F_c \chi^{(2)}_{xxz} \end{aligned} \tag{3.15}$$

$$\begin{aligned} c_{p\to p} = {} & -\Gamma\zeta\frac{\sqrt{8}}{3}\left(F_c f_c^3 - 2f_s^2 F_c f_c + F_s f_s f_c^2\right) \\ & - 2i\frac{\Omega}{c}F_c f_c^2 \chi^{(2)}_{xxx} \end{aligned} \tag{3.16}$$

$$\tag{3.17}$$

$$a_{s\to p} = \Gamma\zeta\frac{2}{3}\left(2F_s f_c + f_s F_c\right) + i\frac{\Omega}{c}F_s\left(2\epsilon(\Omega)\chi^{(2)}_{zxx}+\gamma\right) \tag{3.18}$$

$$c_{s\to p} = \Gamma\zeta\frac{\sqrt{8}}{3}\left(F_c f_c + F_s f_s\right) + 2i\frac{\Omega}{c}F_c\chi^{(2)}_{xxx} \tag{3.19}$$

$$b_{p\to s} = \Gamma\zeta\frac{\sqrt{8}}{3}\left(f_c^2 - 2f_s^2 f_c\right) + 2i\frac{\Omega}{c}f_c^2\chi^{(2)}_{xxx} \tag{3.20}$$

$$b_{s\to s} = -\Gamma\zeta\frac{\sqrt{8}}{3}f_c - 2i\frac{\Omega}{c}\chi^{(2)}_{xxx} \tag{3.21}$$

where

$$\Gamma = \frac{i\sqrt{\epsilon(\omega)}\Omega^2}{8(2w_t+W_t)c^2},$$

ζ is the bulk anisotropic contribution and γ is the bulk isotropic contribution.

The Eqs. 3.9-3.12 show that in general, second harmonic generation is surface sensitive but contains contributions from both bulk and surface. However, adjusting the angle ϕ allows for separating the isotropic and anisotropic surface contributions. For $\phi = \pi/6$ Eqs. 3.9 and 3.10 contain only isotropic surface contributions ($\chi^{(2)}_{zzz}$, $\chi^{(2)}_{zxx}$ and $\chi^{(2)}_{xzx}$), whereas Eqs. 3.11 and 3.12 only

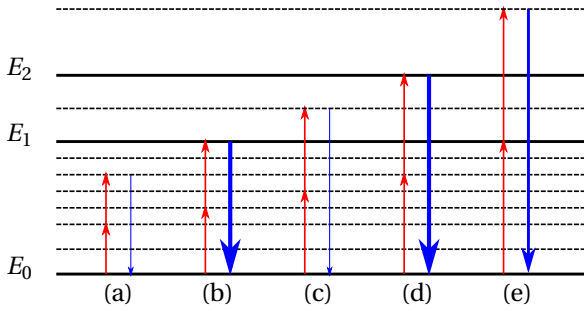

Figure 3.3: Representation of the second harmonic resonances.

contain the anisotropic surface term ($\chi^{(2)}_{xxx}$). Still, the problem with concurrent bulk and surface contributions remains. One method to distinguish between the two contributions is to modify the surface while tracking changes to the SH signal. Also, knowledge of bulk silicon properties, which will be presented in section 3.4, is important when analysing the recorded signal.

3.2.3 Second harmonic spectroscopy

The second harmonic generation process can be viewed as an electron being excited by two photons with frequency ω and then relaxes by emitting a photon with frequency 2ω. When one of the photon energy coincides with an energy level in the sample, the second harmonic signal will be resonantly enhanced. Figure 3.3 illustrates a few scenarios with different photon frequencies. In (a) and (c) neither the fundamental nor the SH photon coincide with an energy level and no enhancement is seen. In (b) and (e) there will be enhancement due to overlap between 2ω and E_1 energy, and ω and E_1, respectively. In (d) there will be enhancement due to 2ω and E_2 overlap. Thus by varying the fundamental frequency, electronic states at the surface can be investigated. A surface may contain a number of resonances at different frequencies and surface modifications could introduce additional resonances. The modelling of the nonlinear susceptibility containing these features is based on the work of Erley et al.[6] and Suzuki et al.[7], describing the susceptibility as a coherent sum of interband resonance transitions:

$$\chi^{(2)}(2\omega) \propto \sum_n \frac{f_n e^{i\phi_n}}{2\omega - \omega_n + i\gamma_n} \tag{3.22}$$

where f_n is the amplitude of the resonance n, ϕ_n is the resonance phase, ω_n is the resonance frequency and γ_n is the resonance width.

3.2.4 SHG and metal particles

In this work SHG has been used to probe surface and interface effects in order to investigate the interaction between metallic nanoparticles and semiconductor substrates.

The SH polarization of small metal particles is given by [8]:

$$P_m(2\omega) = L_{2\omega}\chi_m^{(2)}(2\omega)L_\omega^2 E^2(\omega) \tag{3.23}$$

where $\chi_m^{(2)}$, L_ω and $L_{2\omega}$ are respectively the effective SH susceptibility of the metal, the local field factor at frequency ω and the local field factor at frequency 2ω. According to [8] the local fields factors in the dipole approximation are:

$$L(\omega) = \frac{\epsilon_d(\omega)}{\epsilon(\omega) + [\epsilon_m(\omega) - \epsilon_d(\omega)]M} \tag{3.24}$$

where ϵ_m and M are respectively the dielectric constant of the metal and the shape-dependent depolarization factor of the metal particles.

For the metal particles the surface susceptibility also reduces to three components (centrosymetric and isotropic material), and the surface SH polarization reduces to three contributions [5]:

$$P_{m,\parallel}(2\omega) = P_{m,\parallel\perp\parallel}(2\omega) \tag{3.25}$$

$$P_{m,\perp}(2\omega) = P_{m,\perp\perp\perp}(2\omega) + P_{m,\perp\parallel\parallel}(2\omega) \tag{3.26}$$

where $P_{m,\parallel}$ and $P_{m,\perp}$ are the total parallel and perpendicular SH polarization for the metal particles. Each contribution term in Eq. 3.25 can be expressed as:

$$P_{m,ijk}(2\omega) = L_i(2\omega)\chi_{m,ijk}^{(2)}(2\omega)L_j(\omega)E_j(\omega)L_k(\omega)E_k(\omega) \tag{3.27}$$

where $\{i, j, k\}$ can stand for either parallel or perpendicular directions. From Eq. 3.24 the local field factors $L_i(2\omega)$, $L_j(\omega)$ and $L_k(\omega)$ can be obtained and the tensor elements $\chi_{m,ijk}^{(2)}$ in Eq. 3.27 are calculated with the classical form

for the surface of a semiinfinite system [9, 10]:

$$\chi^{(2)}_{m,ijk} = -\frac{a_{ijk}}{2}[\epsilon_m(\omega)-1]\frac{e\epsilon_0}{m\omega^2}. \tag{3.28}$$

Size and shape effects of the metallic nanoparticles are taken into account by modifying the bulk dielectric function of the metal, ϵ_m. The Rudnick and Stern parameters, $a_{\parallel\perp\parallel}$ and $a_{\perp\perp\perp}$, describe the parallel and vertical surface currents, respectively, and the value of those parameters can be both complex and frequency dependent [9, 11]. In the literature the $P_{m,\perp\parallel\parallel}$ term is often disregarded, as its contribution is very weak for plane surfaces [12], but, in this model, its contribution has been found to be significant for surfaces covered by metal particle.

3.2.5 Metal nanoparticles on a substrate

The fundamental and generated SH fields are both enhanced by the metallic particles. The presence of the metallic particles influences also the reflection, transmission and absorption properties of the interface. The local field enhancement and the modification of the transmission properties of the interface by the metallic particles affect the SH polarization of the substrate which can be expressed as:

$$P_i(2\omega) = T_{eff,ijk}L_{eff,ijk}\chi^{(2)}_{ijk}(2\omega)E_j(\omega)E_k(\omega) \tag{3.29}$$

where $L_{eff,ijk}$ is the effective local field factor taking into account both the electric field at ω and the electric field at 2ω, and $|L_{eff}|^2$ is often referred to as the enhancement factor. The modifications of the absorption and transmission properties of the surface at frequency ω and 2ω are comprised in $T_{eff,ijk}$.

The presence of the metallic particles at the interface induces a space charge region (SCR) and results in a build-in electric field (E^{dc}) which breaks the symetry of the semiconductor substrate. This effect gives rise to a SH signal which is commonly referred to as the electric-field-induced-second-harmonic (EFISH) signal. The creation of SCR by build-in charges in thin films or in particles deposited on a Si/SiO_2 surface has been reported [13, 14]. The EFISH process is a third-order process, but its response can be effectively described by a second-order susceptibility tensor $\chi^{(2)}_{eff}$. The EFISH SH polarization can

be expressed as[15, 16]:

$$P_{s,EFISH}(2\omega) = \chi^{(2)}_{s,eff}(2\omega)E^2(\omega). \tag{3.30}$$

The second-order susceptibility tensor is given by $\chi^{(2)}_{s,eff}(2\omega) = \chi^{(3)}_s(2\omega)E^{dc}$, where $\chi^{(3)}_s$ is the third-order susceptibility tensor of the substrate.

3.2.6 Modelling of second harmonic generation

In this work, a model describing the intensity of the measured SHG signal was developed in order to get a better understanding of the different phenomena involved and their importance. The model takes into account all the SH polarisations for the combined system of metal particles on a substrate and can be summarized by:

$$I(2\omega) \propto \left| \sum_{ijk} P^m_{ijk} + \sum_n P^s_n \right|^2 \tag{3.31}$$

where P^m_{ijk} are the metal polarizations described by Eq. 3.27 and P^s_n are the substrate polarizations obtained from Eq. 3.29. Even though Eq. 3.31 is simple, it involves many variables and it has proven to be very difficult to analyse and correlate the results with the measurements without information obtained through SEM analysis and linear measurements.

3.3 Linear effects

With the increase in interest for localized plasmon resonances seen in the last years, the linear optical response of metal particles has been investigated thoroughly. In this work, the linear response of metallic particles is used in modelling the intensity of the SH signal and ease the interpretation of the SH spectra. More precisely, it provides the absorption of the particles and the depolarisation factors.

In this work the Island Film Theory (IFT) approach [17, 18] and differential reflectivity spectroscopy [19] (DRS) are used to investigate the linear properties. There are other models describing this response, such as the homogeneous uniaxial layer approach [17] or the dynamic Yamaguchi approach [20], both applying the effective medium method and convincingly reproducing the

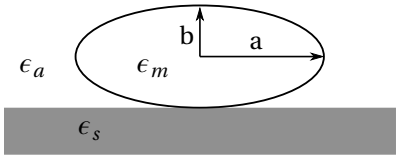

Figure 3.4: Representation of an oblate spheroid touching the substrate. a is the major semi axis and b is the minor semi axis.

experimental results. However, DRS and IFT were chosen as they readily provide information that can be used in the SHG modelling. Differential reflectivity is defined as:

$$\frac{\Delta R}{R_0} = \frac{R - R_0}{R_0} = \frac{I - I_0}{I_0} \tag{3.32}$$

where R an R_0 are the reflectivities of the surface with and without metal particles, respectively. Further, the reflectivity can be calculated as $R = |r|^2$ where r is the Fresnell reflection coefficient. Using the same light source for the measurement, the differential reflectivity can be obtained using intensities instead. In the IFT an extra term is added to the Fresnell reflection coefficients, containing the surface susceptibilities γ and β, in order to include the contribution of the metallic particles.

For this work, the particles are in reasonable approximation oblate spheroids in contact with the substrate as depicted in Fig. 3.4, where the major semi-axis (a) is parallel to the substrate. The modified Fresnel coefficients for both reflection and transmission are respectively given by:

$$r_p = \frac{\kappa_- - \xi_-}{\kappa_+ - \xi_+} \tag{3.33}$$

and

$$t_p = \frac{2 n_a \cos\Theta \left(1 + \frac{1}{4} k^2 \epsilon_a \beta \gamma \sin^2\Theta\right)}{\kappa_+ - \xi_+} \tag{3.34}$$

where

$$\kappa_\pm = (n_s \cos\Theta_i \pm n_a \cos\Theta_t) \left[1 - \frac{1}{4} k^2 \epsilon_a \gamma \beta \sin^2\Theta_t\right], \tag{3.35}$$

$$\xi_{\pm} = i\frac{2\pi}{\lambda}\left[\gamma\cos\Theta_i\cos\Theta_t \pm n_a^3 n_s \beta \sin^2\Theta_i\right], \tag{3.36}$$

where n_a and ϵ_a are the refractive index and dielectric function of the ambient medium, respectively. $k = 2\pi/\lambda$ and n_s is the refractive index of the substrate. Θ_i and Θ_t are the incidence and refracted angles respectively. The surface susceptibility γ and β can then be expressed in terms of the density of particles ρ and the parrallel $\alpha_{\parallel}$ and perpendicular $\alpha_{\perp}$ dipolar polarizabilities:

$$\gamma = \rho\alpha_{\parallel} \quad \text{and} \quad \beta = \rho\alpha_{\perp}/\epsilon_a^2. \tag{3.37}$$

In the dipole approximation, the polarizabilities of spheroidal particles is given by:

$$\alpha_{\parallel,\perp} = \frac{4\pi a^2 b}{3}\frac{\epsilon_a(\epsilon_m - \epsilon_a)}{\left[\epsilon_a + M_{\perp,\parallel}(\epsilon_m - \epsilon_a)\right]}. \tag{3.38}$$

where ϵ_m stands for the dielectric function of the metal particles and $M_{\perp,\parallel}$ stands for the factors for the perpendicular and parallel directions respectively. They can be calculated with following equations:

$$M_{\perp} = l_{\perp} + \left(1+\beta^2\right)\left(\frac{\epsilon_a - \epsilon_s}{\epsilon_a + \epsilon_s}\right)\left[\beta\,\mathrm{atan}\left(\frac{1}{\beta}\right) - \left(\beta^2 + \frac{3}{2}\right)\beta^2 \ln\left(1 + \frac{1}{\beta}\right) + \beta^2\right] \tag{3.39}$$

$$M_{\parallel} = l_{\parallel} + \frac{1}{2}\left(1+\beta^2\right)\left(\frac{\epsilon_a - \epsilon_s}{\epsilon_a + \epsilon_s}\right)\left[\beta\,\mathrm{atan}\left(\frac{1}{\beta}\right) - \left(\beta^2 + \frac{3}{2}\right)\beta^2 \ln\left(1 + \frac{1}{\beta^2}\right) + \beta^2\right] \tag{3.40}$$

where

$$\begin{aligned} \beta &= \left[\left(\frac{a}{b}\right)^2 - 1\right]^{-1/2} \\ l_{\perp} &= \left(1+\beta^2\right)\left[1 - \beta\,\mathrm{atan}\left(\frac{1}{\beta}\right)\right] \\ l_{\parallel} &= \frac{1 - l_{\perp}}{2} \end{aligned} \tag{3.41}$$

One of the particularities arising from the nanoscale of the metallic particles is that their size becomes comparable with the bulk mean free path of the electrons. This effect influences the dielectric function with respect to the bulk dielectric function (ϵ_B) and can be expressed as:

$$\epsilon_m(\omega) = \epsilon_B(\omega) + \frac{\omega_p^2}{\omega^2 + \imath\omega\tau_B^{-1}} - \frac{\omega_p^2}{\omega^2 + \imath\omega\tau^{-1}} \tag{3.42}$$

where ω_p is the plasma frequency and τ_B is the relaxation time in the bulk. The relaxation time in the nanoparticles τ^{-1} is obtained from:

$$\tau^{-1} = \tau_B^{-1} + \upsilon_F R'^{-1} \tag{3.43}$$

where υ_F and R' are the Fermi velocity and the effective radius of the particles, respectively. When the particles become larger, the horizontal polarizability $\alpha_\parallel$ needs to be renormalized while taking into account dynamic depolarization [17, 21]:

$$\frac{1}{\alpha_\parallel^*} = \frac{1}{\alpha_\parallel} - \frac{k^2}{4\pi a} - \imath\frac{k^3}{6\pi}. \tag{3.44}$$

Combining the above theory with the information obtained from SEM analysis allows for a detailed analysis with only two free parameters, namely particle height ($2b$) and effective radius (R'). From this we get the depolarization factors ($M_\perp$ and $M_\parallel$), a modified dielectric function for the metal (ϵ_m), and the new absorption, transmission and reflection properties of the surface. The linear measurements and analysis enable a credible interpretation of the SHG, without which the number of free variables would have been to high to solve the problem.

3.4 Bulk silicon properties

The bulk electronic properties of Si are important to understand in order to interpret the SH spectra. Fig 3.1a-b in section 3.2 show the top view and side view of a Si (111) crystal surface. The black triangle on Fig. 3.1a represents the primitive cell of the (111) surface an illustrates the 3-fold symmetry of the surface. The red and green atoms in 3.1a and 3.1b represents the topmost and second topmost atoms of the crystal surface, the grey are lower atoms. Moreover some crystal directions are indicated next to the top view structure. Fig. 3.5 shows the Brillouin zone of crystalline Si (Fig. 3.5a) and part of bulk Si electronic band structure (Fig. 3.5b). In Fig. 3.5a the crystal axis are represented by x, y and z. In both subfigures, high symmetry points Γ, K, U, L and X, and directions Σ, Λ and Δ are indicated. The Λ direction is parallel to the Si(111)

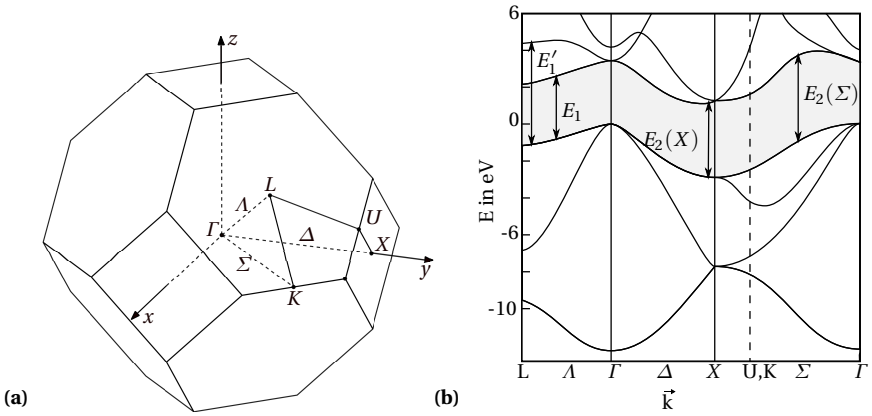

Figure 3.5: (a) Brillouin zone of Si crystal including crystal axis ($x\,y\,z$). High symmetry points Γ, K, U, L and X, and directions Σ, Λ and Δ are indicated in the figure. (b) Part of the bulk Si band structure related to the symmetry points and directions in (a).

surface normal vector and the plane containing L also shows the 3-fold symmetry of the Si(111) surface.

In relation to SHG some transitions between bands in bulk Si are of importance [2]. First, the E_1 transition in bulk Si between Λ bands in the direction from Γ to L that has an energy of is 3.4 eV. Related to E_1 is the E_1' transition [22] with an energy of 5.5 eV. Both E_1 and E_1' are both shown in Fig. 3.5b. The E_2 transition consists of two contributions [23]: the $E_2(X)$ transition between Δ bands in direction Γ to X with energy 4.27 eV and $E_2(\Sigma)$ in direction from Γ to K with energy 4.51 eV. All transitions are indicated on Fig. 3.5b. These are bulk energy levels and will in general differ from surface energy levels due to bending, stretching or compression of Si bands at the first couple of surface layers.

3.5 Summary

This chapter introduced the theory behind SHG, SHG spectroscopy for surfaces and interfaces including metal nanoparticles. The linear optical properties of metal particles on a surface, as well as Si bulk properties, were also introduced as important tools to help interpret the SHG results presented in chapter 5.

References

1. Pedersen, K. & Morgen, P. Optical second-harmonic generation spectroscopy on Si(111)7x7. *Surface Science* **377-379.** European Conference on Surface Science, 393–397. ISSN: 0039-6028 (1997).
2. Daum, W. Optical studies of Si/SiO2 interfaces by second-harmonic generation spectroscopy of silicon interband transitions. *Applied Physics A* **87,** 451–460. ISSN: 0947-8396 (2007).
3. Rafaelsen, J. *Surface studies of Germanium interfaces and nano-structures.* Ph.D. dissertation (2013).
4. Tom, H. W. K., Heinz, T. F. & Shen, Y. R. Second-Harmonic Reflection from Silicon Surfaces and Its Relation to Structural Symmetry. *Phys. Rev. Lett.* **51,** 1983–1986 (21 Nov. 1983).
5. Sipe, J. E., Moss, D. J. & van Driel, H. M. Phenomenological theory of optical second- and third-harmonic generation from cubic centrosymmetric crystals. *Phys. Rev. B* **35,** 1129–1141 (3 Jan. 1987).
6. Erley, G. & Daum, W. Silicon interband transitions observed at Si(100)-SiO_2 interfaces. *Phys. Rev. B* **58,** R1734–R1737 (4 July 1998).
7. Suzuki, T., Milovzorov, D., Kogo, S., Tsukakoshi, M. & Aono, M. Surface second-harmonic generation spectra of Si(111)-7x7 in the 1.0 1.7eV fundamental photon energy. *Applied Physics B* **68,** 623–627. ISSN: 0946-2171 (1999).
8. Kim, E. M. *et al.* Surface-Enhanced Optical Third-Harmonic Generation in Ag Island Films. *Phys. Rev. Lett.* **95,** 227402 (22 Nov. 2005).
9. Bachelier, G. *et al.* Origin of optical second-harmonic generation in spherical gold nanoparticles: Local surface and nonlocal bulk contributions. *Phys. Rev. B* **82,** 235403 (23 Dec. 2010).
10. Rudnick, J. & Stern, E. A. Second-Harmonic Radiation from Metal Surfaces. *Phys. Rev. B* **4,** 4274–4290 (12 Oct. 1971).
11. Sipe, J. E., So, V. C. Y., Fukui, M. & Stegeman, G. I. Analysis of second-harmonic generation at metal surfaces. *Phys. Rev. B* **21,** 4389–4402 (10 May 1980).
12. Wang, F. X. *et al.* Surface and bulk contributions to the second-order nonlinear optical response of a gold film. *Phys. Rev. B* **80,** 233402 (23 Dec. 2009).

13. Rafaelsen, J., Pedersen, K. & Li, Z. Size-effects in photoemission and optical second harmonic generation spectroscopy of Ge nano-dots on Si(111). *Journal of Applied Physics* **114,** 044304 (2013).

14. Dingemans, G., Terlinden, N. M., Verheijen, M. A., van de Sanden, M. C. M. & Kessels, W. M. M. Controlling the fixed charge and passivation properties of Si(100)/Al2O3 interfaces using ultrathin SiO2 interlayers synthesized by atomic layer deposition. *Journal of Applied Physics* **110,** 093715 (2011).

15. Aktsipetrov, O. A., Fedyanin, A. A., Golovkina, V. N. & Murzina, T. V. Optical second-harmonic generation induced by a dc electric field at the Si–SiO2 interface. *Opt. Lett.* **19,** 1450–1452 (Sept. 1994).

16. Dadap, J. I. *et al.* Measurement of the vector character of electric fields by optical second-harmonic generation. *Opt. Lett.* **24,** 1059–1061 (Aug. 1999).

17. Mendoza-Galván, A. *et al.* Optical response of supported gold nanodisks. *Opt. Express* **19,** 12093–12107 (June 2011).

18. Bobbert, P. & Vlieger, J. The polarizability of a spheroidal particle on a substrate. *Physica A: Statistical Mechanics and its Applications* **147,** 115–141. ISSN: 0378-4371 (1987).

19. Lazzari, R. *et al.* Multipolar plasmon resonances in supported silver particles: The case of Ag/α-Al2O3(0001). *Phys. Rev. B* **65,** 235424 (23 June 2002).

20. Yamaguchi, T., Yoshida, S. & Kinbara, A. Optical effect of the substrate on the anomalous absorption of aggregated silver films. *Thin Solid Films* **21,** 173–187. ISSN: 0040-6090 (1974).

21. Meier, M. & Wokaun, A. Enhanced fields on large metal particles: dynamic depolarization. *Opt. Lett.* **8,** 581–583 (Nov. 1983).

22. Lautenschlager, P., Garriga, M., Vina, L. & Cardona, M. Temperature dependence of the dielectric function and interband critical points in silicon. *Phys. Rev. B* **36,** 4821–4830 (9 Sept. 1987).

23. Dolgova, T. V., Fedyanin, A. A., Aktsipetrov, O. A. & Marowsky, G. Optical second-harmonic interferometric spectroscopy of $Si(111)-SiO_2$ interface in the vicinity of E_2 critical points. *Phys. Rev. B* **66,** 033305 (3 July 2002).

Chapter 4

Sample Fabrication

4.1 Introduction

In order to investigate effects and properties of metallic structures on a semiconductor surface a number of samples with different characteristics where fabricated. This chapters describes the different fabrications processes used in this work including thermal metal deposition and electron-beam lithography.

4.2 Samples for the second harmonic generation experiments

SHG is extremely surface sensitive and small changes or contamination of the sample will affect the signal. Samples for SHG investigation are made under ultra high vacuum conditions to ensure a controlled environment and well defined interfaces for long periods of time.

4.2.1 Thin oxide layer

To study the effect of metal nanoparticles on a Si surface, the natural oxide is removed by two short heating to 1000°C while the sample is mounted in the vacuum chamber. The expected surface from this treatment is a 7x7 reconstruction which can be verified via the low energy electron diffraction (LEED) setup available in the chamber. To seal and passivate the surface, the sample is exposed to 1200 L of O_2 at a temperature of 600°C. This creates a ∼1 nm thick silicon oxide layer [1]. Figure 4.1 shows a scanning transmission electron

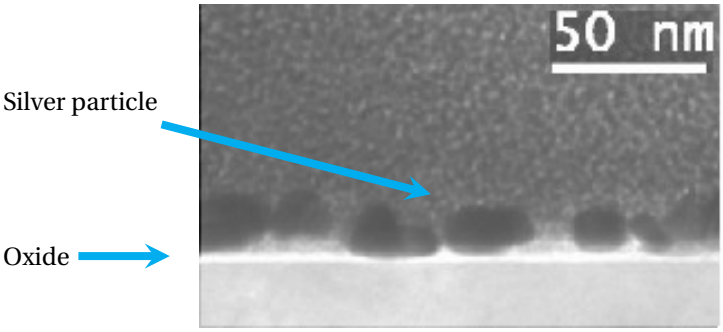

Figure 4.1: STEM image of Si-SiOx surface with Ag particles. The oxide layer is seen as a thin bright line. Charging effects make the oxide layer appears thicker. The Ag particles are the dark areas.

microscope (STEM) image obtained at iNANO, Aarhus University. In this image the oxide layer is seen as the bright line indicated on the figure. The line appears thicker due to charging effects when using the electron microscope. Another testament of how thin the oxide layer is is shown in Fig. 4.2 where the edges of self-assembled metal particles follow the underlying crystal-structure of Si (111). The process is self saturating and will not grow thicker under further exposure of O_2. The layer is very thin and is not strictly SiO_2. It will be referred to as a SiO_x layer.

4.2.2 Metal deposition

The metal nanoparticles for the SHG experiments are all made by deposition using an electron beam evaporator, available inside the UHV-chamber, where the sample is kept in a controlled environment. The formation of nanoparticles using this method is a complex process and is governed by many factors, including the choice of substrate and metal, as well as thermodynamics and kinetics, and generally results in a broad distribution of particle sizes and shapes. This section is meant to give a brief overview of the processes involved. The formation of particles can roughly be divided into two phases: nucleation and growth. Nucleation is important for the number of particles per area, whereas the growth process governs the shape of the particles.

Nucleation

At the beginning of the deposition process there are only a few metal atoms on the surface (adatoms) and due to a low affinity with the substrate, they migrate the surface to form nuclei when meeting other adatoms or an existing nuclei. If the influx of atoms from the vapor phase (F) from the evaporator is approximately constant and desorption of metal adatoms is neglegted, nuclei will continually be formed on the substrate when adatoms meet. At some point the chance of forming a new nuclei is much less than the chance of an adatom attaching to an existing nuclei and the number density of nuclei will approximately saturate at [2]

$$N = \sqrt{\frac{40F}{D}} \tag{4.1}$$

where D is the diffusion coefficient and describes the movement of the adatoms. The equation shows that the number of nuclei per area increases with influx atoms and decreases with increasing diffusion. The temperature (T) of the substrate and adatoms plays an important role in both the number density and subsequently in the shape and size of the particles. In the initial formation of nuclei the effect of the temperature is explained via the diffusion D and time on surface τ, calculated as [2]

$$D = D_0 \exp\left(-\frac{E_{diff}}{RT}\right) \tag{4.2a}$$

$$\tau = \tau_0 \exp\left(\frac{E_{des}}{RT}\right). \tag{4.2b}$$

Here D_0 is the diffusion constant, E_{diff} is the activation free energy for diffusion, R is the gas constant and T is the temperature. τ_0 is a prefactor and E_{des} is the activation free energy for desorption. Both E_{diff} and E_{des} differ for different adatoms and surfaces. Equation 4.2a shows that diffusion increases with increasing temperature. Thus the saturated number density (Eq. 4.1) will decrease with increasing temperature.

When depositing metals like Ag and Au there will be desorption of adatoms from the substrate. This means that each adatom has only a limited time on the surface given by τ. As seen in Eq. 4.2b, τ decreases with increasing temperature. Intuitively a decreasing time on the substrate would lead to more nuclei as the average diffusion length ($x = (Dt)^{(1/2)}$) will decrease. This is

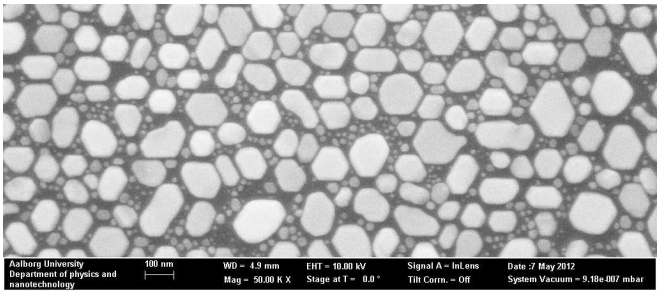

Figure 4.2: SEM image of Au particles deposited on a Si substrate where the shape of the particles reflects the underlying hexagonal Si structure.

not observed experimentally and instead the number of nuclei decreases with increasing temperature (i.e. decreasing time) as predicted by Eqs. 4.1 and 4.2a.

Another important factor is inhomogeneities in the substrate which affect the formation of nuclei by introducing nucleation centres and by defining paths where the diffusion energy is different. The effect of the inhomogeneities can be reduced by increasing the temperature and thereby the diffusion of the adatoms, pushing to a thermodynamic equilibrium.

Particle growth

After the initial formation of nuclei the growth process starts where the particles grow in volume as a function of time, while F, D, τ and substrate imhomogeneties are still playing a role. Substrate imhomogeneties are particularly important at low temperatures, and the thin oxide layer of the samples allows the underlying crystal structure of the Si (111) surface to affect greatly the shape of the particles. This is evident in Fig. 4.2 where the sides of most particles orient with the underlying structure. Increasing the temperature reduces both the average size due to desorption [3–5] and the effect of substrate inhomoginities. The adatoms have enough energy to move unaffected and make jumps to find energetically favorably position, forming particles on the surface. At this stage the shape of the particles is governed by the interface free energy. The system can be described by three interface energies [6]: γ_{SV}, γ_{SM} and γ_{MV}, where the subscripts S, V and M stands for substrate, vacuum and metal, respectively. Where the three interfaces meet the interface tensions must be at an equilibrium, which defines the cross-sectional shape of the particles and is

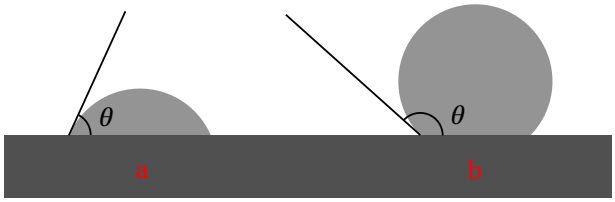

Figure 4.3: Illustration of the cross sectional shape of particles with different contact angle θ: (a) Au particle with $\theta < 90°$ and (b) Ag particle with $\theta > 90°$.

described via the contact angle θ (see Fig. 4.3). The contact angle is calculated as

$$\cos(\theta) = \frac{\gamma_{SV} - \gamma_{SM}}{\gamma_{MV}} \tag{4.3}$$

When the interface free energy of the substrate-vacuum interface is larger than the free energy of the substrate-metal interface, the result is flat particles with a small contact angle as seen in Fig. 4.3a. If the opposite is true, the particles rise up and can become almost spherical. If γ_{MV} is smaller than $|\gamma_{SV} - \gamma_{SM}|$ particles will not form on the surface and a continuous film will fill the surface.

In the case of Au and Ag particles, the particles formed are very different in shape. Au on SiO_x produces rather large and flat particles, which can be seen in the SEM image in Fig. 4.4. The camera angle in the SEM image is 54°. From this perspective the particles on the surface appears flat, e.g. arrow 1. Arrow 2 points to a cross-section of a particle. This has been achieved by first covering a part of the surface with Platinum using gas-injection and then by using a focused ion beam to cut and polish a cross-section of a particle. However, the resolution of the setup and charging effects made a reliable estimation of particle height impossible. Ag on SiO_x produces high and almost spherical particles as evident in Fig. 4.1. Studies of growth on air-oxidized Si(111)-(7x7) showed Ag particles oriented similar to epitaxial growth of Ag on Si(111) surfaces [7]. At a temperature (T=500°C) and a deposition rate (2 ML/min) similar to that of [7] with an even thinner oxide used, particles with the same characteristics were expected. In Fig. 4.5 a STEM image obtained at iNANO, Aarhus University, shows signs of lattice planes in two silver particles, as highlighted in the figure. In both particles the planes are oriented the same, thus indicating a substrate effect.

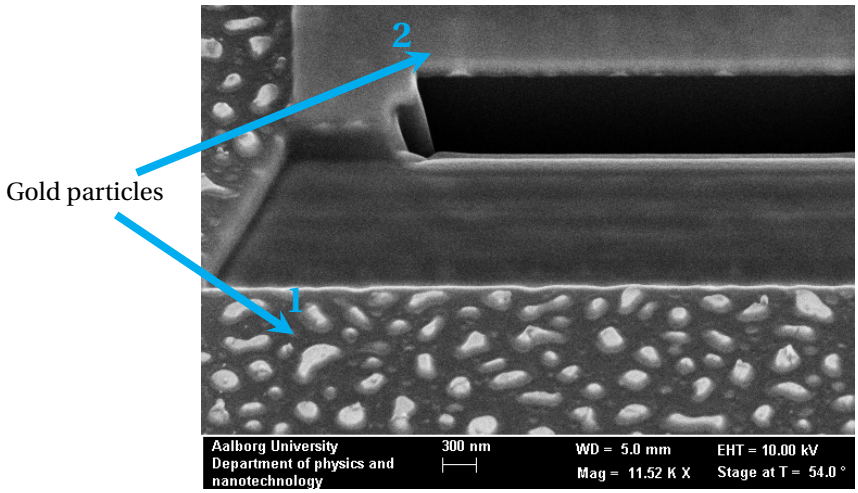

Figure 4.4: SEM cross-section image of Si-SiO_x surface with Au particles. Arrow 1 points to a surface with Au particles and arrow 2 points to a cross section of a Au particle.

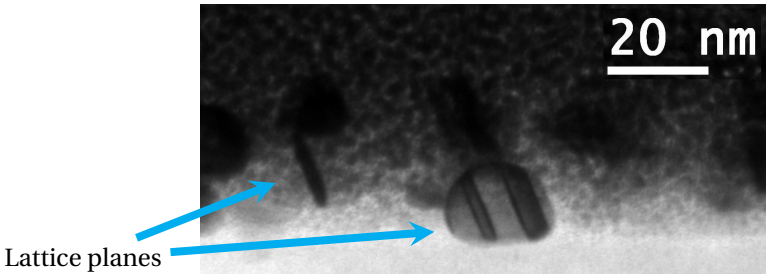

Figure 4.5: STEM image of Ag particles deposited on a Si substrate. The blue arrows highlights two particles where lattice planes with identical orientation are visible.

Summary

Metal deposition is a relatively simple and fast method to form nanoparticles on a surface, offering a fair degree of control over the number and size of the particles. The materials used, both the metal and the substrate, are obviously important and together with temperature are the limiting factor for number density, shape and size of the particles. Within the limits set by the materials, temperature plays an important role, as it enables movement of the adatoms on the surface. Increasing the temperature results in fewer particles but also decreases the width of the particle size distribution. Higher temperature also increases the desorption rate and results in smaller particles. High temperatures also minimize the effect of inhomogeneities in the substrate. Other controllable parameters are the influx of metal atoms and time: an increase in flux will increase the number of particles and time will increase the size of the particles. This method produces particles with a given distribution in size which are formed in a controlled environment inside the vacuum chamber. The number of particles and the size of the particles can only be assessed after unmounting the sample from the vacuum chamber.

4.3 Fabrication of samples with e-beam lithography

E-beam lithography (EBL) is a powerful technique to make structures on the nanoscale. In this work it as been used extensively to make samples, both on small test solar-cells (paper C) as well as different types of wafers (paper D) and GaAs half-cylinders (paper B). The biggest advantage of EBL is an excellent control over the shape and position of the particles. The working principle EBL is illustrated in Fig. 4.6. It is using a focused electron beam to define structures in an electron sensitive resist film covering a substrate. The electrons change the solubility of the resist and exposed areas can then be removed in a development process by immersing the film into a solvent. Thus the structures defined by the e-beam are now bare substrate. The final step is coating the sample and in a liftoff process remove the remaining resist with coating on top, leaving the defined structures on the substrate.

The different steps of the EBL process, as illustrated in Fig. 4.6, will be further detailed in the following paragraphs.

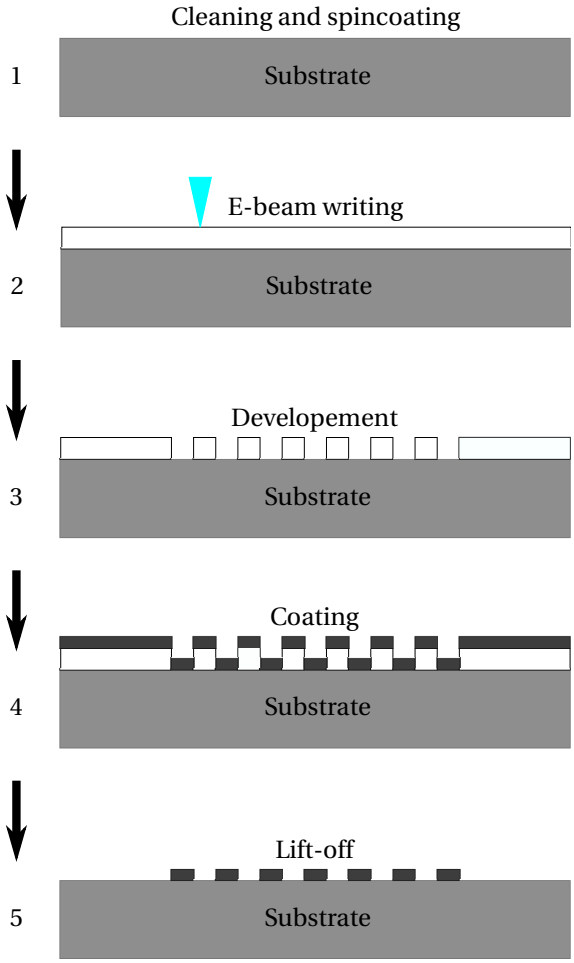

Figure 4.6: Schematic of the fabrication processes involved in EBL.

Step 1. Preparation of the substrate

A clean substrate is critical for a successful EBL process. Prior to applying the resist, the following steps were performed on a wet bench inside the cleanroom:

1. Organic materials are removed by 2 min in an ultrasonic bath with acetone.
2. The sample is rinsed with milli Q water and blown dry with N_2.
3. Acetone and organic leftovers are removed by 2 min in an ultrasonic bath with ethanol.
4. The sample is rinsed with milli Q water and blown dry with N_2.

The steps are repeated if necessary.

The electron sensitive resist used in this work is a poly(methyl methacrylate) (PMMA) type with toluene as a solvent. It is a positive resist, meaning that the exposed areas are removed during development. The resist is applied by spincoating on a Laurell WS-650S-23NPP spin coater. The required thickness of the resist depends on the desired high of the nanostructures, where the general rule is the lower the thickness to height ratio, the greater the risk of liftoff failure. A ratio above 3:1 is generally on the safe side. The trade-off in increasing the thickness is that it reduces the resolution of the e-beam written pattern. A specific thickness is obtained by using the appropriate PMMA concentration in combination with adjusting the speed of the spincoater. Finally, the resist is baked on a hotplate for 5 min. The resulting thickness is measured using a profiler available in the cleanroom.

Step 2. E-beam writing

The structures are written using a Raith Elphy Plus system connected to a Zeiss 1540 XB electron microscope. The Raith system controls the electron beam and allows for precise definition of structures in the resist. This setup has a writing field area of 100 x 100 μm^2. For larger areas the sample must be moved and aligned with the neighbouring fields in a process called stitching. The exposure of resist is a complicated mater with many parameters available, and depends on substrate, resist, electron energy, beam current and beam spot size. The high energy incidence electron beam creates secondary electrons as it enters the resist and they have a large impact on the exposure. Structures

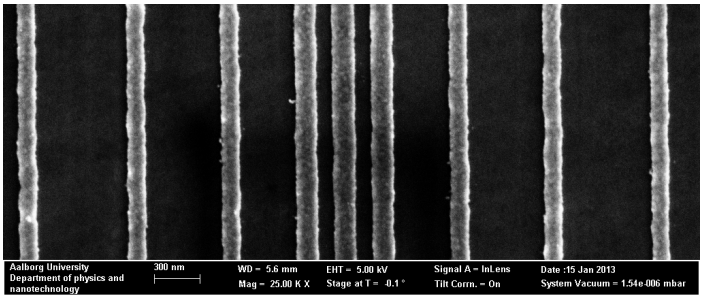

Figure 4.7: SEM image showing proximity effects when using EBL. In this case proximity effects made the three center strips wider than the other strips.

written close together may experience proximity effects, where the exposure affects neighbouring structures. Figure 4.7 is from the work leading up to paper B. It shows strips of Ag on a GaAs surface. The intended strip width was 130 nm, but proximity effects made the three strips at the center wider. Apart from a few cases, in most of this work the structures were sufficiently far apart to neglect proximity effect. Conducting substrates were used, and the structures were simple with no complicated geometrical shape. A basic setup could be used when writing structures, which includes an electron energy of 10 keV, a fixed current and the beam focused on the substrate surface. The exposure is then controlled via a dose factor which translates into the velocity of the beam moving across the sample. Due to the many factors at play, the correct dose factor is difficult to calculate and is found after performing a writing test on a small sample. The test is the complete EBL procedure, including liftoff, at a smaller scale. A few structures with different doses are written on a similar substrate with identical resist thickness, and subsequently investigated in SEM to identify the best dose factor.

Another special case is EBL on a non-conducting substrate, where incoming electrons cannot be removed from the exposed area which then leads to charging effect in the writing process. To reduce charging effect the resist is coated with a thin ∼20 nm aluminum layer, giving the electrons a way to escape. The aluminum layer is then removed after the e-beam writing with a KOH solution.

Step 3. Development

The development is done in a MIBK:IPA 1:3 solution, where MIBK stands for Methyl IsoButyl Ketone and IPA is IsoPropyl Alcohol. The development time depends on the size of the structures and the thickness of the resist, and one must rely on experience or perform tests to ensure correct development. After the development, the sample is rinsed in IPA and blown dry with N_2.

Step 4. Coating

The developed sample was primarily coated in a Cryofox Explorer Electron-beam physical vapor deposition (EBPVD) system. In EBPVD, the source is heated with an electron beam at high energy and the target is placed at a distance above the source. It is line-of-sight deposition, ideally suited for EBL purposes as the sides of the developed structures will see very little coating. The coater is equipped with a thickness monitoring system and a control of the deposition rates for e-beam evaporation with 4 crucibles. A load-lock and a computer-control of the deposition process enable a fast and reliable method for coating of standard samples. Coating with non-standard materials was done in a Leybold coating chamber by resistive evaporation deposition. The chamber is equipped with a crystal balance to monitor the deposition rate, but allows only manual control of the evaporation current, demanding careful planing and constant monitoring.

Step 5. Lift-off

In the lift-off process the unexposed resist is removed including the coating on top, leaving only the defined structures on the substrate. This is done by dipping the sample into an ultrasonic bath of acetone. The lift-off time depends on several factors including the quality of the former steps. If all the processes have been successful, only the e-beam written structures are left on the surface.

Summary

EBL is a strong tool for producing nanostructures. With experience and attention to details in every single step, the method allows for precise formation of nanostructures, enabling testing of e.g. scattering properties or electronic properties of specific structures. The writing process is relatively slow

and might take 2-3 min for a single writing field depending on the structures written. It is especially well suited for small samples with a total writing area consisting of a few tens of writing fields. For large areas as the sample shown in D Fig.2, which consists of 437 writing fields, the total time can exceed 24 hours. Long writing time can induce problems due to small changes over time for both sample stage position, beam focus and beam current.

References

1. Morgen, P. *et al.* Roads to ultrathin silicon oxides. *Journal of Vacuum Science & Technology A* **23,** 201–207 (2005).
2. Campbell, C. T. Ultrathin metal films and particles on oxide surfaces: structural, electronic and chemisorptive properties. *Surface Science Reports* **27,** 1–111. ISSN: 0167-5729 (1997).
3. Lazzari, R. *et al.* Multipolar plasmon resonances in supported silver particles: The case of Ag/α-Al2O3(0001). *Phys. Rev. B* **65,** 235424 (23 June 2002).
4. Bachmann, L. & Shin, J. J. Measurement of the Sticking Coefficients of Silver and Gold in an Ultrahigh Vacuum. *Journal of Applied Physics* **37,** 242–246 (1966).
5. Van Campen, D. G. & Hrbek, J. Silver on Alumina: Adsorption and Desorption Study of Model Catalysts. *The Journal of Physical Chemistry* **99,** 16389–16394 (1995).
6. Kaplan, W. D., Chatain, D., Wynblatt, P. & Carter, W. C. A review of wetting versus adsorption, complexions, and related phenomena: the rosetta stone of wetting. *Journal of Materials Science* **48,** 5681–5717. ISSN: 1573-4803 (Sept. 2013).
7. Roy, A., Bhattacharjee, K., Ghatak, J. & Dev, B. Growth of epitaxially oriented Ag nanoislands on air-oxidized Si(111)-(7x7) surfaces: Influence of short-range order on the substrate. *Applied Surface Science* **258,** 2255–2265. ISSN: 0169-4332 (2012).

Chapter 5

Second harmonic generation experiments

5.1 Introduction

The original choice of material for the SHG spectroscopy of nanoparticles on Si was Ag, as its plasmon resonance response is very strong and at an interesting wavelength for solar cells. The results obtained have shown to be difficult to interpret. Au nanoparticles were then investigated and published in A. The results obtained with Au enabled the further interpretation of the results for Ag particles and those are presented in this chapter.

The first part of the chapter describes the experimental setup used for the SHG spectroscopy experiments. SHG spectroscopy measurements on Si with native oxide, Si with a thin oxide layer and Si with Ag nanoparticles at the surface are then presented.

5.2 Setup for second harmonic generation spectroscopy

The setup used in the SHG measurements is shown in Fig. 5.1. The samples were prepared and investigated in an ultra high vacuum (UHV) chamber with a base pressure below $10^{-8}\ Pa$. In the chamber, the sample can be heated by sending current through it and be exposed to oxygen in a controlled manner. Moreover, the chamber is equipped with a low energy electron diffraction

(LEED) setup to investigate the surface of the sample and with an evaporator to deposit material on the sample.

The primary laser system used in the SH experiments is a nanosecond system consisting of a Continuum Surelite II-10 Nd:YAG pump laser in combination with a tunable Continuum Surelite optical parametric oscillator (OPO) system. The OPO emits pulses of a duration of approximately 4 ns with 10 Hz repetition rate and photon energy tunable from around 0.9-1.7 eV and 1.8-2.42 eV, with degeneration around 1.75 eV.

A second laser system was also used for part of the Ag on silicon experiment. It is a femtosecond laser system based on a Spectra-Physics/Newport Tsunami Ti:Sapphire laser operating at 80 MHz and 786 nm. It is seeded into a Quantronix Integra-He amplifier system. The 1 kHz output is then fed into a Light Conversion Topas-C optical parametric amplifier (OPA), yielding an 1 kHz output tunable from 0.11 eV to 6.5 eV, with degeneration around 0.78 eV. This second laser system was used to cover the frequency range around the degeneration of the primary laser (∼1.75 eV), as the SH in this range coincide with a plasmon resonance of Ag and several substrate transitions.

In order to minimize the risk of damaging the nanoparticles on the surface the intensity of the laser can be reduced by using a $\lambda/2$-wave plate in combination with a polarizing beamsplitter, which also enables to control the polarization of the incidence light. High-pass filters before the sample separate the pump-beam from high energy light which can be falsely detected as SH, and likewise, low-pass filters separate the pump-beam from the SH before detection. A f=300 mm lens is used to focus the light on the sample, and again to collimate the light from the sample. Before detection a polarizing beamsplitter is used to select the polarization of the detected signal. The incidence angle of the light is 67°. The detection is done using a photomultiplier tube (PMT) connected to a boxcar averager. The signal is normalized using the SH front surface reflection from a quartz-crystal wedge as a reference signal.

For all experiments in this work, the silicon samples of 10x30 mm^2 are cut from (111)-oriented wafers and mounted inside the UHV chamber. The samples are oriented such that the plane of incidence of the light is parallel with the (110) direction of the crystal. This configuration ensures that only the isotropic contribution is detected for p to p polarization.

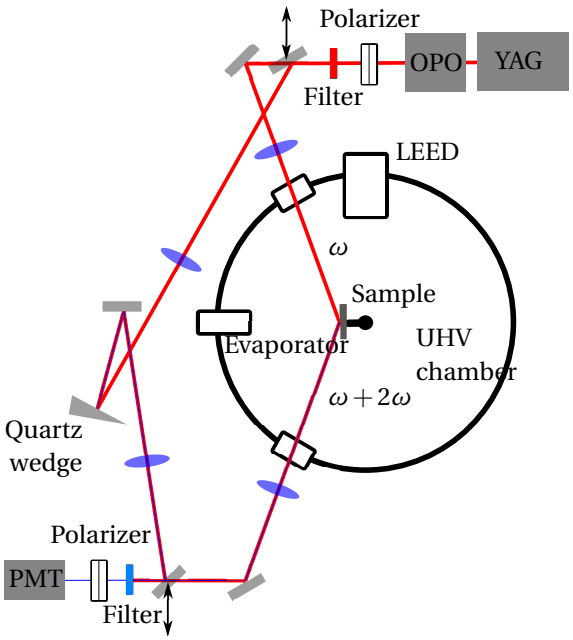

Figure 5.1: Schematic of the experimental setup used for SHG measurements. The light from the Topas-C OPA is inserted into the setup using adjustable mirrors not shown in the figure.

5.3 Second harmonic generation from silicon

5.3.1 Second harmonic generation from Si with native oxide

Figure 5.2 presents the $p \rightarrow p$ SH signal from a sample with the native oxide layer. The spectum shows four distinct resonances labelled E_1, E_{SiO}, $E_2(X)$ and $E_2(\Sigma)$. The E_1 and E_2 resonances are close to bulk Si transitions (see Fig. 3.5) and is related to the Si bonds close to the interface [1]. The E_1 is found at an energy of 3.27 eV, shifted from 3.4 eV due to strain at the interface [2]. Both $E_2(X)$ and $E_2(\Sigma)$ transitions are shifted as well, to 4.38 eV and 4.58 eV respectively, with $E_2(\Sigma)$ being the most pronounce of the two. The large resonance at 3.52 eV can be related to tilted Si-Si bonds due to oxidation at the Si interface [3]. The solid line in Fig. 5.2 is a modeling of the measured signal using Eq. 3.31, where the values for each resonance used in the model are presented in Tab. 5.1. A resonance also related to the Si-SiOx [4] interface labelled E'_{SiO} with an energy of 3.70 eV together with E'_1 (located outside the graph) are needed to get at good agreement between model and measured data.

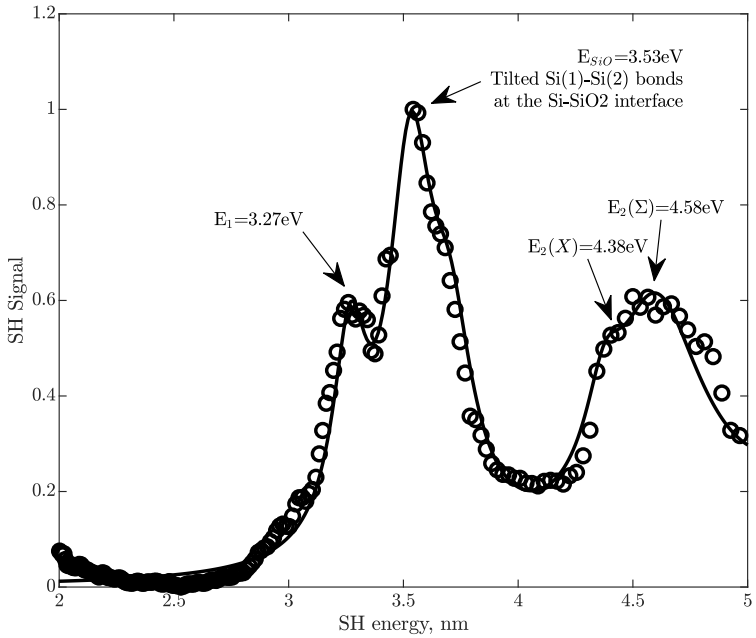

Figure 5.2: The black circles represent the measured p→p SHG from a Si surface with the native oxide. The black solid line is the modeling of the SH signal from the surface.

	ω_k [eV]	f_k	ϕ_k [rad]	γ_k [eV]
E_1	3.27	0.034	0	0.09
E_{SiO}	3.53	0.075	0.16π	0.12
E'_{SiO}	3.70	0.035	0.25π	0.12
$E_2(X)$	4.38	0.15	0.48π	0.1
$E_2(\Sigma)$	4.58	0.13	0.48π	0.25
E'_1	5.5	0.1	1.0π	0.2

Table 5.1: Parameters used in the model of the SH signal from Si with native oxide.

5.3.2 Second harmonic generation from Si with a thin oxide layer

The SHG from the Si surface with a thin oxide layer is presented in Fig. 5.3. There is a clear change in signal compared to the natural oxide. First of all, the strong E_{SiO} with an energy of 3.53 eV has now almost disappeared, and the signal is dominated by the E_1 and $E_2(\Sigma)$ transitions. This is also evident from the fitting values for the model of the signal presented in Tab. 5.2.

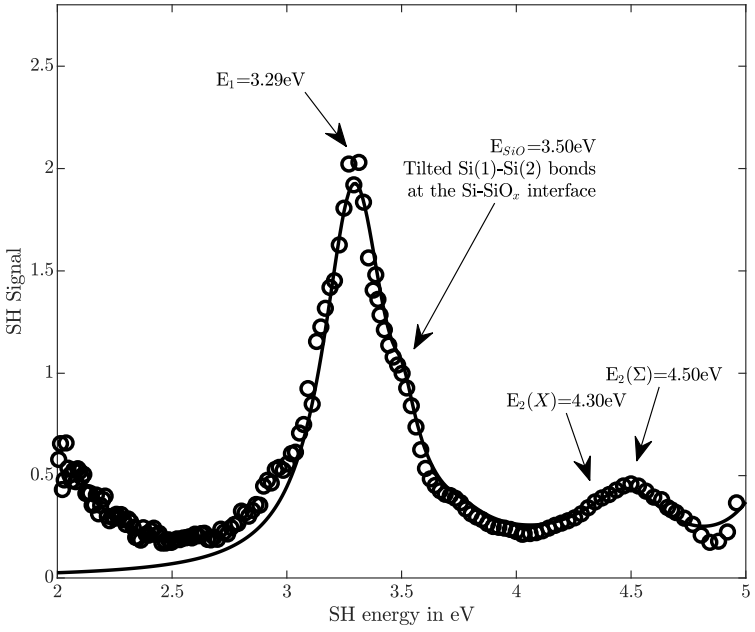

Figure 5.3: Second harmonic generation signal from Si with a thin oxide layer: the black circles represent the measurements while the solid black line is from the model.

	ω_k [eV]	f_k	ϕ_k [rad]	γ_k [eV]
E_1	3.29	0.235	0	0.17
$E_{1,bulk}$	3.39	0.0005	0	0.11
E_{SiO}	3.50	0.008	0.13π	0.06
E'_{SiO}	3.75	0.004	0.19π	0.06
$E_2(X)$	4.30	0.001	1.1π	0.15
$E_2(\Sigma)$	4.50	0.17	1.0π	0.23
E'_1	5.18	0.14	2.0π	0.2

Table 5.2: Parameters used in the model of the SH signal from Si with thin oxide layer.

The uncertainty of the parameters for the resonances $E_{1,bulk}$, E_{SiO}, E'_{SiO} and $E_(X)$ are large as they contribute very little to the signal. The $E_{1,bulk}$ (EFISH) transition is included in the model as it plays a role when metal is deposited on the surface. The increase in signal at low energy is not related to second harmonic generation, thus it is not included in the model. The origin of the signal is attributed to a combination of low signal to noise ratio and multiphoton luminescence within the system.

5.4 Silver nanoparticles on Si(111)

Prior to the publication of paper A, which addressed gold particles on a Si(111) surface, a system with Ag particles on a Si(111) surface was investigated. This proved to be a complicated system as a first attempt. In this section this system is revisited with the knowledge obtained from the Au system. The sample is measured in three stages: first, the SHG is measured just after making the sample, without removing it from the chamber. Second, the sample is removed from the UHV chamber and moved directly to the clean room where the linear measurements are performed. Last, the SEM images are obtained in the e-beam microscope. The analysis is then performed in reverse order, starting with the SEM images, then the linear measurements and finally the SHG investigation.

5.4.1 Sample preparation

The sample is prepared in a similar manner as the Au sample and is explained in detail in Sec. 4.2. The starting point is a Si(111) sample cut from a wafer,

which is mounted in the UHV chamber. While mounted inside the chamber the thin oxide layer (SiO_x) is created, following the procedure explained in subsection 4.2.1. On top of this well defined oxide layer the Ag is deposited using thermal evaporation with the deposition rate of 2 ML/s with a substrate temperature of 500°C. The rate of material deposition and total material deposited were measured using a quartz crystal microbalance (QCM). As shown in subsection 4.2.2 the result for Ag on the SiO_x surface are high almost spherical particles. The size of the particles are varied through the amount of Ag deposited on the surface, which is is controlled by moving the sample into the shadow of a screen during deposition. Hereby four areas with different size distributions where produced of the sample. SEM images and size distributions of each area are shown in Fig 5.4. Table 5.3 lists the results of the SEM analysis. In addition to the diameters the SEM analysis also provided the density of particles and the coverage in addition to the diameters. Both the density and the coverage, included in Table 5.3, are independent of the diameter and are related to the overall distribution.

5.4.2 Linear measurements

The linear optical properties are used to assist in the analysis of the SHG measurements. The linear measurements were performed with a Sentech SE 850 ellipsometer and resulted in two sets of data, each with different polarization setting, and the results are presented in Fig. 5.5(a) and Fig. 5.5(b). Both figures include measurements from each of the four different areas and they show the differential reflection defined as $(I-I_0)/I_0$, where I and I_0 are the intensity of the reflected light from the surfaces with and without Ag, respectively. In Fig. 5.5(a) the results of the modelling using the Island film approach is also presented as black dashed lines. Figure 5.5(a) shows the measurements using p-polarized incidence light and p-polarized detected light, whereas Fig. 5.5(b) shows s-polarized incidence and s-polarized detected light. There are three distinct features labelled A, B and C. The feature A is present in both figures and coincide with the onset of the indirect bandgap in Si, which adds backside reflection to the signal. The increase in reflection labelled B is present for both polarization configurations and can thus be related to the particle plasmon resonance parallel to the surface. The resonances position shows a red shift with increasing particle size. The decrease in reflection labelled C in Fig.

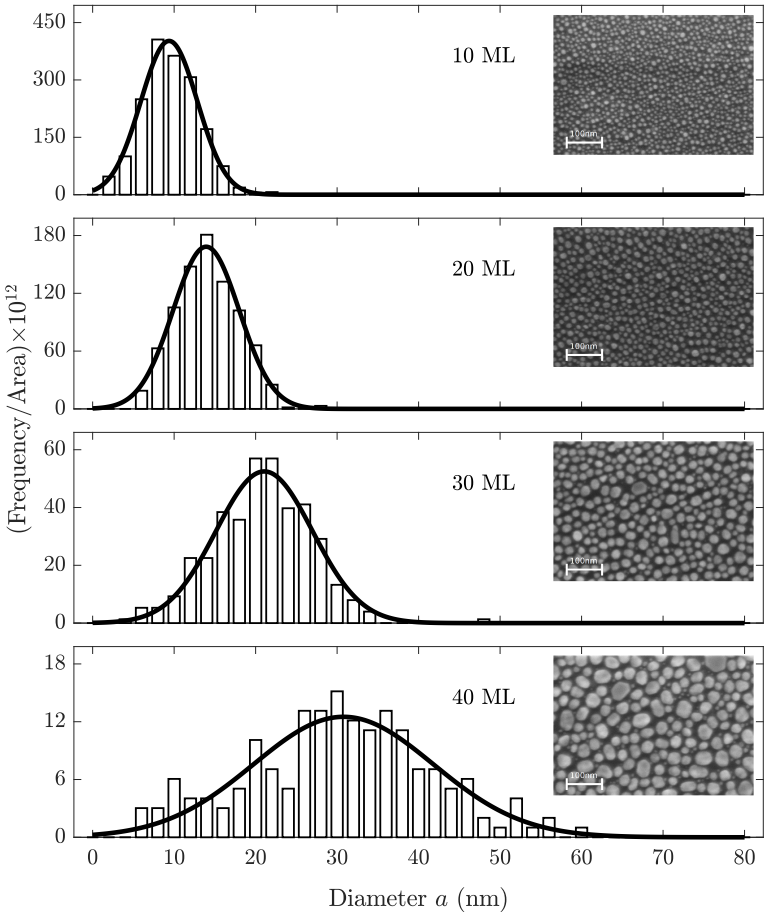

Figure 5.4: Nanoparticle size distributions from areas with 10 ML, 20 ML, 30 ML and 40 ML and corresponding SEM images.

Momolayers		10	20	30	40
Diameter	nm	9.4	13.9	21.1	30.8
Density	m^{-2}	$1.24e\times10^{15}$	6.03×10^{14}	1.97×10^{14}	6.48×10^{13}
Coverage		0.31	0.36	0.38	0.52
Height	nm	3.55	4.95	7.2	11.0
Resonance B	eV	2.8	2.6	2.5	2.4
Resonance C	eV	3.3	3.4	3.45	3.45
FWHM C	eV	0.57	0.45	0.45	0.43

Table 5.3: Particle diameter, particle height, density, and silver coverage for each area on the sample. The position of the plasmon resonance for both the parallel and the perpendicular directions and the full width at half maximum (FWHM) for the perpendicular resonance are also listed.

5.5(a) is not present in Fig. 5.5(b) and is identified as the particle plasmon resonance perpendicular to the surface. The resonance position shows a blue shift with increasing particle size. The position of the two plasmon resonances are coverned by the shape and size of the particles, as well as electromagnetic coupling with the substrate and particle-particle interaction [5, 6]. The particle diameter and the density of particles are obtained from the SEM analysis. Those parameters are introduced in the modelling of the p-p polarization and the particle height and the relaxation time, both unknown, are used as fitting parameters.

In Table 5.3 the resonance position of α and γ for each area is shown, together with the corresponding particle heights obtain from the model. The height obtained from fitting the model with the measurements corresponds to approximatively 40% of the amount of deposited Ag measured by the QCM. This discrepancy could be explained by the desorption of adatoms under the deposition process (see subsection 4.2.2). It could also be due to the fact that sharper edges on the particles induces similar consequence on the surface plasmon resonances as lowering the particle height, resulting in artificial lower values of the particle height when determining it from the plasmon frequency.

5.4.3 Second harmonic generation measurements

Figure 5.6 shows the measured SHG from both a clean SiO_x surface (0 ML) and with increasing Ag deposition (10 ML - 40 ML). In each graph the measured intensity is represented with black circles and the modelled intensity is the black

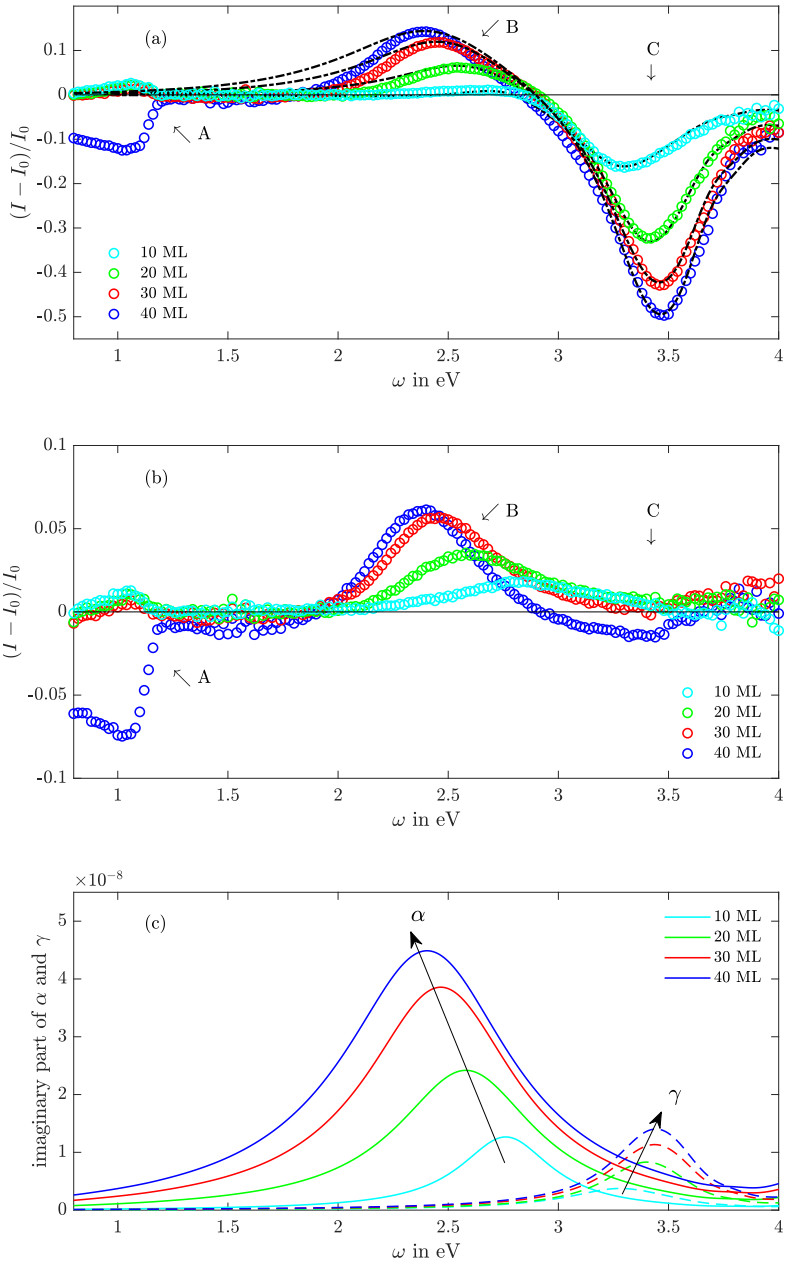

Figure 5.5: (a) Differential reflection intensity for p- to p-polarization, (b) differential reflection intensity for s- to s-polarization and (c) the imaginary part of the parallel and the perpendicular surface susceptibilities (α and γ) with arrows indicating the shift in resonance energy.

solid line. The green line represents the contribution from the substrate and red line the contribution from the Ag particles.

The presence of Ag particles has a clear effect on the SH spectra measured, as shown in Fig. 5.6, mostly as a large increase in the SH signal intensity. The spectra are still dominated by two features around the E_1 and E_2 Si bulk transitions. Already at 10 ML of Ag there is a jump in peak position of the resonances. As observed for Au particles (see Pap. A) the E_1 peak is shifted from 3.29 eV (surface energy) to 3.40 eV (bulk energy), and similar for the E_2 peak from 4.50 eV ($E_2(\Sigma)$) to 4.34 eV ($E_2(X)$). As the black solid line indicates, there is a good agreement between measurement and modelling. Through the modelling it is possible to separate the SH measured signal into the substrate and the Ag contributions. They are presented in Fig. 5.6 as green and red solid lines, respectively, where the Ag contribution has been multiplied by a factor 5 for better visualization. It is seen that the direct contribution from the Ag particles to the SH signal is relatively low, but it increases with increasing deposition. In particular on the 30 ML and 40 ML graphs, both the horizontal plasmon around 2.5 eV and the perpendicular plasmon around 3.4 eV can be identified, in line with the linear measurements (see Fig 5.5). The perpendicular plasmon resonance, and the E_1 and E_{SiO} resonances are all positioned close together, and this overlap was the original motivation to switch to Au particles where the resonances are further apart, enabling an almost individual treatment of metal and substrate contributions. However, this separation is not possible for Ag particles.

Modelling

Equation 3.31 is used to model the signal. The SH signal resembles that of the Si substrate, and thus the starting point of the modelling is the optimization of the Substrate contributions and then, the Ag particle contribution is introduced. We will concentrate on the energies close to the E_1 transition, namely $E_{1,Surf}$, $E_{1,bulk}$ and E_{SiO}, as these are the energies which are most affected by the presence of silver.

In paper A we succeeded by treating the two resonances related to E_1 as one and optimize the resonance position and phase. The resonance at E_1 in Figure 5.6 (30 ML) and -(40 ML) has a flat top, suggesting that combining the two is not possible with Ag particles and $E_{1,Surf}$ and $E_{1,bulk}$ must be included as individual resonances. The substrate contributions are modelled primarily by

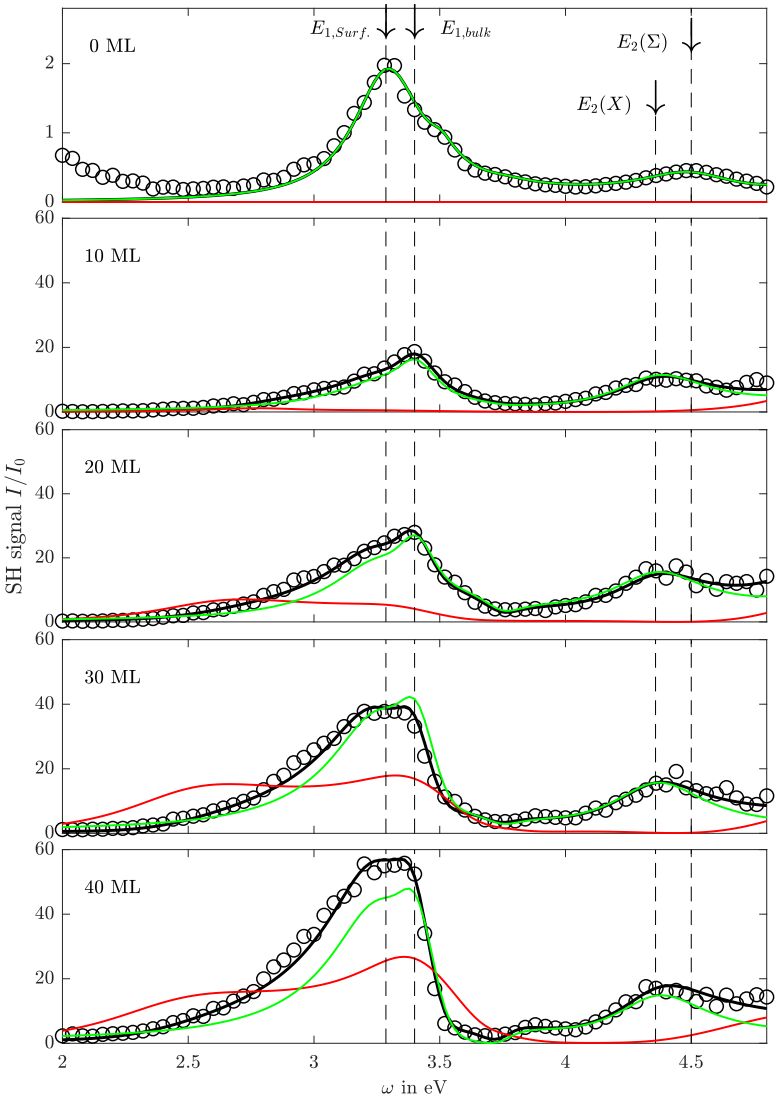

Figure 5.6: SH spectra for p- to p-polarization. Both measured (open black markers) and modelled spectra (black lines) are shown. SH spectra for different amount of monolayers of Ag deposited ranging from 10 ML to 40 ML are shown. The 0 ML SH spectrum corresponds to the clean SiO_x surface. The green and red lines show the different contributions to the SH signal obtained from the model: (red line) Ag contribution, which is multiplied by a factor of 5 to better discern the features, (green line) combined $E_{1,Surf}$ and $E_{1,bulk}$ contribution to the SH signal.

optimizing the amplitude (f_n) and the phase (ϕ_n) of the resonance. The width (γ_n) and resonance energy (ω_n) of the interface resonances, $E_{1,Surf}$ and E_{SiO}, are also optimized as they might change due to silver deposition. The $E_{1,bulk}$ width and resonance energy should be fixed as they are bulk values and are not affected by silver deposition. For simplicity the E_2 resonances are treated as one, and the remaining resonances, $E_{SiO'}$ and E_1', must also be included in the model as they contribute to the final results.

Following the initial modelling of the surface contributions, the silver particle contributions are introduced. As described in subsection 3.2.6 the modified dielectric function (Eq. 3.42) and the local fields factors (Eq. 3.40 and 3.39) of the Ag particles are determined from the SEM investigations and the results from the linear measurements. This simplifies the modelling of the SH generation of the present system to the problem of finding the three Rudnick and Stern parameters for each polarization (see Eq. 3.28). As with the substrate contributions, the parameters are found by optimization.

The modelling is then performed by alternating between optimizing the surface and silver particle contributions, until the modelling converges.

Metal contributions

Fig. 5.7 shows the Rudnick and Stern parameters used in the modelling as a function of particle diameter. The black crosses represent the absolute value of the parameters and the red circles represent the phase. The $a_{\parallel\perp\parallel}$ and $a_{\perp\perp\perp}$ parameters describe the parallel and vertical surface currents, respectively. In many cases the two currents are sufficient to describe the observed signal [7, 8]. With the sample geometry with Ag particles on a silicon substrate this proved to be insufficient. The contribution from $P_{\perp\parallel\parallel}$ is found to be quite significant as seen in the absolute value of the $a_{\perp\parallel\parallel}$ parameter, which is an order of magnitude larger than the values found for gold particles in paper A. The value of $a_{\perp\perp\perp}$ is known to depend strongly on surface configuration [8–10]. For Aluminium particles the value ranges from around 0 up to 37 depending on surface configuration [10]. For Au particles values of up to 56 were found as presented in paper A. The surface structures has also a clear effect on all the a parameters.

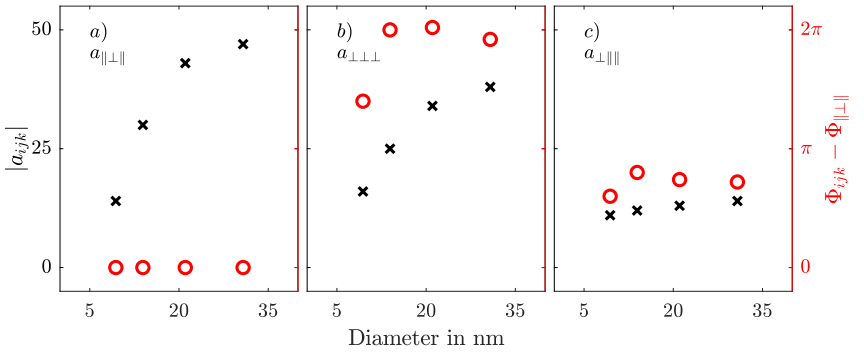

Figure 5.7: Rudnick and Stern parameters obtained from the model as a function of the particle diameter: (black cross markers) Absolute value and (red circle markers) phases relative to the phase of $a_{\parallel\perp\parallel}$.

Substrate contributions

Table 5.4 shows the result of the modelling for three resonances of interest. Already after deposition of 10 monolayers of silver, an immediate jump in the resonance position to a value of ∼3.4 eV is seen, which suggests that the deposited silver creates a SCR and enables an EFISH signal. In the model the EFISH contribution is represented by $E_{1,bulk}$, and as expected, the value obtained from the optimization for both the resonance energy and the width is very close to the bulk value for Si. The optimization did not change the resonance energy of the interface resonances ($E_{1,Surf}$ and E_{SiO}) and they retain the values from the SiO_x modelling. The width of both interface resonances increased during the optimization.

According to Rumpel et al. [11], an EFISH resonance in phase with the E_1 surface resonance corresponds to a positive SCR, whereas a phase different of π corresponds to a negative SCR. The relative phase of the EFISH contribution obtained in this experiment shows a value of $\sim 1.8\pi$ for all sample areas, thus suggesting that a positive SCR is created very early in the deposition process. Additionally, the relative phase difference between the $E_{1,bulk}$ and E_{SiO} resonance is close to π and can be coupled to the sharp decrease in signal between the two energies, which is especially apparent for 40 ML of silver deposition.

	0 ML	10 ML	20 ML	30 ML	40 ML
$E_{1,Surf}$					
ω [eV]	3.29	3.29	3.29	3.29	3.29
f	0.235	0.690	0.984	1.44	1.79
ϕ [rad]	0	π	0.92π	0.99π	1.09π
γ [eV]	0.17	0.20	0.20	0.20	0.20
$E_{1,bulk}$					
ω [eV]	3.39	3.39	3.39	3.39	3.39
f	0.0005	0.377	0.502	0.615	0.803
$\phi - \phi_{E_1,surf}$	0	1.85π	1.78π	1.80π	1.86π
γ [eV]	0.11	0.11	0.11	0.11	0.11
E_{SiO}					
ω [eV]	3.53	3.50	3.50	3.50	3.50
f	0.008	0.0780	0.168	0.435	0.872
$\phi - \phi_{E_1,surf}$	0.13π	3.05π	3.08π	2.94π	2.98π
γ [eV]	0.06	0.12	0.12	0.12	0.12

Table 5.4: Parameters for selected resonances used in the model to fit the measured SH signal from Si with Ag nanoparticles.

With respect to the amplitudes, f, of the resonances, the values obtained from the modelling are also shown in Tab. 5.4. For the EFISH transition, it is the amplitude of the effective second-order susceptibility tensor $\chi^{(2)}_{eff}$ (see Eq. 3.30). For the interface transitions, the amplitude represents the product of $L_{eff,n}$ and f_n, and thus contains the field factors for both the electric fields at ω and 2ω. In Fig. 5.8 the contributions from each resonance have been extracted from the modelling and presented together with the measured signal. Already at 10 ML the SCR is created, and at this stage the EFISH contribution is larger than the $E_{1,Surf}$ contribution. With increasing silver deposition both the $E_{1,Surf}$ and EFISH contributions continue to grow, with $E_{1,Surf}$ growing at a greater rate. This difference can be understood through the origin of the two contributions. Tunneling of electrons from a silicon substrate through a thin oxide to Sn particles has previoulsy been shown from photoemission studies of Sn nanoparticles [12]. In this study, they also observed that the band bending resulting from the tunneling of electrons increased with metallic surface area and total surface charge, levelling out at high coverage with 10 ML deposited.

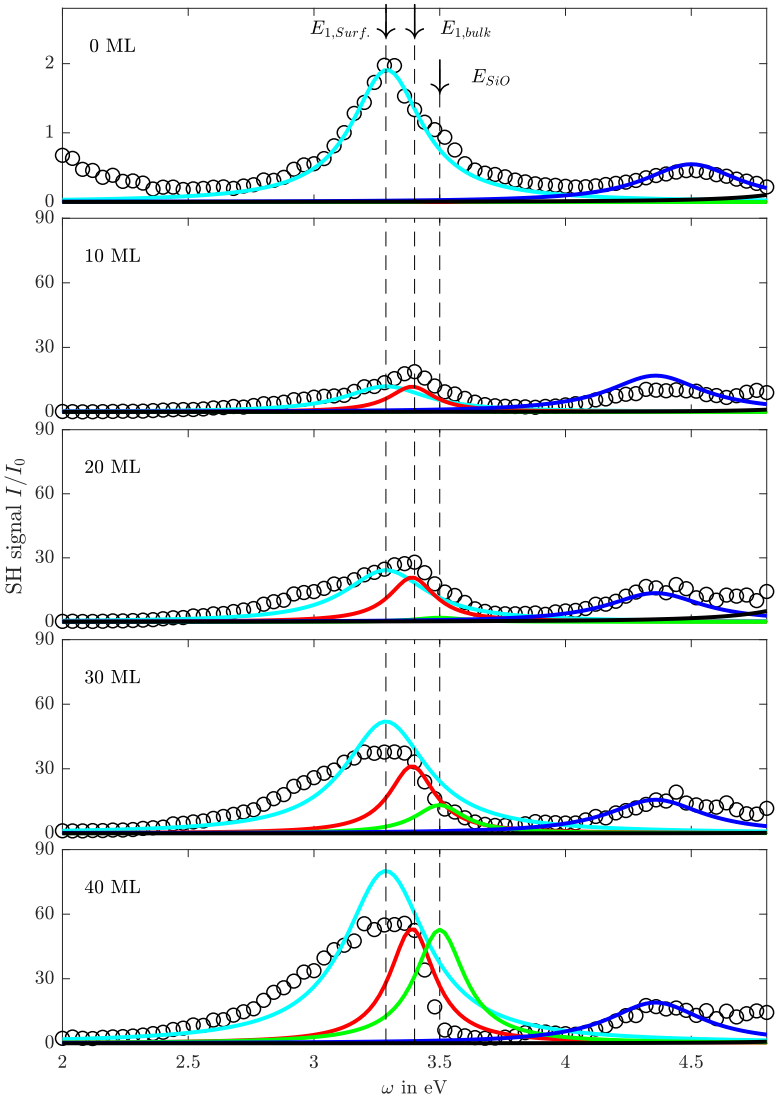

Figure 5.8: The open black markers show the measured SH spectra for p- to p-polarization. 0 ML is the SH spectrum from clean SiO_x surface and 10 ML-40 ML are SH spectra from areas with 10-40 monolayers of deposited silver. The cyan, red, green, blue and black lines represent the contribution from $E_{1,Surf}$, $E_{1,bulk}$, E_{SiO_x}, E_2 and E_1', respectively.

In [12] a band bending of 0.40 eV is reported, which corresponds approximatively to the value obtained for a clean Si(111) 7x7 surface with a space charge region depth of ∼730 nm. In the present work on Ag particles 10 ML corresponds to the minimum amount of Ag deposited. The band bending seems to have saturated which can be explained by the build up of charges on the particles preventing more electrons to tunnel through the oxide layer. This barrier is constant as the particles become larger.

As reported in [13] the EFISH intensity depends both on the band bending and on the penetration depth of the pump and SH fields. When the penetration depth is significantly shorter than the depth of the SCR, the EFISH intensity depends linearly on the band bending. It was shown in [14] that the penetration depth of light in silicon is ∼15 μm for 1.65 eV, ∼25 nm for 3.3 eV and ∼10 nm for 3.4 eV photons, which indicates that the EFISH contribution originates from the first few tens of nanometres in the Si substrate for which the DC field from the SCR can be considered constant.

As for Au particles in paper A the field enhancement from the silver particles is expected to be located at an even shorter range, such that $L(z)$ is limited to a few nanometres into the silicon substrate [15, 16]. The interface contribution to the SH signal is expected to be favored with respect to the bulk like EFISH part when silver particle are present.

In Fig. 5.9(a) the enhancement factor ($|L_{eff}|^2$) for the $E_{1,surf}$ is presented and is found to scale liniarly with particle diameter. The results are obtained via the modelling, as explained in subsection 3.2.5, containing the contributions from both the electric fields at ω and at 2ω. It is shown that the enhancement factor increases the strength of the field enhancement. The increase is limited when comparing it with other experiments with metallic particles as field enhancers[17–22]. Compared to the work in paper A with gold particles, the increase is significant. In both experiments the amount of metal deposition is comparable, but the maximum enhancement factor is 58 and 3.3 for silver and gold, respectively. This was expected due to the difference in the plasmon resonance position and the difference in the strength of the plasmon resonance for the silver and gold particles.

A surprising result of the modelling was the large increase of the SiO resonance at 3.50 eV, especially for 30 ML and 40 ML Ag deposited. As explained above, the sharp decrease in signal starting ∼3.4 eV is explained by an $\sim \pi$ phase difference between the $E_{1,bulk}$ and E_{SiO} resonances. The increasing strength of E_{SiO} also increases the effect of interference with the EFISH contribution, thus enhancing the drop in the signal.

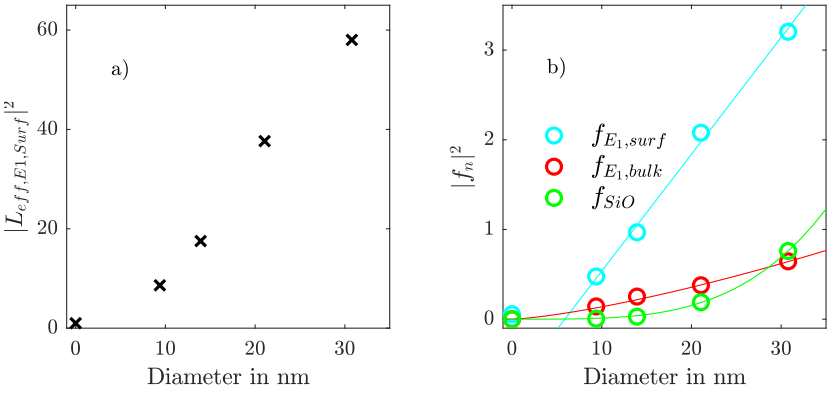

Figure 5.9: (a) Enhancement of the $E_{1,Surf}$ resonance as a function of particle diameter. (b) Amplitude squared of the $E_{1,Surf}$, $E_{1,bulk}$ and E_{SiO_x} resonance as a function of particle diameter.

The enhancement factors are calculated by comparing the amplitudes from the silver samples with the amplitudes from the SiO_x modelling, and they describe the enhancement due to local fields. For the SiO_x signal both the $E_{1,bulk}$ and the E_{SiO} contributions are very small and associated with large uncertainties. Changes in the EFISH contribution is not only due to field enhancements, but also to the strength of the SCR. Moreover, the width of E_{SiO} was found to change significantly compared to the SiO_x value. By trying to calculate the enhancement factors a value of ~2.6e6 and ~1.2e4 for $E_{1,bulk}$ and E_{SiO} is found, respectively. These values do not represent the enhancement factor as defined by Eq. 3.29 and are associated with large uncertainties.

To compare the different contributions, the amplitudes of $E_{1,Surf}$, $E_{1,bulk}$ and E_{SiO} are presented in Fig. 5.9 (b) as a function of particle diameter. The figure shows how local field enhancements favor interface resonances as the $E_{1,surf}$ increases faster than the EFISH contribution. Both the $E_{1,surf}$ contribution and the EFISH contribution appear to scale linearly with particle diameter. Within the span of particle diameters investigated here, the E_{SiO} does not follow the same linear trend of increasing with particle diameter.

$E_{1,Surf}$ and E_{SiO} are both interface transitions and are thus easier to compare. With increasing diameter, the perpendicular plasmon moves from 3.3 eV ($E_{1,surf}$) to 3.45 eV (close to E_{SiO}) while increasing in strength. The FWHM of the plasmon resonances is wide (see Tab. 5.3) both compared to the change

in plasmon resonance and to the width of both $E_{1,surf}$ and E_{SiO}. Given the information above, the immediate expectations are for the two resonances to evolve the same way. The apparent behaviour of the f_{SiO} amplitude is different than the others and has yet to be explained.

5.5 Summary

This chapter presented the SHG studies performed on Ag particles deposited on Si(111). In this work, second harmonic generation spectroscopy studies of Ag particles on Si substrate with a thin 1 nm thick surface oxide were performed. Field enhancements from Ag particles of different sizes (diameters of 9 to 30 nm) were measured and modelled. Those studies were originally performed before the Au study presented in paper A, but proved to be more complicated to interpret. The knowledge gained through the Au study helped in analysing the Ag data and drawing the conclusions presented in this chapter.

A horizontal plasmon resonance near ∼2.5 eV and a perpendicular plasmon near ∼3.4 eV were identified from results from linear optical spectroscopy. Those values were used as inputs for different parameters and properties in the model, which include the local field factors, optical properties, and absorption and transmission of the silver island layer.

The SHG signal from the silver samples are dominated by resonances close to the E_1 and E_2 bulk transitions of Si, but with a much larger signal. The field enhancement in the Si Surface induced by the presence of the silver nanoparticles was obtained by following the evolution of the characteristic SHG Si resonance near the E_1 point. The silver nanoparticles affect the SHG signal near the E_1 resonance both through charge transfer from the substrate to the metal and through enhancement of the field at the Si-oxide interface. The EFISH signal was found to dominate for small particles where charge transfer modifies the band bending in Si. The local fields increase with increasing particle size; the Si-oxide interface dominates the SH signal for larger particles.

References

1. Daum, W. Optical studies of Si/SiO2 interfaces by second-harmonic generation spectroscopy of silicon interband transitions. *Applied Physics A* **87,** 451–460. ISSN: 0947-8396 (2007).

2. Daum, W., Krause, H.-J., Reichel, U. & Ibach, H. Identification of strained silicon layers at Si-SiO_2 interfaces and clean Si surfaces by nonlinear optical spectroscopy. *Phys. Rev. Lett.* **71,** 1234–1237 (8 Aug. 1993).
3. Bergfeld, S., Braunschweig, B. & Daum, W. Nonlinear Optical Spectroscopy of Suboxides at Oxidized Si(111) Interfaces. *Phys. Rev. Lett.* **93,** 097402 (9 Aug. 2004).
4. Erley, G. & Daum, W. Silicon interband transitions observed at Si(100)-SiO_2 interfaces. *Phys. Rev. B* **58,** R1734–R1737 (4 July 1998).
5. Yamaguchi, T., Yoshida, S. & Kinbara, A. Optical effect of the substrate on the anomalous absorption of aggregated silver films. *Thin Solid Films* **21,** 173–187. ISSN: 0040-6090 (1974).
6. Martin, D., Jupille, J. & Borensztein, Y. Silver particle sizes and shapes as determined during a deposit by in situ surface differential reflectance. *Surface Science* **402-404,** 433–436. ISSN: 0039-6028 (1998).
7. Wang, F. X. *et al.* Surface and bulk contributions to the second-order nonlinear optical response of a gold film. *Phys. Rev. B* **80,** 233402 (23 Dec. 2009).
8. Bachelier, G. *et al.* Origin of optical second-harmonic generation in spherical gold nanoparticles: Local surface and nonlocal bulk contributions. *Phys. Rev. B* **82,** 235403 (23 Dec. 2010).
9. Liebsch, A. Second-Harmonic Generation at Simple Metal Surfaces. *Phys. Rev. Lett.* **61,** 1233–1236 (10 Sept. 1988).
10. Teplin, C. W. & Rogers, C. T. Experimental example of isotropic surface second-harmonic generation: dc-sputtered air-exposed aluminum thin films. *Phys. Rev. B* **65,** 245408 (24 May 2002).
11. Rumpel, A., Manschwetus, B., Lilienkamp, G., Schmidt, H. & Daum, W. Polarity of space charge fields in second-harmonic generation spectra of Si(100)/SiO2 interfaces. *Phys. Rev. B* **74,** 081303 (8 Aug. 2006).
12. Silva, A. G., Pedersen, K., Li, Z. S. & Morgen, P. Photoelectron spectroscopy as an in situ contact-less method for studies of MOS properties of ultrathin oxides on Si. *Applied Surface Science* **353,** 1208–1213. ISSN: 0169-4332 (2015).
13. Ohlhoff, C., Lupke, G., Meyer, C. & Kurz, H. Static and high-frequency electric fields in silicon MOS and MS structures probed by optical second-harmonic generation. *Phys. Rev. B* **55,** 4596–4606 (7 Feb. 1997).

14. Vuye, G. *et al.* Temperature dependence of the dielectric function of silicon using in situ spectroscopic ellipsometry. *Thin Solid Films* **233,** 166–170. ISSN: 0040-6090 (1993).

15. Jung, J. *et al.* Dyadic Green's functions of thin films: Applications within plasmonic solar cells. *Phys. Rev. B* **83,** 085419 (8 Feb. 2011).

16. Hao, E. & Schatz, G. C. Electromagnetic fields around silver nanoparticles and dimers. *The Journal of Chemical Physics* **120,** 357–366 (2004).

17. Qian, X.-M. & Nie, S. M. Single-molecule and single-nanoparticle SERS: from fundamental mechanisms to biomedical applications. *Chem. Soc. Rev.* **37,** 912–920 (5 2008).

18. Stiles, P. L., Dieringer, J. A., Shah, N. C. & Van Duyne, R. P. Surface-Enhanced Raman Spectroscopy. *Annual Review of Analytical Chemistry* **1.** PMID: 20636091, 601–626 (2008).

19. Kneipp, J., Kneipp, H. & Kneipp, K. SERS-a single-molecule and nanoscale tool for bioanalytics. *Chem. Soc. Rev.* **37,** 1052–1060 (5 2008).

20. Wokaun, A. *et al.* Surface second-harmonic generation from metal island films and microlithographic structures. *Phys. Rev. B* **24,** 849–856 (2 July 1981).

21. Boyd, G. T., Rasing, T., Leite, J. R. R. & Shen, Y. R. Local-field enhancement on rough surfaces of metals, semimetals, and semiconductors with the use of optical second-harmonic generation. *Phys. Rev. B* **30,** 519–526 (2 July 1984).

22. Tsuboi, K. *et al.* Second-harmonic spectroscopy of surface immobilized gold nanospheres above a gold surface supported by self-assembled monolayers. *The Journal of Chemical Physics* **125,** - (2006).

Paper A

Field enhancement at silicon surfaces by gold ellipsoids probed by optical second-harmonic generation spectroscopy

List of authors:

Hans Ulrik Ulriksen
Kjeld Pedersen

The paper has been published in the
Journal of applied physics Vol. 120, pp. 235307, 2016.

The layout has been revised.

JOURNAL OF APPLIED PHYSICS **120**, 235307 (2016)

Field enhancement at silicon surfaces by gold ellipsoids probed by optical second-harmonic generation spectroscopy

Hans Ulrik Ulriksen and Kjeld Pedersen[a)]
Department of Physics and Nanotechnology, Aalborg University, Skjernvej 4A, 9220 Aalborg East, Denmark

(Received 1 September 2016; accepted 30 November 2016; published online 20 December 2016)

Optical second-harmonic generation (SHG) spectroscopy has been used to determine the field enhancements from Au nanoparticles on a silicon substrate. Au particles with diameters from 30 to 250 nm have been deposited on a Si substrate passivated by a 1 nm thick surface oxide. The linear optical spectra are dominated by a horizontal plasmon resonance near 1.0 eV, and the experimental spectra are modelled by the island film model in order to extract the linear properties of the metal particles. SHG spectroscopy from this system shows resonances from the metal particles and from the silicon/oxide substrate. By following the evolution of these Si resonances with the size of the Au particles, the field enhancement in the Si surface has been modelled. The effect of the Au particles on SHG at the Si E_1 resonance is a combination of charge transfer through the thin oxide that changes the space charge region and an enhancement of the optical field in a thin surface layer of the Si substrate. *Published by AIP Publishing*. [http://dx.doi.org/10.1063/1.4972190]

I. INTRODUCTION

One of the promising applications of nanoplasmonics is the design of metallic structures that can enhance optical fields in the surrounding media at specific wavelengths. Both size and shape of the nanostructures can be used to tailor resonances to specific applications.[1] Raman scattering spectroscopy enhanced by plasmonic resonances is becoming a well-established technique in chemical and bio-medical sensing where sensitivities down to the single molecule level may be reached.[2–4] This is made possible by the fourth power dependence of the Raman signal on the enhancement of the incident optical field at the surface where the molecules are placed. Another application of surface field enhancements by plasmons that has been studied intensely over the past decade is the enhanced light absorption in solar cells.[5,6] Increased light absorption is particularly important for thin film cells, organic as well as inorganic, where the thin active layer has a poor light absorption compared to thicker cells.[7,8] Excitation of plasmons in metal particles placed near the active layer may lead to strong light scattering, increasing the optical path through the layer, and to strong fields near the metal particles that localize the field in the active layer. More than 50% enhancement of the photocurrent in Si thin film cells has been reported.[8] Various geometries of the metal structures have been investigated with sizes in the range of 50–100 nm giving an optimal compromise between absorption and scattering.

Nonlinear processes are particularly interesting in relation to investigations of field enhancements of the driving field. Early investigations of surface enhanced second harmonic generation (SHG) performed on roughened surfaces and island films showed up to 3 orders of magnitude intensity enhancement attributed to local fields.[9,10] More recent spectroscopic investigations of SHG and third-harmonic generation (THG) from metal particles have identified plasmon resonances around harmonic wavelengths of 270 nm in Ag particles separated from a Si surface by oxide layers of varying thickness to demonstrate the effect of the effective refractive index of the substrate.[11] Up to 5 orders of magnitude enhancement of SHG from Au particles arranged as a self-assembled monolayer (ML) with a gap of 0.8 nm to a Au substrate has been demonstrated.[12] The strong frequency dependence of the enhancement indicates that localized plasmons are the source of the enhancement. While these spectroscopic SHG investigations are focused on signals from the metal particles, the present work uses SHG spectroscopy to investigate field enhancements in a Si surface resulting from Au particles placed on top of the surface. The metal particles are isolated from Si by a very thin surface oxide (1 nm). The metal particles are then as close as possible to the substrate without a direct contact - an arrangement one would seek in a solar cell. Oxide covered silicon surfaces have a number of well-known resonances in SHG spectroscopy. The basic idea in this work is to follow the evolution of the Si resonances, in particular, the resonances associated with the E_1 critical point, as a function of the size of Au nano-particles in order to deduce the enhancement of the fields in the Si surface layer. The theoretical background for the analysis of linear and SH spectra is presented in Section II. The experimental setup is presented in Section III. In Section IV, experimental spectra recorded for various particle sizes are presented along with the fits of the theoretical models, and the analysis of the results is discussed in Section V.

II. THEORY

A. Second-harmonic generation spectroscopy

Second-harmonic generation has for many years been used to investigate the surface and interface properties of semiconductors and multilayered structures. The second harmonic (SH) signal from Si surfaces and Si/SiO_2 interfaces

[a)]Electronic mail: kp@nano.aau.dk

has been studied and is well described in Refs. 13–15. Generally the SH signal is expressed via an interface polarization $P_i^{(2)}$ at twice the pump frequency given by[15,16]

$$P_i(2\omega) = \chi_{ijk}^{(2)}(2\omega)E_j(\omega)E_k(\omega), \tag{1}$$

where $E(\omega)$ is the optical field of the pump-laser at the interface at frequency ω, and $\chi_{ijk}^{(2)}$ is the second-harmonic susceptibility tensor of the interface. The SHG spectrum from a Si surface has two main features originating from E_1 (∼3.3 eV) and E_2 (∼4.4 eV) interband transitions in Si. Resonances near the E_1 transition often appears as two distinct resonances,[15,17] an electric field induced part from the space charge region (SCR) appearing at the bulk E_1 transition at 3.4 eV, and a surface contribution shifted down in energy to ∼3.3 eV. Furthermore, a broader feature associated with the Si oxide interface (3.7 eV) and the E'_1 (5.3 eV) transition contribute to the spectra. The measured SHG spectrum from these transitions can be modelled as[15]

$$I(2\omega) \propto \left| \sum_{k=1}^{n} \frac{f_k(\theta,\omega)\exp(\imath\phi_k)}{2\omega - \omega_k + \imath\Gamma_k} \right|^2, \tag{2}$$

a superposition of n resonances each with a resonance frequency ω_k, an amplitude $f_k(\theta, \omega)$ which is a function of both incidence angle and frequency, a phase ϕ_k, and a width Γ_k.

B. Second-harmonic generation from metallic nanoparticles

A large SH signal from small metal particles was first observed and associated with local surface-plasmons in the early 1980.[9,18] The SH polarization of small metal particles is given by[11]

$$P_{Au}(2\omega) = L_{2\omega}\chi_{Au}^{(2)}(2\omega)L_\omega^2 E^2(\omega), \tag{3}$$

where $E(\omega)$ is the optical field of the pump-laser at frequency ω, $\chi_{Au}^{(2)}$ is the effective SH susceptibility of the metal, and L_ω and $L_{2\omega}$ are the local field factors at frequency ω and 2ω, respectively. In the dipole approximation, the local field factors are given by[11]

$$L(\omega) = \frac{\epsilon_d(\omega)}{\epsilon_d(\omega) + [\epsilon_m(\omega) - \epsilon_d(\omega)]M}, \tag{4}$$

where ϵ_d and ϵ_m are the dielectric constants of the matrix and the metal, respectively, and M is the shape-dependent depolarization factor of the metal particles.

In the present work, the nanoparticles are disk-shaped with a large diameter to height ratio, and they are situated on a Si surface. We therefore treat the particles as disks with negligible heights and only one large surface (see Fig. 4(a)). With this assumption, the surface SH polarization reduces to three contributions[19]

$$\begin{aligned} P_\parallel(2\omega) &= P_{\parallel\perp\parallel}(2\omega) \\ P_\perp(2\omega) &= P_{\perp\perp\perp}(2\omega) + P_{\perp\parallel\parallel}(2\omega), \end{aligned} \tag{5}$$

where $P_\parallel$ and $P_\perp$ are the total parallel and perpendicular SH polarization. Each term in Eq. (5) takes the form

$$P_{ijk}(2\omega) = L_i(2\omega)\chi_{ijk}^{(2)}(2\omega)L_j(\omega)E_j(\omega)L_k(\omega)E_k(\omega), \tag{6}$$

where i, j, and k can represent the parallel or perpendicular directions. The local field factors $L_i(2\omega)$, $L_j(\omega)$, and $L_k(\omega)$ are obtained from Eq. (4). The tensor elements $\chi_{ijk}^{(2)}$ in Eq. (6) can be calculated using the classical form for the surface of a semiinfinite system[20,21]

$$\chi_{ijk}^{(2)} = -\frac{a_{ijk}}{2}[\epsilon_m(\omega) - 1]\frac{e\epsilon_0}{m\omega^2}. \tag{7}$$

Again ϵ_m is the dielectric function of the metallic particles and is modified to take into account, the size and shape effects. The constants $a_{\parallel\perp\parallel}$ and $a_{\perp\perp\perp}$ are the Rudnick and Stern parameters which are related to the parallel and vertical surface currents, respectively. The values of these parameters can be both complex and frequency dependent.[20,22] The $P_{\perp\parallel\parallel}$ term is often left out in the literature as it is considered very weak for plane surfaces,[23] but we keep it in our model as we have found its contributions to be significant for the gold particle covered surface.

C. Metal particle effects on SHG from silicon

As mentioned above, the signal from a clean Si/SiO_2 interface is well understood and can be modelled by Eq. (2). The metallic particles enhance the local electric fields, both the pump-field and the generated SH field. The metallic particles also change the reflection and transmission properties of the interface and absorb light. The combined effect of the local field enhancement and the transmission properties of the interface on the SH polarization of the silicon surface can be summarized as

$$P_i(2\omega) = T_{eff,ijk}L_{eff,ijk}\chi_{ijk}^{(2)}(2\omega)E_j(\omega)E_k(\omega), \tag{8}$$

where $L_{eff,ijk}$ contains the local field factors for both the electric fields at ω and at 2ω. $T_{eff,ijk}$ contains the changes in absorption and reflection at the surface at both ω and 2ω. $|L_{eff}|^2$ is often referred to as the enhancement factor.

Space charge regions (SCR) in semiconductors break the symmetry of the material with its built-in electric field (E^{dc}), thus giving rise to a SH signal. This mechanism is called the electric-field-induced-second-harmonic (EFISH) and the resonance from Silicon appears at ∼3.4 eV, the bulk E_1 resonance. The presence of built-in charges in thin films or in particles deposited on a Si/SiO_2 surface has been shown to create a SCR.[24,25] EFISH is fundamentally a third-order process, but the response can be described by a second-order susceptibility tensor $\chi_{eff}^{(2)}$, and the SH polarization is given as[26]

$$P_{Si,EFISH}(2\omega) = \chi_{Si,eff}^{(2)}(2\omega)E^2(\omega), \tag{9}$$

where $\chi_{Si,eff}^{(2)}(2\omega) = \chi_{Si}^{(3)}(2\omega)E^{dc}$, $\chi_{Si}^{(3)}$ being the third-order susceptibility tensor, and E^{dc} is the built-in electric field.

D. Linear effects

The linear optical response of metal particles has been investigated for many years, especially properties related to

localized plasmon resonances. The linear response gives some valuable insights to help interpret the SH spectra and provides us with both the depolarization factors and the absorption of the particles. In this work, we use the Island film theory approach[27,28] and the differential reflectivity spectroscopy[29] to investigate the linear properties. Here the metallic particles are included by adding a term to the Fresnell reflection coefficients which contains the surface susceptibilities γ and β. The particles are assumed to be oblate spheroids touching the substrate. The particles' major semi-axis (a) is parallel to the surface and the minor semi-axis (b) is perpendicular to the surface.

The modified Fresnel reflection and transmission coefficients are given as

$$r_p = \frac{\kappa_- - \xi_-}{\kappa_+ - \xi_+} \tag{10}$$

and

$$t_p = \frac{2n_a \cos\Theta\left(1 + \frac{1}{4}k^2\epsilon_a\beta\gamma\sin^2\Theta\right)}{\kappa_+ - \xi_+}, \tag{11}$$

where

$$\kappa_\pm = (n_s\cos\Theta_i \pm n_a\cos\Theta_t)\left[1 - \frac{1}{4}k^2\epsilon_a\gamma\beta\sin^2\Theta_t\right], \tag{12}$$

$$\xi_\pm = \imath\frac{2\pi}{\lambda}\left[\gamma\cos\Theta_i\cos\Theta_t \pm n_a^3 n_s\beta\sin^2\Theta_i\right], \tag{13}$$

and n_a and ϵ_a are the refractive index and dielectric function of the ambient, respectively. n_s is the refractive index of the substrate, and $k = 2\pi/\lambda$. Θ_i and Θ_t are the incidence and refracted angles. Via ρ, the number of nanoparticles per unit area; $\alpha_\parallel$ and $\alpha_\perp$, the parallel and perpendicular dipolar polarizabilities, respectively; the coefficients γ and β are given as

$$\gamma = \rho\alpha_\parallel \quad \text{and} \quad \beta = \rho\alpha_\perp/\epsilon_a^2. \tag{14}$$

In the dipole approximation, the polarizabilities of spheroidal particles can be expressed analytically as

$$\alpha_{\parallel,\perp} = \frac{4\pi a^2 b}{3}\frac{\epsilon_a(\epsilon_m - \epsilon_a)}{\left[\epsilon_a + M_{\perp,\parallel}(\epsilon_m - \epsilon_a)\right]}, \tag{15}$$

where ϵ_m is the dielectric function of the metal particles, and $M_\perp$ and $M_\parallel$ are the depolarization factors for the perpendicular and parallel direction. As the size of the metal particles is comparable to the bulk mean free path of the electrons (42 nm for Au), the metal dielectric function must be modified as

$$\epsilon_m(\omega) = \epsilon_B(\omega) + \frac{\omega_p^2}{\omega^2 + \imath\omega\tau_B^{-1}} - \frac{\omega_p^2}{\omega^2 + \imath\omega\tau^{-1}}, \tag{16}$$

where ϵ_B is the bulk dielectric constant, ω_p is the plasma frequency, τ_B is the relaxation time in the bulk metal, and $\tau^{-1} = \tau_B^{-1} + v_F R'^{-1}$ where v_F is the Fermi velocity and R' is some effective radius of the particle. Moreover, for the larger particles, it is necessary to consider the dynamic depolarization and renormalize the horizontal polarizability $\alpha_\parallel$ as[27,30]

$$\frac{1}{\alpha_\parallel^*} = \frac{1}{\alpha_\parallel} - \frac{k^2}{4\pi a} - \imath\frac{k^3}{6\pi}. \tag{17}$$

E. Modelling of SHG

Our model for the intensity of the measured SHG signal from the combined system of the Si/SiO_2 interface and the gold particles is a sum of SH polarizations

$$I(2\omega) \propto \left|\sum_{ijk} P_{ijk}^{Au} + \sum_n P_n^{Si}\right|^2. \tag{18}$$

Here P_{ijk}^{Au} are the gold polarizations described by Eq. (6) and P_n^{Si} are the Si/SiO_2 interface polarizations described by Eq. (8). The model contains many variables and without input from both scanning electron microscope (SEM) analysis and linear measurements, any analysis would be difficult. The list below gives an overview of the different parameters for both the linear and the SH models that are obtained.

1. Model of the linear spectra

From SEM analysis: Particle diameter, coverage, and density.

From literature: Refractive index of ambient and substrate. Dielectric function, plasma frequency, and the relaxation time of gold.

Free parameters: Particle height and R′ (effective radius).

2. Model of the SHG

From linear spectra: Depolarization factors. Modified dielectric constant. Absorption, transmission, and reflection.

Locked parameters: The position and width of all Si/SiO_2 resonances, except E_1.

Free parameters: The Rudnick and Stern parameters. The position and width of the E_1 resonance. The phase and $L_{eff,k}$ for all Si/SiO_2 resonances.

The EFISH contribution has not been included in the model since the EFISH signal and the E_1 interface signal are close and cannot be separated in the measurements. Instead both the position and the width of E_1 are free parameters, and the two contributions are treated as one in the model.

III. EXPERIMENTAL SETUP

The Silicon samples were cut from (111)-oriented wafers and mounted inside a UHV system with a base-pressure below 10^{-10} mbar. Two short heatings to 1000 °C removed the native oxide and the surface obtained showed a 7 × 7 reconstruction which was verified via the low energy electron diffraction. The sample was then exposed to 12001 O_2 (1 l is 10^{-6} Torr for 1 s) at a temperature of 600 °C to passivate and to seal the surface with a thin (∼1 nm) SiO_x layer.[31] The gold particles were deposited at a rate of 2 monolayers/min using an electron beam evaporator. During

the deposition, the sample was held at 500 °C. Our setup enabled us to move the sample into the shadow of a screen during deposition, thus controlling the size of the particles through the amount of metal deposited on the surface. Five different areas where made, starting with 10 monolayers on the first area and adding 10 monolayers for each area, up to 50 monolayers. Hereby five areas with different particle size distributions were produced on the same sample. The rate of material deposition and total material deposited were measured using a quartz crystal microbalance (QCM).

The SH spectra were obtained on the sample in UHV using a Continuum Surelite II-10 Nd:YAG pump laser in combination with a tunable Continuum Surelite optical parametric oscillator (OPO) system. The OPO emitted pulses of a duration of approximately 4 ns, and the photon energy was scanned from 0.9 eV to 2.42 eV. In order to minimize the risk of damaging the nanoparticles on the surface, the intensity of the laser was reduced by using a $\lambda/2$-wave plate in combination with a polarizing beamsplitter. A 300 mm focal length lens was used to focus the pump light onto the surface. In most cases, the sample was kept a few cm away from the tightest focus. The angle of incidence was 67° with the plane of incidence parallel to the (110) direction. The reflected SH signal was separated by low pass filters and passed through a polarizer before being detected by a photomultiplier tube connected to a boxcar averager. The signal was normalized using the SH front surface reflection from a quartz-crystal wedge.

After the SH measurements, the sample was removed from the UHV chamber directly to the linear measurements, which were performed with a Sentech SE 850 ellipsometer. The particle diameter and the number of particles per area were obtained using images taken with a Zeiss 1540 XB scanning electromicroscope (SEM) and subsequent analysis with imageJ.

IV. RESULTS

The results of the SEM analysis of the nanoparticles grown on area 2–4 are presented in Fig. 1. From this analysis, it can be seen that each area has a double size distribution, one with a diameter centered around ∼30 nm (marked 2 in Fig. 1 30 ML) and a larger diameter which varies for the specific areas (marked 1 in Fig. 1 30 ML). Table I lists the complete result of the analysis. In addition to the diameters, the SEM analysis also provided the density of particles and the coverage. Both the density and the coverage, included in Table I, are independent of the diameter and are related to the overall distribution.

The height of the particles was investigated using a focused ion beam (FIB) cutting into the sample together with SEM, but due to the small height of the particles, no reliable measurement could be obtained. However, it was evident that the particles were disk-shaped with a large diameter to height ratio and a height considerably smaller than calculated from the number of deposited ML divided by the coverage.

A. Linear reflection

Figure 2 shows the linear differential reflection measurements and the result of our modelling using the Island film approach. In the main figure, the incident light is p-polarized and only the p-component of the reflected light was detected, while the insert shows the measured s-component of the reflected light, with s-polarized incident light. We used the particle diameter and density from the SEM analysis and fitted the remaining unknown variables, namely, particle height and relaxation time. In Table I, the particle heights obtained from the model are shown. The intensity fluctuations of the light used in the differential reflection measurements are less than 0.2% for energies below 3.7 eV. The uncertainty is very low in the differential reflection, and we expect a higher uncertainty for the film thickness.

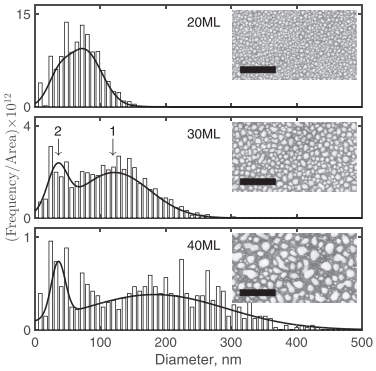

FIG. 1. Nanoparticle size distribution from areas with 20 ML, 30 ML, and 40 ML and the corresponding SEM image. The two arrows on 30 ML indicate the size two distributions. The scalebar inserted in the SEM images is 1 μm.

Four distinct features marked A-D in the figure can be identified in the linear spectra. A is related to the horizontal localized plasmon frequency of the nanoparticles; the position and the width of the resonance for each area is seen in Table I. The position of each resonance and the shift towards lower energy with size corresponds well with what one would expect from the larger particles on the sample.[32,33] The shoulder appearing around 2 eV (B), especially for the large particles, is also an effect of the horizontal localized

TABLE I. For each area on the sample, Table I lists the particle diameter, particle height, density, and gold coverage. Also listed are the position and width of resonance A. Diameter and height 1 and 2 refer to the two size distributions found to co-exist on the sample.

Monolayers		10	20	30	40	50
Diameter 1	nm	31	74	121	183	250
Diameter 2	nm	10	34	34	35	33
Density	m^{-2}	5.4×10^{14}	1.2×10^{14}	4.8×10^{13}	1.8×10^{13}	1.2×10^{13}
Coverage		0.23	0.33	0.36	0.33	0.36
Height 1	nm	1.65	3.85	6.0	7.8	9.0
Height 2	nm	1.25	3.29	5.6	7.8	8.7
Resonance A	eV	0.97	0.96	0.91	0.79	0.68
Width A	eV	0.40	0.38	0.38	0.4	0.5

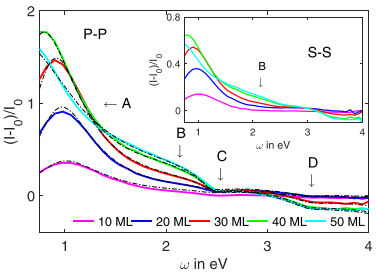

FIG. 2. The main figure is the linear differential reflection from area 1–5 for p-polarized light. The full coloured lines represent the measurements, and the dash-dot black lines are fits using the Island theory approach. The small inset is the reflection from area 1–5 for s-polarized light. The intensity fluctuations are less than 0.2% for energies below 3.7 eV.

plasmon as it is visible using both p- and s-polarized light. It must be associated to the horizontal plasmon of the small particles or to the quadrupolar mode of the large particles, but the two contributions are difficult to distinguish from each other. The feature at 2.5 eV marked C is related to the increased absorption due to the interband transitions in gold. Last, the negative 3.4 eV (D) feature coincides with the E_1 transition of the silicon substrate. The width of the horizontal plasmon resonance is large because of the very broad size distribution (see Fig. 1). This broadening is incorporated through the metal dielectric function as a larger relaxation time.

The particle height used in the model is of the order of 20% of that obtained from the amount of Au deposited when referring to the QCM (number of monolayer times z_{Au} divided by the coverage). There could be two reasons for this difference. First, the sticking coefficient of Au on Si is less than one. The sticking coefficient depends highly on materials, temperature of the substrate, and the amount of material deposited.[29,34,35] Secondly, sharp edges on the particles have the same effect on the surface plasmon resonances as lowering the particle height. Using the plasmon frequency to determine the height may thus result in too low values.

B. Second harmonic generation

The measured second-harmonic spectra (open circles) and the model (black lines) are shown in Fig. 3. All spectra were measured with a p-polarized pump-field and SH-field.

The subfigure labeled 0 ML is the SH spectrum from a clean Si/SiO_x interface. As expected there are two distinct features: the E_1 resonance around 3.3 eV and the E_2 resonance around 4.4 eV. The silicon-oxide resonance at 3.7 eV

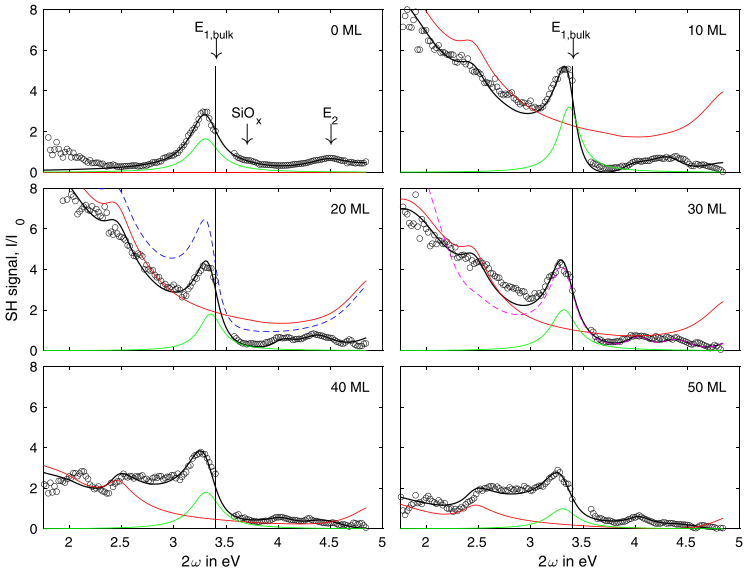

FIG. 3. Measured and modelled SH spectra for p to p polarization. "0 ML" is the SH spectrum from a clean SiO_x surface. 10 ML–50 ML are SH spectra from areas 1–5 with 10–50 monolayers of deposited gold. The open black markers are the SH signals from the measurements, and the black lines are the result of our modelling. The red lines represent the gold contribution to the SH signal, the green are the E_1 contribution. The blue dashed line in 20 ML is the model with substrate contributions above 3.4 eV removed. The magenta dashed line in 30 ML is the model with the $P_{\perp\parallel\parallel}$ contribution removed.

and the E_1' resonance at 5.3 eV are not pronounced but they are needed in the model to get a good fit. The clean silicon-oxide surface is modelled using Eq. (2).

Figure 3 10 ML to 50 ML show the measured SH spectra and models from areas 1–5, respectively. The effect of the added gold is clearly visible on all the measurements, mostly as a large increase in signal in the low energy part of the spectra. The E_1 resonance from the substrate can still be identified on all areas. The areas with gold particles are modelled as a sum of SH polarizabilities including the gold particle part and the field enhanced silicon part as described in Eq. (18). For the thin oxide used, the E_2 resonance and the oxide resonance around 3.7 eV are much weaker than the E_1 resonance. The influence of gold deposition on these two resonances is thus not considered in detail here. However, we include all three surface resonances (the oxide, the E_2, and the E'_1 transitions) in the figures since they contribute to the fits used to extract the field enhancements. The blue dashed line in Fig. 3 20 ML show the effect of removing these three contributions in the model. It is clear that they affect the SH spectra, even at a low energy. It is possible to adjust the remaining parameters to improve the fit, but the extracted enhancements become significantly different. However, a large number of variables is included in the complete model of the SH generation from a silicon-oxide surface with gold particles, which make both the modelling and interpretation very difficult. As described in Subsection II E, we used the SEM investigations and the linear measurements to obtain both the local field factors and the modified dielectric function of the gold particles, which simplifies the modelling of the SH generation from gold particles to the problem of finding the three Rudnick and Stern parameters of each polarization (see Eqs. (5), (6), and (7)). The gold contributions are shown as red lines in Fig. 3. The silicon and silicon-oxide part of the spectrum are modelled by adjusting the phase and $L_{eff,k}$ of each resonance of the interface, and also the frequency and the width of the E_1 resonance. The changes in transmission at both ω and 2ω are calculated using values obtained from the linear measurements. The E_1 contribution to the SH signal is shown in Fig. 3 as green lines. As is evident in Fig. 3, 10 ML to 50 ML, we were able to include all the major features of the SH spectra using this approach.

V. DISCUSSION

As demonstrated in both the linear and the SH spectra, the large horizontal Au plasmon resonance can easily be separated from the SH resonances of the substrate. The linear measurements (see Fig. 2) place the horizontal plasmon of the gold particles at ≈1 eV and lower for the increasing amount of deposited gold. As expected, we see a large second harmonic generation signal from the particles in this energy range, resulting in SH signal at twice the plasmon energy. With an energy of ≈1 eV and lower, the horizontal plasmon is just at the edge or outside the current spectral region. The shoulder named B in Fig. 2 will lead to the SH signal at higher energies, ≈4.0 eV. All the features from 2 eV to 3 eV in the SH spectra can be related via the modelling to cross coupling and the $a_{\perp\parallel\parallel}$ parameter. The main difference between SHG and differential reflection is the surface sensitivity. SHG is sensitive to a small fraction of a monolayer of gold, in particular, in the plasmon region. The sensitivity is considerably higher than for the differential reflection since SHG is a direct surface sensitive measurement of the deposition and not a difference between two separate measurements.

The Rudnick and Stern parameters used in the model are shown in Fig. 4. Rudnick and Stern introduced the $a_{\parallel\perp\parallel}$ and $a_{\perp\perp\perp}$ parameters to describe the parallel and vertical surface currents, respectively. In many cases, these two currents are sufficient to describe the observed signal.[20,23] With our sample geometry with disk-like gold particles on a silicon substrate (see Fig. 4(a)), this proved to be insufficient, in particular, concerning the feature around 2.4 eV. A calculation without the $P_{\perp\parallel\parallel}$ contribution as shown in Fig. 3 30 ML as the magenta dashed line. The contribution from $P_{\perp\parallel\parallel}$ is small as reflected in the absolute value of the $a_{\perp\parallel\parallel}$ parameter compared to both $a_{\parallel\perp\parallel}$ and $a_{\perp\perp\perp}$. In the pursuit of a better model, especially at a low energy, we found that an additional parameter in the vertical direction $a_{\perp\perp\parallel}$ improves the fits. This, however, is not pursued further as it is not in accordance with the symmetry of a plane surface. The value of $a_{\perp\perp\perp}$ has previously been investigated,[20,36,37] both theoretically and experimentally, and showed a strong dependence on the surface configuration. For Aluminium particles, the value ranged from almost 0 up to 37 depending on the surface configuration.[37] A strong dependence on the surface structure is also observed here for all the a parameters. The values found are within the expected range.

The E_1 resonance of the substrate can easily be identified on all the areas with deposited gold and through our model, we could extract several resonance properties. Figure 5 shows the resonance energy, enhancement, the phase, and width for the E_1 resonance. We see an immediate jump in the resonance position to a value of ≈3.4 eV after 10 monolayers of deposited gold. This strongly suggests that the deposited gold creates a SCR and an EFISH signal as explained in Subsection II C. As more gold is added, the resonance returns to the

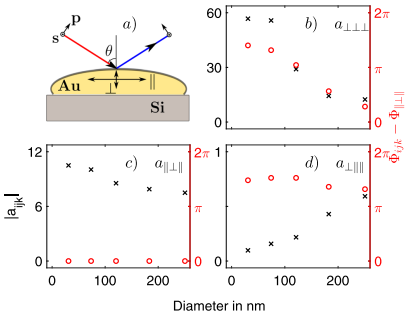

FIG. 4. (a) is a sketch of the sample geometry. (b)–(d) are the Rudnick and Stern parameters used in the model. Black marks represent the absolute value, and the red marks represent the phases relative to the phase of $a_{\parallel\perp\parallel}$.

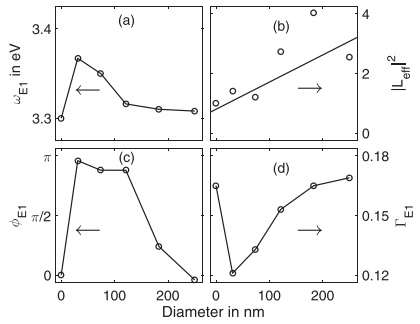

FIG. 5. (a) Position of the E_1 resonance as a function of the particle diameter. (b) enhancement of the E_1 resonance as a function of the particle diameter. (c) Phase of the E_1 resonance relative to that of the Au particles as a function of the particle diameter. (d) Width of the E_1 resonance as a function of the particle diameter.

interface value of 3.3 eV as can be seen via the green lines in Fig. 3 and in Fig. 5(a). For p to p polarization, it is not possible to separate the interface signal ($E_{1,if}$) and the EFISH signal ($E_{1,scr}$), and they are treated as one single resonance in our model. Fig. 5(d) show an immediate drop in the resonance width to a value of ≈0.12 after 10 monolayers of deposited gold. The decrease in width is explained by an interference between the $E_{1,if}$ and the EFISH contributions. The resonance width follows the same trend as the E_1 resonance position and returns to the interface value when more gold is added.

In the following, the shift in E_1 resonance position is discussed. Photoemission studies of Sn nanoparticles on an oxide covered silicon surface similar to the substrate in the present work show that when Sn is deposited on the oxide, electrons from the silicon substrate tunnel through the thin oxide to the metal particles.[38] The band bending following this charge transfer was found to increase with metallic surface area and total surface charge, levelling out at high coverage with 10 ML deposited. The results showed a band bending of 0.40 eV, which is close to the value of a clean Si(111) 7×7 surface, giving a space charge region depth of ≈730 nm. In our case, 10 ML is the minimum amount of Au deposited. The band bending saturates as the build up charges on the particles prevent more electrons to tunnel through the oxide layer, and larger particles do not lower this barrier.

The EFISH intensity depends on both the band bending and on the penetration depth of the pump and SH fields.[39] In the case that the penetration depth is much shorter than the depth of the space charge region, the EFISH intensity exhibits a linear dependence on the band bending. The penetration depth of light in Silicon is calculated[40] to be ≈15 μm, ≈25 nm, and ≈10 nm for 1.65 eV, 3.3 eV, and 3.4 eV photons, respectively. Thus, the EFISH contribution originates from the first few tens of nanometres in the Si substrate where the DC field from the space charge layer can be considered constant.

The field enhancement from the Au particles is expected to be located in an even shorter range, such that L(z) is limited to a few nanometers into the silicon substrate.[1,41] Field enhancement from the Au particles is thus expected to favor the interface contribution compared to the bulk-like EFISH part. The shift in E_1 resonance position can thus be understood in the following way. Deposition of the first 10 ML Au leads to charge transfer to the metal particles and thus an increasing DC field in the space charge region, resulting in a dominating EFISH contribution at the bulk E_1 resonance (3.4 eV). The band bending is expected to saturate around 10 ML and as more gold is deposited, the growing particles size leads to an increasing polarizability (see Eq. (15)), thus also increasing the field enhancement. As the short range field enhancement grows, the surface contribution at 3.3 eV grows to dominate the E_1 resonance. Variations in the phase of the E_1 resonance coming out of the modelling (see Fig. 5(c)) also support this interpretation. Samples with a positive space charge have a phase difference of $\approx\pi$ between the EFISH and the surface contributions.[17] Thus, the phase of the Si signal relative to that of the Au particles, change according to the type of resonance that dominates the signal.

In the following, we turn to the discussion of the field enhancement at the Si/oxide interface. First, it should be realized that the signal from this interface is seen through the deposited Au particles. Adding gold changes the transmission, reflection, and absorption properties of the surface. This can be seen in Fig. 6 which shows the transmittance for each area of the surface, including absorption in the gold particles. These are linear effects and are very well understood via Eqs. (10) and (11), and via the relation $1 = A + T + R$, where A is the absorption, T is the transmittance, and R is the reflectance. Less of the pump field is present at the interface, and a smaller part of the generated signal is transmitted back through the surface as gold is deposited. Focusing on SHG around 3.3 eV and comparing 50 ML coverage to the surface without Au, it is seen by considering $T(1.65\,eV)^2T(3.3\,eV)$ that the Si signal is expected to decrease by a factor of 5 due to the deposited Au. Thus, though the E_1 contribution to the measured SHG intensity represented by the green curve in Fig. 3 decreases

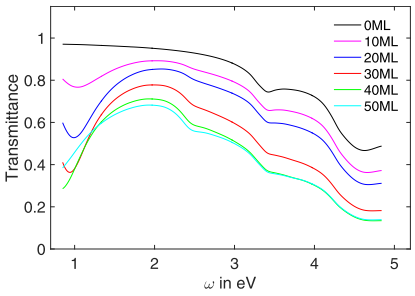

FIG. 6. Transmittance for p-polarized light at an incident angle 67° as a function of the photon energy. The Transmittance is calculated using results from the linear measurements and includes absorption in the gold particles.

with coverage, the nonlinear signal at the interface grows due to field enhancements.

The increasing strength of the field enhancement is evident through the enhancement factor $|L^2_{eff}|$ from our modelling (see Fig. 5(b)); the increase is moderate, especially compared to the other experiments with metallic particles as field enhancers.[2–4,9,10,12] There are a number of reasons for this difference. (1) In our case, the E_1 resonance is far from the plasmon resonance of the gold particles, and we would not expect a large enhancement. (2) We have a broad size distribution which means that the particles are resonant at different energies, resulting in a spectrally broad but also weaker field factor. As mentioned before, the $E_{1,if}$ and $E_{1,SCR}$ resonances are treated as one in our model, the very low enhancement at 20 ML could be explained by the transition from EFISH signal to interface signal. At the 50 ML area, the enhancement appears to fall off again, possibly an effect of depolarization of the quite large particles.

To further investigate the enhancement factor, we look at the field factors which can be calculated via Eq. (4). According to Wokaun,[9] the field factor for the metal particles at normal incidence can also be calculated as

$$|f^2(\lambda,d)| = \frac{\lambda n_s A(\omega,d)}{2\pi d \mathrm{Im}(\epsilon_m(\omega))T(\omega,d)}, \qquad (19)$$

where f is the parallel field-factor at wavelength λ and mass thickness d, n_s is the refractive index of the substrate, $A(\omega, d)$ and $T(\omega, d)$ are the absorption and transmittance of the island film, and $\epsilon_m(\omega)$ is the complex dielectric function of the metal. The absorption and transmittance at normal incidence can be calculated from linear measurements via Eqs. (10) and (11) and the relation $1 = A + T + R$. Also the mass thickness is obtained from the linear measurements as the particles' height times the coverage, in our case, for the 30 ML area, the mass thickness is roughly 22 Å (60 Å high particles covering 36% of the surface). The same factor can be calculated via Eq. (4) using the depolarization factor obtained from the linear measurements. These calculations are shown in Fig. 7 for the 30 ML area for both the Wokaun method (Eq. (19)) and the method described by Aktsipetrov (Eq. (4))

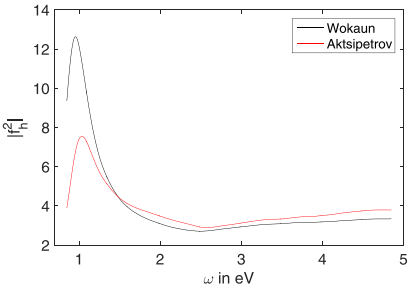

FIG. 7. Absolute square of the local field factor at a normal incident as a function of the photon energy. Black line is calculated via Eq. (19). The red line via Eq. (4).

The two methods agree on both the spectral shape and the magnitude, except at the low energy end of the spectrum where the magnitudes differ.

Wokaun[9] has calculated the f^2 for gold particles on a sapphire substrate. Though sapphire has a lower refractive index than Silicon, the strength of field factors should be comparable for the two substrates. They find a field factor of $\sim$3 at an energy of 2.33 eV and a mass thickness of $\sim$20 Å, which agrees well with our findings. The above considerations and calculations cannot be linked directly to our measurements which are performed at 67° and on a silicon substrate, but they support our method of finding the field factors.

It is also interesting to see how the gold SH signal, which dominates the spectra below 3 eV, compares with the calculated enhancement factor. Our SHG measurements are performed at an incident angle of 67°, so both horizontal and vertical field factors are at play. Our modelling showed a strong coupling between the horizontal and the vertical component which leads us to an estimation of the enhancement of the gold particles as

$$|L_{eff}|^2 = |(L_h(\omega) + L_v(\omega))^2 (L_h(2\omega) + L_v(2\omega))|^2, \qquad (20)$$

where $L_{h,v}$ are calculated via Eq. (4), and we use the island film theory to find the depolarization factor M for both the horizontal and the vertical component. Figure 8 shows the measured SH signal (black circles) together with the calculated enhancement factor (red solid line), both for the 50 ML area. The shape of $|L_{eff}|^2$ fits well with the low energy part of the measured SH spectra, which is a region where the Si/SiO_x interface has no resonance and mainly the gold contributes to the signal. The minimum at 2.3 eV can via the modelling be linked to $P_{\perp\parallel\parallel}$, thus it originates from a coupling between the parallel and the vertical plasmon. This minimum appears again at twice the energy, 4.6 eV.

The above considerations only relate to an enhancement of the signal from the gold particles while our main interest is in the enhancement of the SH silicon E_1 resonance. We will focus on the area with 50 ML of deposited gold as the EFISH contribution is very small, and the E_1 resonance seen in the measurement is primarily the interface signal. As this signal is generated in the first few atomic layers in the

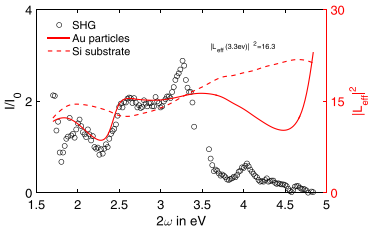

FIG. 8. The black circles are the measured SHG from the area with 50 ML of deposited gold. The red solid line is the field factor for the gold particles calculated via Eq. (20). The red dashed line is the field factor in the silicon substrate calculated via Eq. (21).

silicon, we are interested in the field in silicon. Due to the thin SiO_x layer, the particles are $\sim$1 nm from the substrate and further more, light at the $E_1(\omega)$ energy is refracted from an angle in air of 67° to an angle of 14° in silicon. The small angle means that the vertical component is greatly suppressed, and it is primarily the horizontal component that contributes to the generated signal, which also simplifies the problem as the horizontal component of electric field thus is continuous across the boundary. Neglecting the vertical field factor and leaving out the distance to the interface, the enhancement factor in silicon can be calculated as

$$|L_{eff}|^2 = |[\cos(\theta'(\omega))L_h(\omega)]^2 \cos(\theta'(2\omega))L_h(2\omega)|^2, \quad (21)$$

where $\theta'(\omega)$ and $\theta'(2\omega)$ are the light angle in Silicon at ω and 2ω, respectively. The red dashed line in Fig. 8 shows the enhancement factor as a function of 2ω for the 50 ML area using the expression above.

First we see that the low peak at $2\omega = 2$ eV is an effect of the horizontal plasmon, as it coincides with a peak in the enhancement factor. The minimum at 2.3 eV and at 4.6 eV of the solid red line in Fig. 8 disappears, which is expected as these are an effect of the coupling between the horizontal and the vertical plasmon. Also shown in the figure is the enhancement factor at $2\omega = 3.3$ eV, the $E_{1,if}$ resonance, which is calculated to be 16.3. This number should be compared to an enhancement factor of 3 found from our modelling (see Fig. 5). However, the range of the field enhancement from the metal particles has been left out. If we assume that the range is the same for both the fundamental and the SH field, that the particles are at a distance of 1 nm from the interface (approximate thickness of the SiO_x layer) where the SH is generated, and that only the decay length is responsible for this difference, one can calculate the decay length to be 3 nm. Jung *et al.*[41] showed that the range of the field factor is limited to a few nanometers in silicon. The decay length in air is generally assumed to be of the size of the particles. On the 50 ML area, the particles are on average 9 nm in height. Our estimated decay length of 3.3 nm is in the Si/SiO_x material, which as expected is shorter than the assumed decay length in air.

The high energy part of the SH spectrum is not treated in detail in this work, but a couple of features are worth mentioning. In the bulk silicon, there are two E_2 transitions:[13] one close to the X point at 4.27 eV, and one along the Σ direction at 4.51 eV. For the measured SH from the clean SiO_x surface, the E_2 resonance is close to 4.51 eV, whereas it appears that the 4.27 eV is promoted when the gold is deposited. With 40–50 ML of deposited gold, the E_2 signal is very weak and difficult to identify. When the gold is added, a new and distinct resonance appears around 4 eV. This resonance can be identified on all areas with gold, and its position does not change with the gold deposition or the particle size. We could not find any mentioning on this particular resonance in the literature. Both of the above features are not yet understood and are subject to further study.

VI. CONCLUSION

Field enhancements from Au particles with diameters in the range from 30 to 250 nm deposited on a Si substrate with a thin 1 nm thick surface oxide have been investigated by second harmonic generation spectroscopy.

Linear optical spectroscopy identifies a strong horizontal plasmon resonance near 1.0 eV and has been used to determine both the local field factors and optical properties, as well as absorption and transmission of the island film. The linear optical properties are well described by the Island film model and are used in the investigation of the SHG signal.

At energies below the E_1 critical point energy, a strong SHG signal originating from plasmon resonances in the Au particles is observed and well described by field enhancements from local field factors based on the linear measurements. By following the evolution of the characteristic SHG Si-resonance near the E_1 point, the field enhancement in the Si surface induced by the Au particles has been determined. It is found that the Au particles affect the SHG signal near the E_1 resonance both through charge transfer from the substrate to the metal and through enhancement of the field at the Si-oxide interface. Starting with the smaller particles, the charge transfer modifies the band bending in Si and thus gives rise to the EFISH signal, which dominates for smaller particles. The optical transmission is decreasing with larger particles, which in turn decreases the EFISH signal without affecting the near field. Thus for larger particles, the field enhancement at the Si-oxide interface dominates the SH signal.

When investigating the field enhancement in Si near the E_1 resonance, an enhancement factor L^2 of 3 is found experimentally for the largest islands. This is about a factor of 6 less than the corresponding factor calculated by the local field factors when the separation between Au islands and the Si interface region is neglected. It is argued that the fast decay of the local field away from the metal islands reduces the observed SHG signal and thus the resulting field enhancement.

ACKNOWLEDGMENTS

The authors gratefully acknowledge the financial support from the PLATOS project "Localized-surface plasmons and silicon thin-film solar cells," financed by the Villum Foundation.

[1]E. Hao and G. C. Schatz, "Electromagnetic fields around silver nanoparticles and dimers," J. Chem. Phys. **120**, 357–366 (2004).
[2]X.-M. Qian and S. M. Nie, "Single-molecule and single-nanoparticle sers: From fundamental mechanisms to biomedical applications," Chem. Soc. Rev. **37**, 912–920 (2008).
[3]P. L. Stiles, J. A. Dieringer, N. C. Shah, and R. P. Van Duyne, "Surface-enhanced Raman spectroscopy," Annu. Rev. Anal. Chem. **1**, 601–626 (2008).
[4]J. Kneipp, H. Kneipp, and K. Kneipp, "Sers-a single-molecule and nanoscale tool for bioanalytics," Chem. Soc. Rev. **37**, 1052–1060 (2008).
[5]S. Pillai and M. Green, "Plasmonics for photovoltaic applications," Sol. Energy Mater. Sol. Cells **94**, 1481–1486 (2010).
[6]H. A. Atwater and A. Polman, "Plasmonics for improved photovoltaic devices," Nat. Mater. **9**, 205–213 (2010).
[7]P. Spinelli, V. E. Ferry, J. van de Groep, M. van Lare, M. A. Verschuuren, R. E. I. Schropp, H. A. Atwater, and A. Polman, "Plasmonic light trapping in thin-film Si solar cells," J. Opt. **14**, 024002 (2012).
[8]R. A. Pala, J. White, E. Barnard, J. Liu, and M. L. Brongersma, "Design of plasmonic thin-film solar cells with broadband absorption enhancements," Adv. Mater. **21**, 3504–3509 (2009).

[9]A. Wokaun, J. G. Bergman, J. P. Heritage, A. M. Glass, P. F. Liao, and D. H. Olson, "Surface second-harmonic generation from metal island films and microlithographic structures," Phys. Rev. B **24**, 849–856 (1981).
[10]G. T. Boyd, T. Rasing, J. R. R. Leite, and Y. R. Shen, "Local-field enhancement on rough surfaces of metals, semimetals, and semiconductors with the use of optical second-harmonic generation," Phys. Rev. B **30**, 519–526 (1984).
[11]E. M. Kim, S. S. Elovikov, T. V. Murzina, A. A. Nikulin, O. A. Aktsipetrov, M. A. Bader, and G. Marowsky, "Surface-enhanced optical third-harmonic generation in AG island films," Phys. Rev. Lett. **95**, 227402 (2005).
[12]K. Tsuboi, S. Abe, S. Fukuba, M. Shimojo, M. Tanaka, K. Furuya, K. Fujita, and K. Kajikawa, "Second-harmonic spectroscopy of surface immobilized gold nanospheres above a gold surface supported by self-assembled monolayers," J. Chem. Phys. **125**, 174703 (2006).
[13]W. Daum, "Optical studies of Si/SiO_2 interfaces by second-harmonic generation spectroscopy of silicon interband transitions," Appl. Phys. A **87**, 451–460 (2007).
[14]J. Mejía, B. S. Mendoza, and K. Pedersen, "Second harmonic response of the si(111)7 $\times$ 7 surface," Surf. Sci. **605**, 941–946 (2011).
[15]G. Erley and W. Daum, "Silicon interband transitions observed at $si(100) - sio_2$ interfaces," Phys. Rev. B **58**, R1734–R1737 (1998).
[16]T. Suzuki, D. Milovzorov, S. Kogo, M. Tsukakoshi, and M. Aono, "Surface second-harmonic generation spectra of Si(111)-7×7 in the 1.0 1.7 eV fundamental photon energy," Appl. Phys. B **68**, 623–627 (1999).
[17]A. Rumpel, B. Manschwetus, G. Lilienkamp, H. Schmidt, and W. Daum, "Polarity of space charge fields in second-harmonic generation spectra of $Si(100)/Sio_2$ interfaces," Phys. Rev. B **74**, 081303 (2006).
[18]P. Liao, J. Bergman, D. Chemla, A. Wokaun, J. Melngailis, A. Hawryluk, and N. Economou, "Surface-enhanced Raman scattering from microlithographic silver particle surfaces," Chem. Phys. Lett. **82**, 355–359 (1981).
[19]J. E. Sipe, D. J. Moss, and H. M. van Driel, "Phenomenological theory of optical second- and third-harmonic generation from cubic centrosymmetric crystals," Phys. Rev. B **35**, 1129–1141 (1987).
[20]G. Bachelier, J. Butet, I. Russier-Antoine, C. Jonin, E. Benichou, and P.-F. Brevet, "Origin of optical second-harmonic generation in spherical gold nanoparticles: Local surface and nonlocal bulk contributions," Phys. Rev. B **82**, 235403 (2010).
[21]J. Rudnick and E. A. Stern, "Second-harmonic radiation from metal surfaces," Phys. Rev. B **4**, 4274–4290 (1971).
[22]J. E. Sipe, V. C. Y. So, M. Fukui, and G. I. Stegeman, "Analysis of second-harmonic generation at metal surfaces," Phys. Rev. B **21**, 4389–4402 (1980).
[23]F. X. Wang, F. J. Rodríguez, W. M. Albers, R. Ahorinta, J. E. Sipe, and M. Kauranen, "Surface and bulk contributions to the second-order nonlinear optical response of a gold film," Phys. Rev. B **80**, 233402 (2009).
[24]J. Rafaelsen, K. Pedersen, and Z. Li, "Size-effects in photoemission and optical second harmonic generation spectroscopy of Ge nano-dots on Si(111)," J. Appl. Phys. **114**, 044304 (2013).
[25]G. Dingemans, N. M. Terlinden, M. A. Verheijen, M. C. M. van de Sanden, and W. M. M. Kessels, "Controlling the fixed charge and passivation properties of $Si(100)/Al_2O_3$ interfaces using ultrathin SiO_2 interlayers synthesized by atomic layer deposition," J. Appl. Phys. **110**, 093715 (2011).
[26]J. I. Dadap, J. Shan, A. S. Weling, J. A. Misewich, A. Nahata, and T. F. Heinz, "Measurement of the vector character of electric fields by optical second-harmonic generation," Opt. Lett. **24**, 1059–1061 (1999).
[27]A. Mendoza-Galván, K. Järrendahl, A. Dmitriev, T. Pakizeh, M. Käll, and H. Arwin, "Optical response of supported gold nanodisks," Opt. Express **19**, 12093–12107 (2011).
[28]P. Bobbert and J. Vlieger, "The polarizability of a spheroidal particle on a substrate," Physica A **147**, 115–141 (1987).
[29]R. Lazzari, S. Roux, I. Simonsen, J. Jupille, D. Bedeaux, and J. Vlieger, "Multipolar plasmon resonances in supported silver particles: The case of Ag/α-$Al_2O_3(0001)$," Phys. Rev. B **65**, 235424 (2002).
[30]M. Meier and A. Wokaun, "Enhanced fields on large metal particles: Dynamic depolarization," Opt. Lett. **8**, 581–583 (1983).
[31]P. Morgen, A. Bahari, U. Robenhagen, J. F. Andersen, J.-K. Hansen, K. Pedersen, M. G. Rao, and Z. S. Li, "Roads to ultrathin silicon oxides," J. Vac. Sci. Technol. A **23**, 201–207 (2005).
[32]C. Langhammer, Z. Yuan, I. Zorić, and B. Kasemo, "Plasmonic properties of supported pt and pd nanostructures," Nano Lett. **6**, 833–838 (2006).
[33]C. Langhammer, B. Kasemo, and I. Zorić, "Absorption and scattering of light by Pt, Pd, Ag, and Au nanodisks: Absolute cross sections and branching ratios," J. Chem. Phys. **126**, 194702 (2007).
[34]L. Bachmann and J. J. Shin, "Measurement of the sticking coefficients of silver and gold in an ultrahigh vacuum," J. Appl. Phys. **37**, 242–246 (1966).
[35]D. G. Van Campen and J. Hrbek, "Silver on alumina: Adsorption and desorption study of model catalysts," J. Phys. Chem. **99**, 16389–16394 (1995).
[36]A. Liebsch, "Second-harmonic generation at simple metal surfaces," Phys. Rev. Lett. **61**, 1233–1236 (1988).
[37]C. W. Teplin and C. T. Rogers, "Experimental example of isotropic surface second-harmonic generation: dc-sputtered air-exposed aluminum thin films," Phys. Rev. B **65**, 245408 (2002).
[38]A. G. Silva, K. Pedersen, Z. S. Li, and P. Morgen, "Photoelectron spectroscopy as an *in situ* contact-less method for studies of {MOS} properties of ultrathin oxides on Si," Appl. Surf. Sci. **353**, 1208–1213 (2015).
[39]C. Ohlhoff, G. Lüpke, C. Meyer, and H. Kurz, "Static and high-frequency electric fields in silicon mos and ms structures probed by optical second-harmonic generation," Phys. Rev. B **55**, 4596–4606 (1997).
[40]G. Vuye, S. Fisson, V. N. Van, Y. Wang, J. Rivory, and F. Abelès, "Temperature dependence of the dielectric function of silicon using *in situ* spectroscopic ellipsometry," Thin Solid Films **233**, 166–170 (1993).
[41]J. Jung, T. Søndergaard, T. G. Pedersen, K. Pedersen, A. N. Larsen, and B. B. Nielsen, "Dyadic Green's functions of thin films: Applications within plasmonic solar cells," Phys. Rev. B **83**, 085419 (2011).

Paper B

Plasmon enhanced light scattering into semiconductors by a-periodic arrays of metal nanowires.

List of authors:

H. U. Ulriksen
T. Søndergaard
T. G. Pedersen
K. Pedersen

The paper has been published in the
optics express Vol. 27, pp. 14308-14320, 2019.

The layout has been revised.

Research Article | Vol. 27, No. 10 | 13 May 2019 | OPTICS EXPRESS 14308
Optics EXPRESS

Plasmon enhanced light scattering into semiconductors by aperiodic metal nanowire arrays

H. U. ULRIKSEN,* T. SØNDERGAARD, T. G. PEDERSEN, AND K. PEDERSEN

Department of Materials and Production, Aalborg university, Skjernvej 4, 9220 Aalborg East, Denmark
*huu@nano.aau.dk

Abstract: Light scattering from nanostructures is an essential ingredient in several optical technologies, and experimental verification of simulations of light scattering is important. In particular, solar cells may benefit from light-trapping due to scattering. However, light that is successfully trapped in an absorbing media such as e.g. Si necessarily escapes direct detection. We present in this paper a technique for direct measurement and analysis of light scattering from nanostructures on a surface, exemplified with aperiodic patterns of Ag strips placed on a GaAs substrate. By placing the structures on the flat face of a half-cylinder, the angular distribution of light scattered into the azimuth plane can be directly detected, including directions above the critical angle that would be captured if the substrate had the form of a slab. Modelling of the scattered light by summing up contributions from each strip agrees with the experimental results to a very detailed level, both for scattering backward and into the substrate.

1. Introduction

Metallic nanoparticles have been intensively studied due to the strong scattering at the particle plasmon frequency [1–3]. A special case is nanostructures on a surface which is of interest for applications such as optical nanoantennas [4] and light-trapping in thin-film solar cells [1,2]. High-refractive-index substrates are of particular interest since they have a large effect on the scattering properties. These applications rely not only on the strong scattering of nanostructures but also the ability to control the direction of the scattered light. The scattering and absorption cross-sections of plasmonic metal nanoparticles have previously been studied both theoretically [5–8] and experimentally [5, 9, 10], and the mechanisms governing these properties are well understood. For thin-film solar cells in particular, the angular distribution of light scattered on a nanostructure is important in order to trap as much light as possible. Hence, it is sought to maximize the fraction scattered into the substrate and to scatter the light into angles above the critical angle. The theoretical work in this area is extensive and covers a range of sample geometries, such as a scatterer above or on a surface [8, 11–13] and a scatterer in a sandwich structure [6, 14]. Experiments measuring the angular distribution of light have primarily focused on emission from a single scatterer using dark-field microscopy [15, 16] or special mirrors [17]. Other experiments measure the angular distribution of light scattered off an ensemble of nanoparticles [18], but here the single-particle angular distribution is lost and it is typically light scattered into air which is measured.

For analysis and optimization purposes it is important to verify the simulated properties of nanostructures. Such verification can be difficult, however, in the actual device geometry due to light-trapping and absorption. For instance, the absorption in silicon (Si) is sufficiently high to make it difficult to detect light scattered into the Si substrate, in particular with wavelengths of interest for solar cell applications, and to obtain sufficient signal-to-noise ratio, while maintaining the angular information. Hence, in this paper we present a practical and simple method to address

#360739 https://doi.org/10.1364/OE.27.014308
Journal © 2019 Received 21 Feb 2019; revised 9 Apr 2019; accepted 11 Apr 2019; published 2 May 2019

Optics EXPRESS

these issues. A simple experiment is constructed where the angular spectrum of light scattered into the semiconductor can be determined directly using an angle scanning setup [19]. This is achieved by placing the structures on the flat side of a half-cylinder, near the center axis of the cylinder. The scattering angles into the cylinder material can be determined by detecting the angular spectrum transmitted through the cylindrical surface. As Gallium arsenide (GaAs) has almost the same refractive index as Si just below the Si bandgap, but very low absorption, the experiments are performed using a GaAs half-cylinder and a laser diode with a wavelength of 980 nm. This allows us to directly observe the scattering angles as well as the scattering cross-section of the structures. Hence, we demonstrate that the proposed method is a useful and accurate tool for verification of simulated angular scattering profiles of relevance for e.g. plasmon-enhanced solar cells.

2. Theory

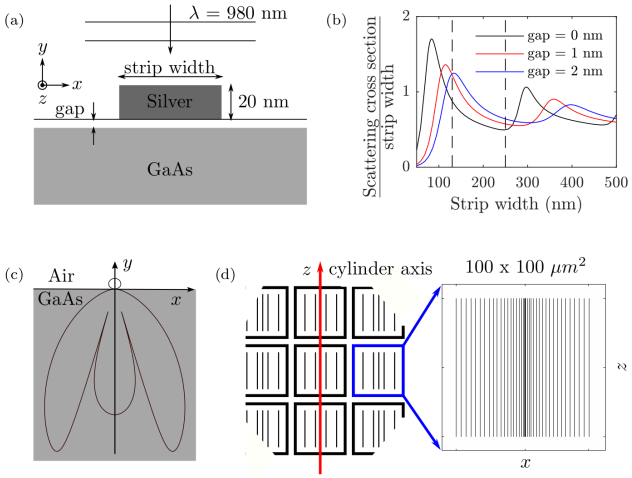

Fig. 1. (a) Sample geometries for a single strip. (b) Scattering cross section as a function of strip width for 3 different gap sizes. The dashed lines represent the strip width on the two samples that have been fabricated. (c) Scattering per unit angle into both air and substrate for a 130 nm strip. (d) Schematic illustration of the structure written on the flat side of the half-cylinder.

2.1. A single strip

The scattering of light by a large number of Ag nanostrips on a GaAs surface will, in this paper, be modelled by superposing scattered fields originating from each nanostrip. At normal incidence and in-plane polarization perpendicular to the strips there is very little scattering in the x-direction (see Fig. 1(a)), except for the generated near-field. The combination of a thick substrate, a relatively large distance between strips, and the aperiodic structure, allows us to neglegt multiple scattering between nanostrips, inter-strip coupling [20, 21] and surface-modes.

Received 21 Feb 2019; revised 9 Apr 2019; accepted 11 Apr 2019; published 2 May 2019

Optics EXPRESS

The total scattered field is thus obtained as the scattered field from a single nanostrip multiplied by a factor that takes into account the different propagation distances from each nanostrip before the light reaches the detector.

The scattering by a single Ag nanostrip on a GaAs surface being illuminated by a normally incident plane wave (see Fig. 1(a)) has been calculated by using the Green′s function surface integral equation method (GFSIEM) [22] for 2D scattering problems. The nanostrip is assumed to be of infinite length (along the z-axis), and the electric field is polarized along the x-axis. The corners of the nanostrip are rounded with a 2-nm corner radius. The thickness of the nanostrip is 20 nm, and the wavelength is 980 nm. According to the literature [23, 24] a native oxide layer on the GaAs is estimated to be from 0.5 nm to app. 2 nm depending on oxidation time. We take into account the effect of this layer by adding a small air-gap between the strip and the GaAs surface. The scattering cross section, i.e., the total scattered power normalized to the incident power per unit area, is shown in Fig. 1(b) as a function of strip width. By normalizing the scattering cross section with the strip width resonances can be easily identified. The resonances are due to the excitation of surface plasmon polaritons propagating back and forth across the Ag strips (along x) and being reflected at the strip edges. This leads to standing-wave resonances when the total round-trip propagation and reflection phase is an integer multiple of 2π. The peaks in Fig. 1(b) are due to excitation of the 1st and 3rd order standing-wave resonances. The 2nd order resonance cannot be excited when using normally incident light due to symmetry considerations [22]. By assuming an oxide layer thickness of 1-2 nm a peak is found at the strip width of app. 130 nm, while a strip width of 250 nm being also considered in the paper is mid between resonances. The scattered radiation pattern (or differential scattering cross section) for a 130-nm-wide strip is shown in Fig. 1(c). Most of the scattered light goes into the semiconductor substrate, which is a consequence of the large refractive index of GaAs compared with air [22]. In addition, a large fraction of the scattered light is at angles that are above the critical angle of a GaAs-air interface ($\approx 17^\circ$ at 980 nm). A plane wave being incident on a planar GaAs-air interface, i.e., from the GaAs side at an angle above the critical angle, would be totally internally reflected. In the case of a GaAs film this means that the light would be trapped in the GaAs, which is useful for a solar cell. The radiation pattern is almost the same as the one for a 30-nm-wide and 17-nm thick strip (see [22]), which is because in both cases the strip width is significantly smaller than the wavelength, and the radiation pattern is similar to that of a dipole in both cases.

2.2. Array of strips – reflection

To obtain a large signal-to-noise ratio of the measured scattered light, one strip is not enough. Introducing more strips with equidistant spacing gives rise to sharp diffraction peaks, which, in connection with the experiment, is undesirable as all information of the scattering profile for a single strip is lost. To circumvent this we place the Ag strips in an aperiodic array to diffract the light into a broad range of angles and thereby obtain information on the scattering profile. To model the measured radiation pattern from the multiple strips we divide the model into two cases: backscattered light and light scattered into the substrate. In each case we assume the structures to be invariant along the z-axis.

For the backscattered case the model is straight forward. The detector is moved around the half-cylinder at angles up to $\theta = 90^\circ$ as illustrated in Fig. 2(a). At large distances from the strip the scattered field will propagate roughly as a cylindrical wave and for each detector angle (θ), see Fig. 2(b), the electric field at detector angle θ is calculated as

$$E(\theta) = F \sum_p \frac{S(\alpha_p) \exp(-ik_0 r_p) \exp\left(\frac{-(x_p - x_c)^2}{w^2}\right)}{r_p}. \quad (1)$$

Here, F is a scaling factor, $S(\alpha_p)$ is the square root of the single-strip radiation pattern (Fig. 1(c))

Received 21 Feb 2019; revised 9 Apr 2019; accepted 11 Apr 2019; published 2 May 2019

Optics EXPRESS

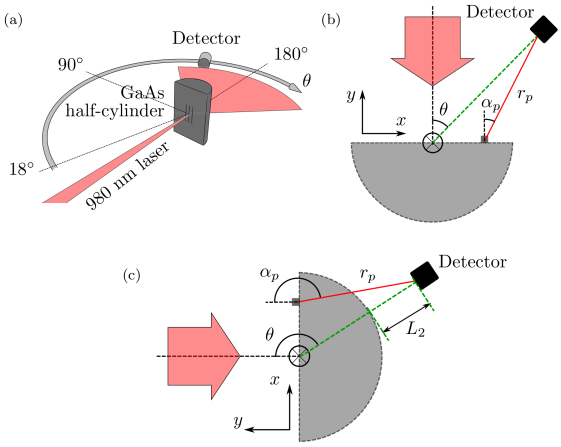

Fig. 2. (a) Detector setup. (b) Sketch showing angles and distances used in the model for reflection. (c) Sketch showing angles and distances used in the simple model for transmission.

at angle α_p (see Fig. 2(b)), k_0 is the free-space wave-number, and r_p is the distance from strip number p to the detector, also, x_p is the strip position on the surface for strip p, x_c is the position of the center axis of the incident beam relative to the center of the write-field, and w is the width of the incident Gaussian beam on the surface.

2.3. Array of strips – transmission

For light scattered into the substrate the problem is more complex for two reasons mainly. First, the distance traveled by light from the individual strip to the detector varies a great deal due to refraction and the curved backside. Second, the scattering intensity depends highly on the angle, as seen in Fig. 1(c).

One could question the need to include the effects mentioned above for the forward scattering and attempt a simpler approach much like Eq. (1). In such a simple model we assume that light from each strip also travels to the sensor in a straight line, neglecting the curved backside and the refraction of light as illustrated in Fig. 2(c). Again, the detector rotates around the fixed axis, now at angles above $\theta = 90°$. The distance from strip to sensor, r_p, is easily calculated, and if L_2 (see Fig. 2(c)) is assumed the same for every strip, the distance travelled in GaAs follows directly. The electric field at the detector angle θ is then calculated as

$$E(\theta) = TF \sum_p \frac{S(\alpha_p)\exp(-ik_0 n_1 L_{1,p})\exp(-ik_0 L_2)\exp\left(\frac{-(x_p-x_c)^2}{w^2}\right)}{r_p}. \quad (2)$$

T is the transmission coefficient of the GaAs to air interface, n_1 is the complex refractive index of GaAs, and $L_{1,p} = r_p - L_2$ is the distance traveled in GaAs. As will be apparent in Sec. 4.4 this model does not describe the measured signal and the effect of the curved backside must be considered.

Received 21 Feb 2019; revised 9 Apr 2019; accepted 11 Apr 2019; published 2 May 2019

Optics EXPRESS

The issues arising from the curved backside are illustrated in Fig. 3. If a strip is placed at the center of rotation, the distance travelled in the substrate is the same as the half-cylinder radius (R), the distance travelled in air is $L_2 = L - R$, and the detector angle θ is the same as the angle of the scattered light detected. For strips placed off center all three are changed into θ', L_1' and L_2'. Due to the relatively small radius of the cylinder and the high refractive index of GaAs, all three effects are significant and cannot be neglected.

To correct for these effects we introduce the two parameters δ and α', both illustrated in Fig. 3. δ is the change in the optical path length in air and α' is the change in angle, relative to the detector angle, of the scattered light reaching the detector. Moreover, we found it necessary to introduce a fitting-parameter (y' in Fig. 3) to account for a mismatch in rotational axis and surface. The angles in Fig. 3 are greatly exaggerated and are in the experiment very small, thus,

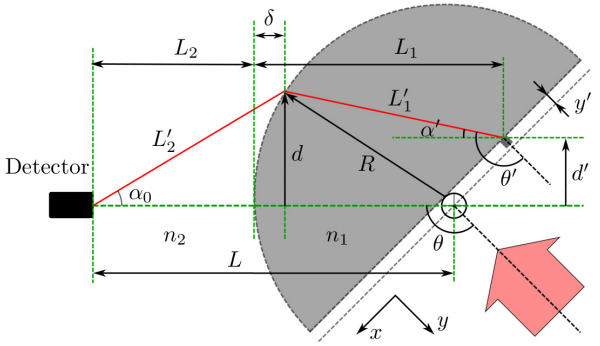

Fig. 3. Sketch of sample and detector system. The sketch is not to scale, $L = 0.30$ m and $R = 2.7$ mm.

both δ and α' can be estimated via the matrix method in paraxial optics;

$$\begin{bmatrix} d_0 \\ \alpha_0 \end{bmatrix} = \begin{bmatrix} 1 & L_2 \\ 0 & 1 \end{bmatrix} \begin{bmatrix} 1 & 0 \\ \frac{n_1 - n_2}{R n_2} & \frac{n_1}{n_2} \end{bmatrix} \begin{bmatrix} 1 & L_1 \\ 0 & 1 \end{bmatrix} \begin{bmatrix} d' \\ \alpha' \end{bmatrix}. \tag{3}$$

We define the optical axis as the straight line between the rotational axis and the detector. d_0 is the height above the optical axis of the light-beam at the detector and is always zero as the detector per definition is on the optical axis. α_0 is the angle of the light-beam at the detector. d' is the strip height above the optical axis and can for each strip be calculated as $d' = y'\cos(\theta) + x'\sin(\theta)$, where x' is the position of the strip on the surface, and y' is the surface offset (see Fig. 3). We calculate $L_1 = R - y'\sin(\theta) + x'\cos(\theta)$ and $L_2 = L - R$, where L is the distance from center of rotation to the detector and R is the radius of the half-cylinder. n_1 and $n_2 = 1$ are the refractive indices of the substrate and air, respectively. By solving Eq. (3) one obtains both α_0 and α'. To calculate δ we estimate $d = L_2\tan(\alpha_0)$ and then $\delta = R - \sqrt{R^2 - d^2}$. The corrected distance for each strip in both substrate and air is then

$$\begin{aligned} L_1' &= (L_1 - \delta)/\cos(\alpha') \\ L_2' &= (L_2 + \delta)/\cos(\alpha_0). \end{aligned} \tag{4}$$

Finally, the laser beam has a Gaussian beam profile with a width w, thus each strip is not illuminated equally. We end up with an expression for the total electric field at each detector

Received 21 Feb 2019; revised 9 Apr 2019; accepted 11 Apr 2019; published 2 May 2019

Optics EXPRESS

position as

$$E(\theta) = TF \sum_p \frac{S(\theta'_p)\exp(-ik_0 n_1 L'_{1,p})\exp(-ik_0 L'_{2,p})\exp\left(\frac{-(x'_p - x_c)^2}{w^2}\right)}{L'_{1,p} + L'_{2,p}}. \quad (5)$$

T is the transmission coefficient of the GaAs to air interface, F is a scaling factor, $S(\theta'_p)$ is the square root of the scattering intensity per unit angle in direction $\theta'_p = \theta + \alpha'_p$. x'_p is the strip position on the surface for strip p. Finally a simple moving average is applied to model the width of the detector.

The sample is mounted on a 5-axis stage when the structures are written using e-beam lithography. This gives an uncertainty on the positions of the write-fields relative to each other. This write-field stitching error must be accounted for in the model, but will result in a large number of variables if the position of all illuminated write-fields should be free to move. In order to limit the number of free variables in the models, we assume z invariance and that only three write-fields are illuminated. This is reasonable as the full width half maximum (FWHM) of the laser beam is 160 μm. This limits the free variables of the back scatter model to two write-field stitching, one beam-center and a scaling factor. For the forward scatter model we reuse the former values and need only one free parameter, the GaAs surface offset. The GaAs half-cylinder was grinded and polished by hand and imperfections in the shape of the half-cylinder are expected. As a consequence, prior to the experiment, a calibration of the half-cylinder was performed by a number of different diffraction gratings written on the half-cylinder. The gratings were made using e-beam lithography. The measured diffraction angles for each grating were then compared to the theoretical value to make a calibration curve. As a final remark, this method is not limited to any particular ordering of the strips or specific polarization of light. However, the array must be aperiodic with sufficient gap between strips. Within this limitation the proposed method can be applied to general scattering geometries and any polarization of the incidence light.

2.4. Summary of model

The list below gives an overview of how the different parameters for the models are obtained.

General assumptions:

Three write-fields, z invariance and cylindrical waves.

Measured quantities:

Width of the beam, distance from the cylinder axis to the detector, radius of the half-cylinder, calibration of the half-cylinder.

Model of the backscattered light

Free parameters: Write-field stitching error, beam-center position and scaling factor.

Model of the forward scattered light

From backscattering model: Write-field stitching error, beam-center position and scaling factor.

From literature: Refractive index of substrate.

Free parameters: The GaAs surface offset.

Received 21 Feb 2019; revised 9 Apr 2019; accepted 11 Apr 2019; published 2 May 2019

Optics EXPRESS

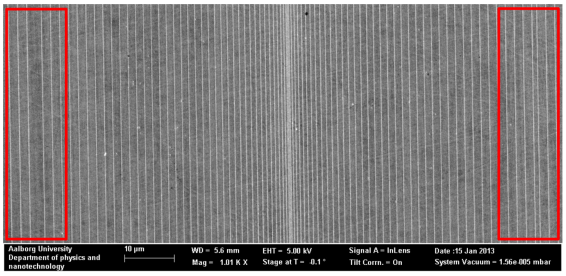

Fig. 4. SEM image showing the full width of a 100 x 100 μm^2 write-field with 130 nm Ag strips. Write-field stitching errors are seen in the red squares.

3. Experimental

The experimental setup is shown in Fig. 2(a). Laser light with a wavelength of 980 nm from a continuous laser-diode is focused with a 200 mm focal length lens onto the flat side of the half cylinder at normal incidence. The FWHM of the beam at focus has been measured to 160 μm. We use a Si detector mounted on an arm with a length of L = 0.30 m that can be rotated around the half-cylinder and all intensities are obtained from a single measurement. The half cylinder used in the experiment has a radius of R = 2.7 mm and is made of crystalline GaAs. The Ag strips are made by a standard e-beam lithography and lift-off procedure and are placed near the center on the flat side of the half-cylinder, with all strips parallel to the cylinder axis.

Specifically, two different samples have been fabricated, one with strips of 130 nm width and one with 250 nm width, all with a thickness of 20 nm. The width of 130 nm is chosen as it is expected to be at a plasmon resonance, whereas 250 nm is between two resonances, and a weak plasmon effect is expected, see Fig. 1(b). The e-beam-setup has a writing area of 100 x 100 μm^2, so both the 130 nm area and the 250 nm area are made of several identical write-fields written close together (see Fig. 1(d)).

The strips must be placed in an aperiodic manner and the exact position of each strip must be known. This is possible using e-beam lithography and for this experiment we have chosen the following position for each strip on a write-field of 100 x 100 μm^2

$$x_p = \pm 50\mu m \left(\frac{p}{p_{max}}\right)^{1.4}, p = 1, 2, 3, ..., p_{max} \tag{6}$$

where x_p is the position of strip p and p_{max} is the number of strips in one half of the write-field. The number of strips is determined by the required coverage

Both the 130 nm area and 250 nm area are designed to have a strip coverage of 10%, which leads to 77 strips and 40 strips on a 100 x 100 μm^2 area, respectively. For the 130 nm sample the range of periods spans from 0.24 μm to 1.83 μm . A SEM image of a part of a 100 x 100 μm^2 write-field with 130 nm strips is shown in Fig. 4. Also indicated in the red squares on Fig. 4 are write-field stitching errors, which can lead to both an increase and a decrease in the distance between the outer strips of two neighboring write-fields.

Received 21 Feb 2019; revised 9 Apr 2019; accepted 11 Apr 2019; published 2 May 2019

Optics EXPRESS

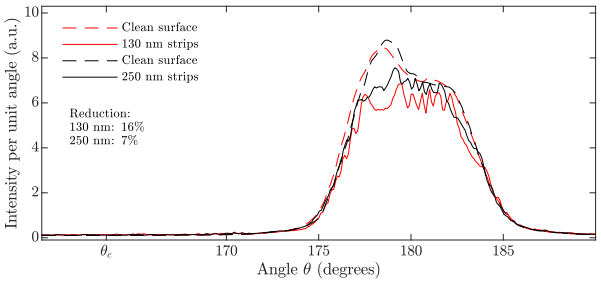

Fig. 5. Measured intensity of the transmitted light for the setup illustrated in Fig. 2(a). The incidence light is polarized transverse to the strips and results are shown for the aperiodic array of 130 nm and 250 nm Ag strips and the same areas without strips.

4. Results

4.1. Direct transmission

The level of interaction between light and nanostructures, both in terms of scattering and absorption, is an important property to investigate. Figure 5 shows the intensity of the directly transmitted beam. The polarization of the incidence light is transverse to the strips and results are shown both for the 130 nm and the 250 nm strips and for the same areas with no strips. The asymmetry in the directly transmitted beam, especially for the clean surface, is related to the beam quality of the laser diode used in the experiment. The reductions indicated in Fig. 5 represent the difference in directly transmitted light, with and without strips. It is calculated by comparing the integrated intensity per unit angle between the critical angles (from 163° to 197°) for the same area, with and without strips. Thus, the reductions represent the light that is lost via absorption, reflection and scattering into angles larger than the critical angle due to the Ag strips. For the 130 nm wide strips (see Fig. 5) we see a larger decrease in transmitted light compared to the case of 250 nm strips, i.e, ≈ 16% and ≈ 7%. This corresponds well with the expected resonance for the 130 nm strip (see Fig. 1(b)). The difference in magnitude of scattering out of the direct beam is also evident in Fig. 1(b), where the cross section per strip width on resonance is twice as large as off resonance. This comparison is posible as both areas have a 10 % strip coverage. The measured reduction contains both reflection, absorption and scattering, but at this structure size, scattering is the dominating effect [6, 9].

4.2. Scattered light – reproducibility

We now turn our attention to the diffracted light, starting with the total scattered light and means of tracking changes in the properties of nanostructures. Figure 6 shows the intensity of the light scattered off the aperiodic array of 130 nm Ag strips on the GaAs surface and is defined as $I_s = I - I_0$ where I is the measured intensity with strips and I_0 is the measured intensity without strips. The black line is the intensity from a new sample, whereas the red line is the intensity from the same sample, but 80 days older. The scattered intensity for the 80 days old sample has been multiplied by a factor of 8. Angles from 0° to 90° are backscattered light and from 90° to 180° is light scattered into the substrate and transmitted through the half-cylinder. The 90° to 180° intensity has been corrected for transmission and reflection losses. The green line is the calculated scattering per unit angle for a single strip and is equivalent to the one shown in Fig. 1(c). First, the ratio of backward to forward scattered light can be directly assessed and

Received 21 Feb 2019; revised 9 Apr 2019; accepted 11 Apr 2019; published 2 May 2019

Optics EXPRESS

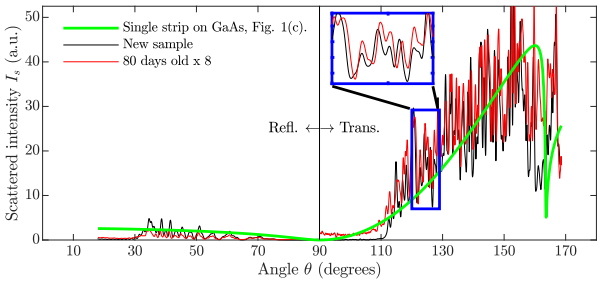

Fig. 6. Measured scattered intensity of the diffracted light from the aperiodic array of 130 nm Ag strips. The green line shows scattering per unit angle for a single 130 nm Ag strip on a GaAs surface. The black line is the measured signal for a new sample, while the red line is for an 80 days old sample multiplied by a factor of 8. The transmitted intensity has been corrected for transmission and reflection losses.

compared with the calculated profile(see Fig. 1(c)). Second, we see that our measurements for the new and 80-day old sample show the same complex peak pattern and intensity distribution except for a scaling factor where the intensity is much lower for the old sample. Exposure to the atmosphere is known to affect Ag nanostructures and both reduce plasmon effects and shift resonances [25, 26] which, in this case, results in a large decrease in scattering cross-section and thereby the scattered intensity. The interference between light scattered from the individual strips is clearly visible as a large number of peaks forming a complex pattern. As illustrated, this pattern is largely unaffected by the oxide layer, and the position of the peaks is reproducible. Thus this method is a strong tool for tracking changes in the properties of the nanostructures.

4.3. Backscattered light

We now discuss the details of the diffraction pattern. First, we consider the backscattered light. The red line in Fig. 7(a) shows the measured intensity of the backscattered light from the aperiodic array of 130 nm Ag strips. The black line in Fig. 7(a) is the calculated backscattered light using Eq. (1) and the green line shows the scattering per unit angle from a single 130 nm Ag strip on a GaAs surface. We have restricted ourself to three write-fields in the model, which are perfectly placed next to each other with no write-field stitching error (Fig. 4). The strips are infinitely long and the beam is perfectly centered on the middle write-field. Both the measured signal and the calculated spectra (F in Eq. (1)) have been scaled to a maximum intensity of one. With these initial parameters our model shows some resemblance with the measured signal. Both the strong onset of signal around 30 degree, which is caused by diffraction from the long period part (1.83 μm) of the aperiodic array, and large scale features at high angle are modeled with some success.

To improve our model we include the write-field stitching error and the position of the beam center axis by allowing the two outer fields and the beam (x_c) to move, still using Eq. (1). Optimizing the position of the write-fields and the beam in the model resulted in the calculated graphs in Fig. 7(b), again, both the measured signal and the calculated spectra have been scaled to a maximum intensity of one. We obtained the best result with the following movements: left write-field shift 0, right write-field shift 0.9 μm, and $x_c = 7$ μm. The write-field shifts are within the accuracy of 1-2 μm for the stage in the e-beam lithography setup. The center of the half-cylinder surface can be found with comparable precision, and a x_c value of 7 μm is

Received 21 Feb 2019; revised 9 Apr 2019; accepted 11 Apr 2019; published 2 May 2019

Optics EXPRESS

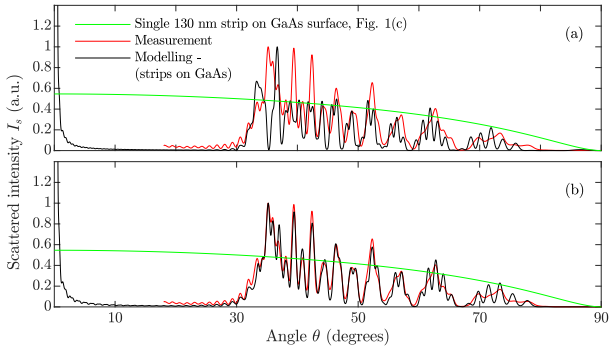

Fig. 7. In both (a) and (b), the green lines shows the scattering per unit angle from a single 130 nm Ag strip on a GaAs surface. The red line is the measured signal from the aperiodic array of 130 nm Ag strip and the black lines are the calculated signals using Eq. (1). In (b) the positions of the write-fields and the beam center have been optimized to match modelling and measurements.

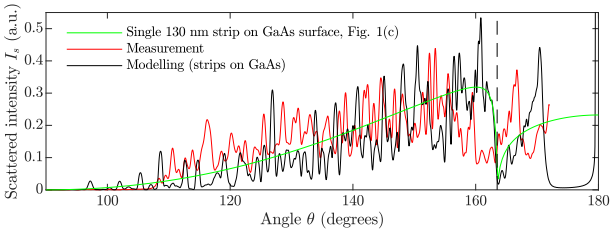

Fig. 8. The green line shows the scattering per unit angle from a single130 nm Ag strip on a GaAs surface. The red line is the measured signal from the aperiodic array of 130 nm Ag strips and the black line is the calculated signal using Eq. (2). The model is corrected for transmission and reflection losses. In the model we have used the write-field stitching error, beam axis position and scaling factor obtained from the modelling of the backscattered light. The dashed vertical line at $\approx 163^\circ$ represents the critical angle for the GaAs-air interface.

within the expected range when also considering imperfections in the shape of the half-cylinder. This has a large impact on the model for the backscattered light, which is now very close to the measured signal. Both the peak positions and the intensity of each peak fit well with the measured ones. The small differences probably originate from the fact that we only use three write-fields and neglect write-fields above and below these three which also contribute to the signal.

4.4. *Forward scattering*

First, we compare the result of modelling using Eq. (2) with the measured signal for the aperiodic array of 130 nm Ag strips. The result is presented in Fig. 8, where the black line is the model, the red line is the measured signal and the green line is the scattering per unit angle for the

Received 21 Feb 2019; revised 9 Apr 2019; accepted 11 Apr 2019; published 2 May 2019

Optics EXPRESS

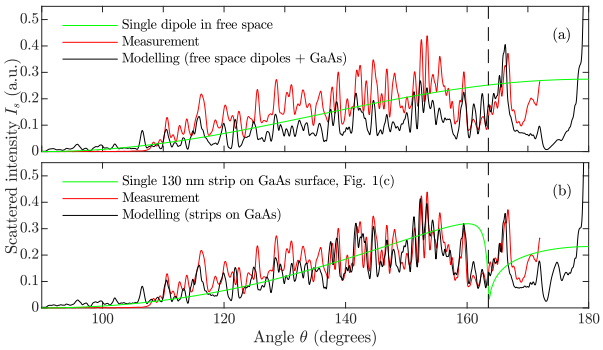

Fig. 9. In both (a) and (b), the green lines shows the scattering per unit angle from a single strip on which the respective models in (a) and (b) are based. The red line is the measured signal from the the aperiodic array of 130 nm Ag strips and the black lines are the calculated signals using Eq. (5) based on (a) free space dipole scattering and (b) the radiation pattern from a 130 nm wide Ag strip on a GaAs surface (see Fig. 1(c)). The models are corrected for transmission and reflection losses. In both models we have used the write-field stitching error, beam axis position and scaling factor obtained from the modelling of the backscattered light. The dashed vertical line at $\approx 163^\circ$ represents the critical angle for the GaAs-air interface.

single 130 nm Ag strip on GaAs. The critical angle for a GaAs-air interface is represented by the vertical dashed line. The model is corrected for transmission and reflection losses and, finally, we have used the write-field stitching error, beam axis position and scaling factor obtained from the backscattering model. The modelling is based on a GaAs refractive index of $n = 3.52 + i0.000083$ at a wavelength of 980 nm, as obtained from interpolating Sopra SA data [27]. The result clearly shows the need for a more detailed model for the forward scattered light. Despite the information obtained from the backscattering, the simple model only agrees on the overall intensity of the forward scattered light.

In Fig. 9 the results using the detailed model (Eq. (5)) are presented. The figure contains two separate graphs, each with the measured signal from the aperiodic array of 130 nm Ag strips in red, the modelling in black, the scattering per unit angle for a single 130 nm Ag strip in green and a vertical black line representing the critical angle. In Figs. 9(a) and 9(b) the models are the same but are based in 9(a) on $S(\alpha_p)$ for a dipole in free space and in 9(b) on $S(\alpha_p)$ for the 130 nm Ag strip on a GaAs surface (Fig. 1(c)). Like the previous simple model, the calculations are corrected for transmission and reflection losses. The results have been obtain using the write-field stitching error, beam axis position and scaling factor obtained from the backscattering model, and by optimizing the surface offset (y'). We obtained the best result with a surface offset of $y' = 210\ \mu$m, which is reasonable considering the experimental setup where the rotational axis of the detector and the center axis of the half-cylinder are aligned using the sample-stage with no direct indication of overlap. The results are very convincing when using the radiation pattern in Fig. 1(c), with good agreement between theory and experiment. For the model using free-space dipole scattering, the peak pattern is equally well described, but some deviations with respect to the intensity level appear. The peak pattern is fixed by the strips positions on the substrate whereas the intensity is related to both the strips position and the scattering per unit angle used in

Received 21 Feb 2019; revised 9 Apr 2019; accepted 11 Apr 2019; published 2 May 2019

the model.

5. Conclusion

A technique has been presented for verification of simulated light-scattering from surface nanostructures, with particular focus on verification of the angular scattering profile of a single scatterer. The technique is based on using multiple scatterers placed in an aperiodic array for increasing the signal-to-noise ratio, and at the same time maintaining angular information of the light-scattering from a single scatterer. By placing the scatterers on the flat face of a half-cylinder, the light scattered into the surface is coupled out through the curved sides of the cylinder, such that the angular profile of light scattered into the substrate can be measured. A thick substrate in combination with the aperiodic array allows us to treat the scatterers as non-interacting, provided we use a sufficiently large distance between neighboring scatterers. This leads to a detailed model for scattering from the aperiodic array based on summing up contributions from each scatterer using the scattering profile of a single scatterer, and taking into account the scattering direction and light propagation distances in different media. The experiments are convincingly modelled, both for the backward- and forward-scattered light. With the correct scattering profile for a single strip, the complex experimental diffraction pattern is accurately reproduced. Importantly, the comparison proved very sensitive to the single strip scattering profile used in the model. Thus, we find that our technique enables sensitive experimental verification of simulated angular scattering profiles.

Acknowledgments

The authors gratefully acknowledge financial support from the PLATOS project "Localized-surface plasmons and silicon thin-film solar cells", financed by the Villum Foundation.

References

1. H. A. Atwater and A. Polman, "Plasmonics for improved photovoltaic devices," Nat. Mater. **9**, 205–213 (2010).
2. P. Spinelli, V. E. Ferry, J. van de Groep, M. van Lare, M. A. Verschuuren, R. E. I. Schropp, H. A. Atwater, and A. Polman, "Plasmonic light trapping in thin-film Si solar cells," J. Opt. **14**, 024002 (2012).
3. K. Catchpole and A. Polman, "Plasmonic solar cells," Opt. Express **16**, 21793–21800 (2008).
4. L. Novotny and N. Van Hulst, "Antennas for light," Nat. Photonics **5**, 83 (2011).
5. T. Søndergaard, Y.-C. Tsao, P. K. Kristensen, T. G. Pedersen, and K. Pedersen, "Light trapping in guided modes of thin-film silicon-on-silver waveguides by scattering from a nanostrip," J. Opt. Soc. Am. B **31**, 2036–2044 (2014).
6. J. Jung, T. Søndergaard, T. G. Pedersen, K. Pedersen, A. N. Larsen, and B. B. Nielsen, "Dyadic Green's functions of thin films: Applications within plasmonic solar cells," Phys. Rev. B **83**, 085419 (2011).
7. W. Lukosz and R. E. Kunz, "Light emission by magnetic and electric dipoles close to a plane interface. I. total radiated power," J. Opt. Soc. Am. **67**, 1607–1615 (1977).
8. J. Mertz, "Radiative absorption, fluorescence, and scattering of a classical dipole near a lossless interface: a unified description," J. Opt. Soc. Am. B **17**, 1906–1913 (2000).
9. C. Langhammer, B. Kasemo, and I. Zorić, "Absorption and scattering of light by Pt, Pd, Ag, and Au nanodisks: Absolute cross sections and branching ratios," J. Chem. Phys. **126**, 194702 (2007).
10. D. D. Evanoff and G. Chumanov, "Size-controlled synthesis of nanoparticles. 2. measurement of extinction, scattering, and absorption cross sections," J. Phys. Chem. B **108**, 13957–13962 (2004).
11. W. Lukosz, "Light emission by magnetic and electric dipoles close to a plane dielectric interface. III. radiation patterns of dipoles with arbitrary orientation," J. Opt. Soc. Am. **69**, 1495–1503 (1979).
12. W. Lukosz and R. E. Kunz, "Light emission by magnetic and electric dipoles close to a plane dielectric interface. II. radiation patterns of perpendicular oriented dipoles," J. Opt. Soc. Am. **67**, 1615–1619 (1977).
13. A. Abass, P. Gutsche, B. Maes, C. Rockstuhl, and E. R. Martins, "Insights into directional scattering: from coupled dipoles to asymmetric dimer nanoantennas," Opt. Express **24**, 19638–19650 (2016).
14. S. R. J. Brueck, "Radiation from a dipole embedded in a dielectric slab," IEEE J. Sel. Top. Quantum Electron. **6**, 899–910 (2000).
15. C. Huang, A. Bouhelier, G. Colas des Francs, A. Bruyant, A. Guenot, E. Finot, J.-C. Weeber, and A. Dereux, "Gain, detuning, and radiation patterns of nanoparticle optical antennas," Phys. Rev. B **78**, 155407 (2008).
16. A. G. Curto, G. Volpe, T. H. Taminiau, M. P. Kreuzer, R. Quidant, and N. F. van Hulst, "Unidirectional emission of a quantum dot coupled to a nanoantenna," Science **329**, 930–933 (2010).

Received 21 Feb 2019; revised 9 Apr 2019; accepted 11 Apr 2019; published 2 May 2019

Optics EXPRESS

17. T. Coenen, E. J. R. Vesseur, A. Polman, and A. F. Koenderink, "Directional emission from plasmonic Yagi-Uda antennas probed by angle-resolved cathodoluminescence spectroscopy," Nano Lett. **11**, 3779–3784 (2011).
18. M. Schwind, V. D. Miljković, M. Zäch, V. Gusak, M. Käll, I. Zorić, and P. Johansson, "Diffraction from arrays of plasmonic nanoparticles with short-range lateral order," ACS Nano **6**, 9455–9465 (2012).
19. E. Skovsen, T. Søndergaard, J. Fiutowski, H.-G. Rubahn, and K. Pedersen, "Surface plasmon polariton generation by light scattering off aligned organic nanofibers," J. Opt. Soc. Am. B **29**, 249–256 (2012).
20. K.-H. Su, Q.-H. Wei, X. Zhang, J. J. Mock, D. R. Smith, and S. Schultz, "Interparticle coupling effects on plasmon resonances of nanogold particles," Nano Lett. **3**, 1087–1090 (2003).
21. W. Rechberger, A. Hohenau, A. Leitner, J. Krenn, B. Lamprecht, and F. Aussenegg, "Optical properties of two interacting gold nanoparticles," Opt. Commun. **220**, 137 – 141 (2003).
22. T. M. Søndergaard, *Green's Function Integral Equation Methods in Nano-Optics* (CRC Press, 2019). (Chap. 4).
23. Y. Mizokawa, O. Komoda, and S. Miyase, "Long-time air oxidation and oxide-substrate reactions on GaSb, GaAs and GaP at room temperature studied by X-ray photoelectron spectroscopy," Thin Solid Films **156**, 127 – 143 (1988).
24. L. Feng, L.-D. Zhang, H. Liu, X. Gao, Z. Miao, H.-C. Cheng, L. Wang, and S. Niu, "Characterization study of native oxides on GaAs(100) surface by XPS," Proc. SPIE **8912**, 89120N (2013).
25. W. Cai, H. Zhong, and L. Zhang, "Optical measurements of oxidation behavior of silver nanometer particle within pores of silica host," J. Appl. Phys. **83**, 1705–1710 (1998).
26. M. D. McMahon, R. Lopez, H. M. Meyer, L. C. Feldman, and R. F. Haglund, "Rapid tarnishing of silver nanoparticles in ambient laboratory air," Appl. Phys. B **80**, 915–921 (2005).
27. Optical data from Sopra SA, "GaAs optical constants," http://www.sspectra.com/sopra.html.

Received 21 Feb 2019; revised 9 Apr 2019; accepted 11 Apr 2019; published 2 May 2019

Paper C

Auminum nanoparticles for plasmon-improved coupling of light into silicon

List of Authors:

T. F. Villesen
C. Uhrenfeldt
B. Johansen
J. Lundsgaard Hansen
H. U. Ulriksen
A. Nylandsted Larsen

The paper has been published in
Nanotechnology Vol. 23(8), pp. 085202, 2012.

The layout has been revised.

IOP PUBLISHING NANOTECHNOLOGY
Nanotechnology **23** (2012) 085202 (4pp) doi:10.1088/0957-4484/23/8/085202

Aluminum nanoparticles for plasmon-improved coupling of light into silicon

T F Villesen[1], Christian Uhrenfeldt[2], B Johansen[2], J Lundsgaard Hansen[2], H U Ulriksen[3] and Arne Nylandsted Larsen[2]

[1] Interdisciplinary Nanoscience Center, Aarhus University, Ny Munkegade 120, 8000 Aarhus C, Denmark
[2] Department of Physics and Astronomy, Aarhus University, Ny Munkegade 120, 8000 Aarhus C, Denmark
[3] Department of Physics and Nanotechnology, Aalborg University, Skjernvej 4a, 9220 Aalborg East, Denmark

E-mail: tfv05@inano.au.dk

Received 5 December 2011
Published 1 February 2012
Online at stacks.iop.org/Nano/23/085202

Abstract
This paper investigates the improved photo-current response obtained by depositing Al nanoparticles on top of a Si diode. Well defined Al nanodiscs with a diameter and height of 100 nm are produced on the surface of a Si diode using electron-beam lithography, and the change in photo-current generation is characterized. A blue shift of the photo-current response is demonstrated, substantially improving the relation between gains and losses compared to what is typically observed in similar schemes using Ag nanoparticles. Enhanced photo-current response is observed in diodes with Al particles on the surface at all wavelengths larger than ≈465 nm, thereby minimizing the losses in the blue range usually reported with Ag nanoparticles on the surface.

(Some figures may appear in colour only in the online journal)

The low absorption coefficient in silicon for light in the red to near infrared (NIR) region is an inherent problem for Si thin-film solar cells, resulting in poor efficiencies. Exploiting the special scattering abilities of localized surface-plasmon resonances (LSPRs) in metallic nanoparticles has recently received much attention as a means to increase coupling of light into Si.

Several groups have demonstrated this approach using Ag metal particles deposited on the surface of thin-film Si solar cells [1–8], and have generally achieved photo-current gain at wavelengths in the visible to the NIR region. A substantial loss is also observed, however, at wavelengths below a certain cross-over point (λ_{cross}), typically in a region where the solar spectrum is still very intense [7, 5, 9, 2], resulting in a poor relationship between gains and losses.

Based on the interpretations of [10, 9, 4] the cross-over point is closely related to the position of the LSPR in the particles, which makes it highly interesting to blue shift the LSPR and thereby improve the balance between reduction and enhancement effects from the particles [11, 10, 12].

The position of the LSPR can be tuned by varying the size (d and h), shape (L) and dielectric function of the particle (ϵ_p) [13]. For particles large compared to the wavelength of light the LSPR can be blue shifted considerably by lowering the size of the particle. Decreasing the nanoparticle size, however, also leads to a decrease in the scattering efficiency of the particles. The LSPR can also be blue shifted by increasing the shape factor L (described in [13]). The range of possible L values, which increases with the height to diameter disc aspect ratio, however, may be limited by practical concerns in the synthesis of nanoparticles.

The dielectric function of the particle is determined by the chosen material. Silver can support a strong resonance, which is widely tunable by the methods mentioned above, but it appears to be difficult to blue shift the cross-over point below 500 nm while maintaining a sufficiently large nanoparticle. To avoid losing too much sunlight at wavelengths smaller than the cross-over point, 500 nm is not far enough towards the blue. Aluminum, on the other hand, also supports a strong plasmon resonance, which has been shown to be tunable from

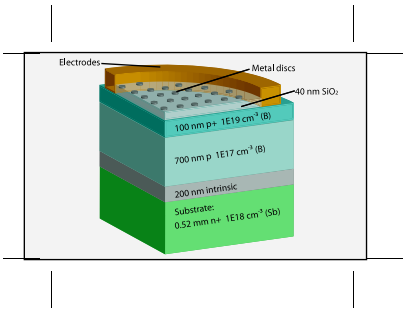

Figure 1. Sketch of the inverted Si diode structure used in the experiments. All layers were grown on an n^+ substrate using molecular-beam epitaxy.

the infrared to the ultraviolet by varying the shape and size of the particle [14, 15]. Assuming that Al particles on the surface of a solar cell behave in a way similar to the trend described above for Ag particles, this opens up the possibility of blue shifting the cross-over point closer to the edge of the solar spectrum than what is reported for Ag particles [5, 9, 2]. The present investigation will demonstrate the feasibility of this approach. We have not aimed at optimizing the system with respect to e.g. maximum in-coupling of light but have mainly focused on the proof of concept.

Usually particles on the surface of a solar cell are separated from the silicon surface by a thin dielectric layer, which has a strong effect on the scattering properties of the particles [16]. Choosing a host material with a low refractive index will cause a blue shift of the resonance. Thus in order to obtain the maximum blue shift a dielectric of low refractive index such as SiO_2 is preferable. This has been used in the present investigation.

All experiments were made on an inverted diode structure made by molecular-beam epitaxy (MBE) as shown in figure 1. A 700 nm layer of boron doped p-type Si (1×10^{17} B cm^{-3}) was grown on top of a highly Sb doped n-type substrate (1×10^{18} Sb cm^{-3}) with a 200 nm intrinsic Si layer in between to extend the pn junction. On top of the p-type Si layer a 100 nm p^+ Si layer (1×10^{19} B cm^{-3}) was added for improved ohmic contact with the Al electrodes, and for reduction of surface recombination by a front-surface field. The MBE growth was carried out at a pressure of 2×10^{-10} mbar at a growth rate of 3 Å s^{-1} with the substrate heated to 700 °C. Finally, all diodes had a 40 nm SiO_2 layer deposited on top by magnetron sputtering.

Using electron-beam lithography (EBL), one sample was prepared with Al discs with diameter (d) of 100 nm and height (h) of 100 nm placed in an array with periodicity 400 nm on the SiO_2-layer on the surface of the diode (figure 2(a)). In order to demonstrate the well established effect of Ag, a sample with Ag discs of diameter 100 nm and height 25 nm was also prepared (figure 2(b)). The NP where characterized by SEM (shape and diameter) and AFM (height). The external quantum efficiencies (EQEs) of the diodes were derived from photo-current (PC) measurements using an Oriel MS257 monochromator and a calibrated Newport 818UV photodiode.

In figures 3(a) and (b) the effect on the EQEs of the diodes by depositing Al and Ag particles on the surface is shown, respectively, together with the corresponding reference measurements. The relative gain is calculated by dividing with the EQE of an identical reference diode without particles, and is also shown in figures 3(c) and (d). Note that the reference diode is not a bare Si but also has a 40 nm SiO_2 layer on the surface. Overall, the Al particles show the same trend as the Ag particles (losses at shorter wavelengths and gain at longer wavelengths), however, with a substantial blue shift of the cross-over point compared to what is reported for Ag particles. This has a strong positive effect on the overall gain as will be described further below. Compared to the Ag-demonstration sample in this article, the cross-over point for the sample with Al particles is blue shifted ≈105 nm, while maintaining a gain on the long wavelength side similar to what is measured with Ag. For Al, a relative gain in the EQE of up to 5% is seen at all wavelengths from the cross-over point at $\lambda_{cross}^{Al} = 465$ nm to the edge of the spectrum in the NIR. At wavelengths below the cross-over point a reduction of up to 14% is observed. For Ag a relative gain in the EQE

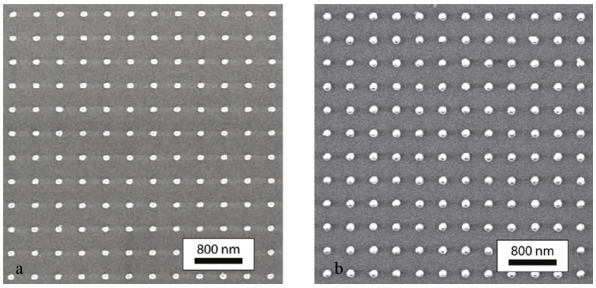

Figure 2. SEM images showing (a) Al and (b) Ag nanodiscs on the surface of the diode.

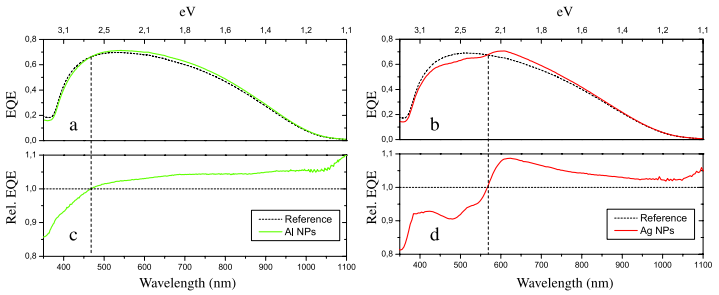

Figure 3. Measured external quantum efficiency (top) and calculated relative photo-current response (bottom) showing the effect of Al (a) and (c) and Ag (b) and (d) particles on the surface of a thin solar cell. The cross-over points are at $\lambda = 465$ nm and $\lambda = 570$ nm for Al and Ag respectively.

of up to 9% is observed at all wavelengths longer than 570 nm and a relative loss of up to 19% at shorter wavelengths, which is similar to what is reported in the literature for Ag particles on the surface of a solar cell.

The observed blue shift may be explained by considering the plasmonic properties of Al nanoparticles compared to Ag nanoparticles. Zoric *et al* showed that the LSPR in metal particles can be described by a relatively simple analytical expression based on the electrostatic approximation and the modified long wavelength approximation, using values of the metal–dielectric functions from the literature. Agreement of the model with experimentally observed LSPR wavelengths for a large range of disc sizes and aspect ratios, including the particles studied here, was also demonstrated by Zoric *et al*.

The polarizability of a particle shaped like an oblate spheroid in the electrostatic approximation is given by [13]:

$$\alpha(\lambda) = \frac{4\pi a^2 b}{3} \frac{\varepsilon_{\mathrm{NP}}(\lambda) - \varepsilon_{\mathrm{h}}(\lambda)}{\varepsilon_{\mathrm{h}}(\lambda) + L[\varepsilon_{\mathrm{NP}}(\lambda) - \varepsilon_{\mathrm{h}}(\lambda)]} \tag{1}$$

where a and b (defined here as $a = d/2$ and $b = h/2$) are the major and minor axis of the particle, respectively, $\epsilon_{\mathrm{NP}}(\lambda)$ and $\epsilon_{\mathrm{h}}(\lambda)$ are the complex dielectric functions of the nanoparticle material and of the surrounding host material, respectively, and L is the geometrical factor as defined in [13]. For larger particles, like the ones used here, the polarization can be corrected using the modified long wavelength approximation to include finite wavelength effects [17, 14]:

$$\alpha\,(k)_{\mathrm{MLWA}} = \frac{\alpha(k)}{1 - \mathrm{i}\frac{k^3}{6\pi}\alpha(k) - \frac{k^2}{4\pi a}\alpha(k)} \tag{2}$$

where $k = \frac{2\pi n_{\mathrm{h}}}{\lambda}$. In our geometry shown in figure 1 $\varepsilon_{\mathrm{h}} = (n_{\mathrm{h}})^2 = (1.26)^2$ as in [15]. By inserting (1) into (2) and using the dielectric functions $\epsilon_{\mathrm{NP}}(k)$ from the literature [18, 19] the polarizability can be calculated numerically.

Figure 4 shows the predicted position of the LSPR, using this model for particles with heights of 25 and 100 nm, as a function of inverse diameter for Ag and Al on SiO_2. It can be seen that for a given particle size and shape the LSPRs for Al particles are closer to the UV than for Ag particles.

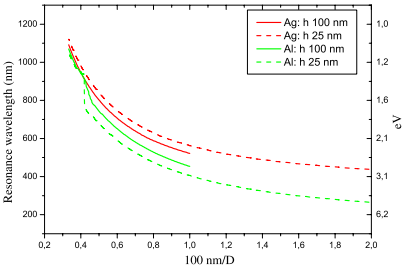

Figure 4. Predicted LSPR positions for Ag and Al particles on SiO_2 with heights $h = 25$ and 100 nm and diameters ranging from $d = 50$–500 nm.

This shows that the position of the LSPR can be blue shifted by replacing Ag with Al as a nanoparticle material. The Al particles investigated in this experiment ($h = 100$ nm, $d = 100$ nm) are predicted to have an LSPR at $\lambda^{\mathrm{Al}}_{\mathrm{LSPR}} = 450$ nm, whereas Ag particles with this shape have a resonance around $\lambda^{\mathrm{Ag}}_{\mathrm{LSPR}} = 520$ nm. The experimental Ag particles included as an example here ($h = 25$ nm, $d = 100$ nm) are predicted to have a resonance at $\lambda^{\mathrm{Ag}}_{\mathrm{LSPR}} = 560$ nm. As can be seen from figure 4 the predicted blue shift of the LSPR wavelength between the Ag and Al nanoparticles from 560 to 450 nm is in excellent agreement with the observed blue shift of the cross-over point from 570 to 465 nm. This strongly supports the concept of blue shifting the cross-over point in the photo-current response by using Al discs as light scatterers instead of Ag on the surface of a solar cell.

The relationship between gains and losses is strongly dependent on the position of the cross-over point in relation to the intensity profile of the solar spectrum. To evaluate this more quantitatively the total effect of the metal particles is found by integrating the EQE weighted with the AM1.5 photon flux as a function of wavelength for samples with and without metal particles on the surface and calculating the

relative difference:

$$PC^{X}_{\lambda_1-\lambda_2} = \int_{\lambda_1}^{\lambda_2} [EQE^{X}(\lambda) \times F_{\text{phot}}(\lambda)]\, \mathrm{d}\lambda$$

$$G = \frac{PC^{\text{NP}}_{\lambda_1-\lambda_2} - PC^{\text{ref}}_{\lambda_1-\lambda_2}}{PC^{\text{ref}}_{\lambda_1-\lambda_2}}.$$

G is the total gain/loss from λ_1 to λ_2, EQE^X is the external quantum efficiency of the sample with Al, Ag or no particles and F_{phot} is the AM1.5 photon flux. Because of the particular shape of the gain curve described above, the total relative loss in photo-current from applying the particles is given by integrating from λ_{min} (minimum wavelength in the solar spectrum) to the cross-over point whereas the total relative gain is given by integrating from the cross-over point to λ_{bandgap}.

When calculated this way, the Ag sample shown above has an integrated photo-current gain of 3.7% from 570 to 1200 nm and a loss of 2.5% from 300 to 570 nm when compared to the reference sample, giving a total gain of 1.2% for the whole photo-current spectrum. The Al sample on the other hand has an integrated gain of 3.0% from 465 to 1200 nm but a loss of only 0.3% from 300 to 465 nm giving a total gain of 2.8%. It is clear that even with a smaller gain at longer wavelengths than with Ag, the Al particles have a higher total gain benefitting from blue shifting the losses out of the solar spectrum. The system reported here is a proof of concept, and further improvements may be gained by optimization. As is evident from the calculation above that not much can be gained by blue shifting further, improving the shape and amplitude of the gain on the long wavelength side of the cross-over point is the main challenge, similar to what has previously been done numerically in [11] for Ag and Al and experimentally for Ag in [6].

In summary we have demonstrated the possibility of using Al nanoparticles on the surface of a thin-film solar cell to enhance photo-current generation. It is shown that by using Al particles the cross-over point where the relative photo-current changes from gain to loss can be blue shifted substantially compared to Ag, reducing losses and improving the overall effect of the particles.

Acknowledgment

We acknowledge financial support from the project 'Localized surface plasmons and Si thin-film solar cells—PLATOS' financed by the Villum Foundation.

References

[1] Atwater H A and Polman A 2010 Plasmonics for improved photovoltaic devices *Nature Mater.* **9** 205–13

[2] Stuart H R and Hall D G 1996 Absorption enhancement in silicon on insulator waveguides using metal island films *Appl. Phys. Lett.* **69** 2327–9

[3] Schaadt D M, Feng B and Yu E T 2005 Enhanced semiconductor optical absorption via surface plasmon excitation in metal nanoparticles *Appl. Phys. Lett.* **86** 063106

[4] Derkacs D, Lim S H, Matheu P, Mar W and Yu E T 2006 Improved performance of amorphous silicon solar cells via scattering from surface plasmon polaritons in nearby metallic nanoparticles *Appl. Phys. Lett.* **89** 093103

[5] Pillai S, Catchpole K R, Trupke T and Green M A 2007 Surface plasmon enhanced silicon solar cells *J. Appl. Phys.* **101** 093105

[6] Spinelli P, Hebbink M, de Waele R, Black L, Lenzmann F and Polman A 2011 Optical impedance matching using coupled plasmonic nanoparticle arrays *Nano Lett.* **11** 1760–5

[7] Beck F J, Polman A and Catchpole K R 2009 Tunable light trapping for solar cells using localized surface plasmons *J. Appl. Phys.* **105** 114310

[8] Uhrenfeldt C, Hansen J L, Villesen T F, Jung J, Ulriksen H U, Pedersen T G, Pedersen K and Larsen A N 2010 Effects of disc shape on plasmon enhanced optical absorption in solar cells *Proc. 25th PVSEC* pp 637–40

[9] Hägglund C, Zäch M, Petersson G and Kasemo B 2008 Electromagnetic coupling of light into a silicon solar cell by nanodisk plasmons *Appl. Phys. Lett.* **92** 053110

[10] Akimov Y A and Koh W S 2010 Resonant and nonresonant plasmonic nanoparticle enhancement for thin-film silicon solar cells *Nanotechnology* **21** 235201

[11] Akimov Y A, Koh W S and Ostrikov K 2009 Enhancement of optical absorption in thin-film solar cells through the excitation of higher-order nanoparticle plasmon modes *Opt. Express* **17** 10195–205

[12] Pors A, Uskov A V, Willatzen M and Protsenko I E 2011 Control of the input efficiency of photons into solar cells with plasmonic nanoparticles *Opt. Commun.* **284** 2226–9

[13] Bohren C F and Huffman D R 1983 *Absorption and Scattering of Light by Small Particles* (New York: Wiley Interscience)

[14] Langhammer C, Schwind M, Kasemo B and Zoric I 2008 Localized surface plasmon resonances in aluminum nanodisks *Nano Lett.* **8** 1461–71 PMID: 18393471

[15] Zoric I, Zäch M, Kasemo B and Langhammer C 2011 Gold, platinum, and aluminum nanodisk plasmons: material independence, subradiance, and damping mechanisms *ACS Nano* **5** 2535–46

[16] Pillai S, Beck F J, Catchpole K R, Ouyang Z and Green M A 2011 The effect of dielectric spacer thickness on surface plasmon enhanced solar cells for front and rear side depositions *J. Appl. Phys.* **109** 073105

[17] Zeman E J and Schatz G C 1987 An accurate electromagnetic theory study of surface enhancement factors for silver, gold, copper, lithium, sodium, aluminum, gallium, indium, zinc, and cadmium *J. Phys. Chem.* **91** 634–43

[18] Rakić A D 1995 Algorithm for the determination of intrinsic optical constants of metal films: application to aluminum *Appl. Opt.* **34** 4755–67

[19] Hagemann H J, Gudat W and Kunz C 1975 Optical constants from the far infrared to the x-ray region: Mg, Al, Cu, Ag, Au, Bi, C, and $A_{12}O_3$ *J. Opt. Soc. Am.* **65** 742–4

Paper D

Optical transmission through two-dimensional arrays of β-Sn nanoparticles

List of authors:

B. Johansen
C. Uhrenfeldt
A. N. Larsen
T. G. Pedersen
H. U. Ulriksen
P. K. Kristensen
J. Jung
T. Søndergaard
K. Pedersen

The paper has been published in the
Phys. Rev. B. Vol. 84(11), pp. 113405, 2011.

The layout has been revised.

PHYSICAL REVIEW B **84**, 113405 (2011)

Optical transmission through two-dimensional arrays of β-Sn nanoparticles

Britta Johansen, Christian Uhrenfeldt, and Arne Nylandsted Larsen
Department of Physics and Astronomy, Aarhus University, Ny Munkegade 120, DK-8000 Aarhus C, Denmark

Thomas Garm Pedersen, Hans Ulrik Ulriksen, Peter Kjær Kristensen, Jesper Jung, Thomas Søndergaard, and Kjeld Pedersen
Department of Physics and Nanotechnology, Aalborg University, Skjernvej 4A, DK-9220 Aalborg East, Denmark
(Received 25 May 2011; revised manuscript received 13 July 2011; published 12 September 2011)

We present measurements of the collinear optical transmission through arrays of β-Sn nanoparticles on fused silica substrates. The particles are cylinders or squares with side lengths of 120–520 nm, and heights of 26–118 nm placed in square-periodic arrays fabricated by electron-beam lithography. By placing the 120 nm cylinders in an index-matched environment peaks appear in the transmission spectrum at wavelengths where the diffracted light propagates at a grazing angle to the substrate. Angle-resolved transmission measurements show that the peak positions depend on the angle of incidence, and the shift of the peaks is in excellent agreement with theoretical calculations of the dipole lattice sum. The peak positions can also be matched by a simple wave-vector analysis. The larger square particles show resonant dips in the transmission even without index matching, and the depth of the dips depends on the particle height. By index matching the environment around the large particles, the dips are replaced by peaks.

DOI: 10.1103/PhysRevB.84.113405 PACS number(s): 78.67.Bf, 42.25.Fx

Metallic nanoparticles have been intensively studied with the aim to enhance light trapping in silicon solar cells.[1–3] In the search for the optimal particle properties, materials such as gold and aluminum have attracted much attention.[4] Another material which has a large potential is metallic Sn[5], as Sn and Si both are group-IV elements. This means that Sn is electrically neutral as a substitutional impurity without midgap defect levels[6] in the Si lattice and hence is compatible with integration in Si-based photovoltaics. This is further described by Jung *et al.*[7] In relation to solar cells, metal nanoparticles are often arranged in arrays, which emphasizes the need to understand the optical mechanisms in such arrays. It is especially interesting to clarify whether diffractive effects dominate the spectral response from the particles or is a minor effect. Optical investigations of nanoparticle arrays have previously been reported,[8–12] but these mostly concentrate on strong plasmonic materials such as gold and silver. In particular, work has focused on light scattering either via plasmons or grating resonances that redirect light into directions favorable for absorption within the solar cell.

That gratings can introduce unusual optical effects was already reported by Wood in 1902 (Ref. 13) as he observed anomalous reflection bands from one-dimensional diffraction gratings. These anomalies were theoretically investigated in 1907 by Rayleigh,[14] and are often referred to as Rayleigh-Wood anomalies. The anomalies appear as the diffracted light becomes grazing to the plane of the grating.

For a two-dimensional particle array with period a in both directions this occurs when

$$\left(\frac{n_2}{\lambda}\right)^2 - \left(\frac{n_1}{\lambda}\right)^2 \sin^2\theta - 2\frac{n_1}{\lambda}\sin\theta\left(\frac{n}{a}\cos\varphi + \frac{m}{a}\sin\varphi\right) = \frac{n^2+m^2}{a^2}, \quad (1)$$

where λ is the wavelength of the incident light, (m,n) denotes the diffraction order, n_1 and n_2 are the refractive incidences of the super- and substrate, respectively, θ is the angle of incidence, and φ defines the angle between the (1,0) grating plane and the plane of the incoming light.

In this Brief Report we show that the grating-induced effects do play a very important role in the optical response of the Sn particles. We observe a significant positive correlation between the spectral position of the anomalies in the measured transmission spectra of Sn particle arrays and the peaks in the theoretically calculated lattice sum of the array. Furthermore, our results corroborate the theoretical findings of Auguié *et al.*[15] who showed that for particle arrays the Rayleigh-Wood anomaly can be suppressed by a reflecting surface close to the particles as long as the particles are small.

Most of the experimental results below are for cylindrical particles with diameter 120 nm and height 40 nm. Hence, for wavelengths in the visible/infrared we expect the dipole approximation to be reasonably accurate. We follow the coupled dipole approach of Refs. 16 and 17 and consider the index-matched case, in which each particle is described as a dipole placed in a homogeneous medium. Care is taken that the spot size in the transmission experiments is always within the sample area of $\sim$4 mm^2; thus all particles probed represent particles within the array. Through dipole-dipole coupling, the nth dipole placed at $\vec{r}_n$ induces an electric field at $\vec{r}_0$, which is proportional to $\overleftrightarrow{G}(\vec{r}_0,\vec{r}_n)\cdot\hat{p}$, where $\overleftrightarrow{G}$ is the dyadic Green's function and $\hat{p}$ is a unit vector along the dipole moment.[16,17] If the polarizability of isolated particles is α, the dipole-dipole coupling included via a dipole-lattice sum S means that the dipole moments in the array are governed by an effective polarizability $\alpha_{\mathrm{eff}} = \alpha/(1-\alpha S)$. Resonances are generally associated with the poles of α_{eff} but if α is only weakly frequency dependent, the resonances coincide with discrete diffraction orders associated with the poles of S. For dipole arrays in homogeneous media, S is given by

$$S = k_0^2 \sum_{n\neq 0} \hat{p}\cdot\overleftrightarrow{G}(\vec{r}_0,\vec{r}_n)\cdot\hat{p}\, e^{i\vec{k}_1\cdot(\vec{r}_n-\vec{r}_0)}, \quad (2)$$

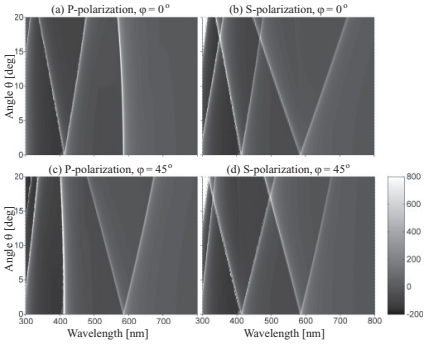

FIG. 1. Calculated real part of the lattice sum S in units of μm^{-3} for different polarizations and incident angles. The lattice period is 400 nm and the surrounding medium has a refractive index of 1.46.

where $k_0 = \frac{2\pi}{\lambda}$, $\vec{k}_\parallel$ is the wave-vector component parallel to the surface, and $\vec{r}_0$ is the center position in the array. In practice, we sum over a finite $N \times N$ lattice with $N = 401$. This means that the poles of S become finite peaks in the spectrum but also produce an unphysical oscillatory modulation with a period inversely proportional to N. We remove this artifact by averaging the spectrum over one period.

The real part of the calculated lattice sums S at different angles of incidence θ is shown in Fig. 1 for both S- and P-polarized incident light and φ equal to 0° and 45°. Peaks are seen in the S sum at wavelengths satisfying Eq. (1). At $\theta = 0°$ the peak at 584 nm originates from the (1,0) diffraction order while the peak at 413 nm originates from the (1,1) diffraction order. In Figs. 1(b) and 1(d), where the light is S polarized, the two peaks in the S sum both split when θ is increased from zero, as the diffracted light can be grazing to one or the other side. In the case of P-polarized light shown in Figs. 1(a) and 1(c), only one of the two peaks splits. The physical explanation for this is that in the case of P-polarized light the electric field is lying in the plane of incidence in which θ is also varied. As the dipoles primarily couple in the direction perpendicular to the driving E field the coupling between the particles will not change significantly as θ is increased. In Fig. 1(a), $\varphi = 0$ and the plane of incidence therefore goes through the (1,0) direction, and as the incident light is P polarized the (1,0) peak in the figure does not split. Likewise when $\varphi = 45°$ and the light is P polarized the (1,1) peak does not split as seen in Fig. 1(c). A closer look at Figs. 1(a) and 1(c) shows that both the (1,0) and the (1,1) peak undergo a slight blueshift as θ is increased.

In our experiments we investigated these polarization-dependent resonance phenomena through angle-resolved transmission measurements of Sn-particle arrays on fused silica. The Sn particles were fabricated by electron-beam lithography, which is a technique that provides excellent control over the shape and position of each particle. To reduce charging effects in the electron-beam writing process

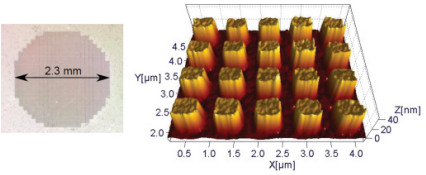

FIG. 2. (Color online) Left: Microscope image of the area covered by Sn particles. The area consists of 437 0.1 × 0.1 mm write fields each containing 250 × 250 particles. Right: AFM picture of an array with period 800 nm consisting of square Sn particles having side lengths of 510 nm and heights of 25 nm.

the resist was coated with a 20 nm aluminum layer. After resist exposure the aluminum layer was removed with a KOH solution. The spatial extent of the particle array was a circular area with a diameter of 2.3 mm as shown to the left in Fig. 2. The Sn particles were investigated both by scanning electron microscopy (SEM) and atomic force microscopy (AFM). An AFM picture is shown to the right in Fig. 2. Generally, the heights of the particles were found from the AFM picture while the side lengths and periods were found from the SEM pictures.

Optical-transmission spectra were obtained by measuring the directly transmitted light through the samples using a Shimadzu UV3600 dual-beam photospectrometer with spot size 1.8 mm and beam divergence 3.5°. The transmission spectrum for cylindrical Sn particles having a diameter of 120 nm, a height of 40 nm, and a period of 400 nm is shown in Fig. 3(a). The Sn coverage of the surface was 6%. Here the sample was illuminated by unpolarized light at

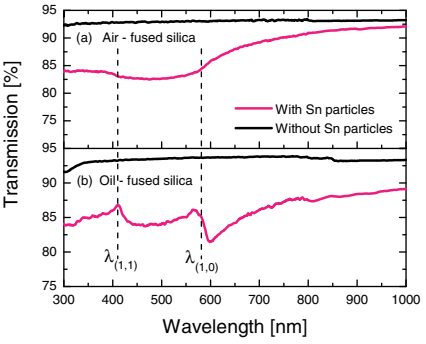

FIG. 3. (Color online) Transmission spectra of cylindrical Sn particles with diameter 120 nm, height 40 nm, and period 400 nm illuminated by unpolarized light at normal incidence. The superstrate is air (a) and index-matched oil (b). A reference spectrum of the bare substrate is shown. The vertical dotted lines show the theoretical positions of the Rayleigh-Wood anomalies according to Eq. (1).

normal incidence. The spectrum reveals a broad dip centered around 500 nm. This feature could be interpreted as a weak plasmon resonance but no conclusive evidence of such an assingment has been found. The theoretical wavelengths for the Rayleigh-Wood anomalies are calculated from Eq. (1) with $\theta = \varphi = 0$ and $n_2 = 1.46$. These wavelengths are shown by vertical dotted lines in Fig. 3 and the subscripts on λ denote the diffraction order (m,n). However, no Rayleigh-Wood anomalies are seen at the vertical lines in Fig. 3(a). As suggested by Auguié *et al.*,[15] the absence of an anomaly can be due to a reflecting interface close to the particles, which suppresses the interparticle coupling. By depositing an oil index matched to the substrate onto the sample, the reflecting interface is removed. Experimentally, a drop of index-matched oil was put on the sample and a clean piece of fused silica was placed on top to ensure a planar surface. The transmission spectrum after index matching is shown in Fig. 3(b). As the reflecting surface is eliminated features now appear at the expected wavelengths as marked by the vertical dotted lines. $\lambda_{(1,0)}$ lies exactly at a top in the spectra while $\lambda_{(1,0)}$ lies between a top and a dip. The spectral feature at $\lambda_{(1,0)}$ resembles the observations reported in Ref. 18, where the asymmetric feature arises due to a frequency-dependent particle polarizability in the region of the pole of S.

To test the theoretically calculated lattice sums shown in Fig. 1, angle-resolved transmission measurements using polarized light have been performed. The results are shown in Fig. 4. The theoretical peak positions from Fig. 1 are shown by vertical dotted lines for each angle. The agreement between the theoretically predicted positions of the anomalies and the measured values is excellent. In Figs. 4(a) and 4(c), only one of the two peaks splits while the other peak makes a slight blueshift when the incident angle is increased as theoretically predicted by the S sum. In the case of S polarization, both peaks split as expected, which can be seen in Figs. 4(b) and 4(d). Note that while the diffraction resonances are described by Eq. (1), the full lattice sum is needed to describe the polarization dependence.

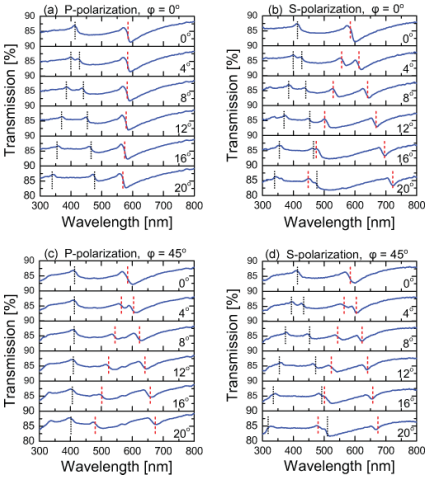

FIG. 4. (Color online) Angle-resolved transmission measurements of cylindrical Sn particles with a diameter of 120 nm, a height of 40 nm, and a period of 400 nm in an index-matched environment. The angle φ and the polarization of the incident light are specified in each graph. The peak positions of the lattice sum in Fig. 1 are shown by vertical dotted lines.

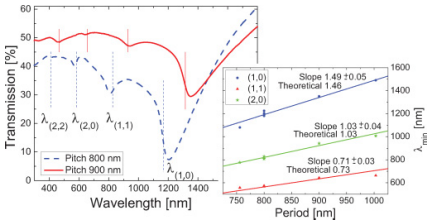

FIG. 5. (Color online) Left: Measured transmission spectra at normal incidence for square particles with different array periods. Dashed curve: Particles with side length 490 nm, height 100 nm, and surface coverage 33%. Solid curve: Particles with side length 520 nm, height 120 nm, and surface coverage 27%. Vertical lines show $\lambda_{(m,n)}$ for array periods 800 (dashed) and 900 nm (solid) according to Eq. (1). Right: Dip positions in the transmission vs array period. The theoretical slopes are calculated from Eq. (1) with $n_2 = 1.46$.

In addition, Sn particles with larger sizes than those presented above were investigated. Transmission spectra measured at normal incidence for two samples with square-Sn particles are shown to the left in Fig. 5. The samples have array periods of 800 and 900 nm and consist of particles with side lengths of 490 and 520 nm and heights of 100 and 120 nm, respectively. Unlike the case of the small particles, it is now possible to see the anomalies in the asymmetric index environment without index-matched oil. The reason for this is that the larger volume, and hence larger polarizability of the particles, makes the anomaly dominate over the reflection damping. This is in agreement with the theoretical predictions by Auguié *et al.*[15] The theoretical wavelengths for horizontal diffraction in the fused silica substrate are calculated from Eq. (1) and shown by vertical dotted lines for the two periods in Fig. 5. There is a clear correspondence between the dip positions and the $\lambda_{(m,n)}$ values. The depth of the dips is notable. The sample with array period 800 nm only lets 8% of the incident 1200 nm light pass through, meaning that 92% of the light is blocked or scattered although only 33% of the fused silica surface is covered by Sn particles. In other words, the particles block three times as much light as would be expected from the geometrical cross section, which indicates a resonant character of the extinction mechanism. Additional transmission measurements of arrays with different periods have been performed (not shown here). They showed similar dips and the three most dominant dip positions for each sample are plotted vs the array period in the inset to the right in Fig. 5. The plot reveals a linear dependence of the dip position on the

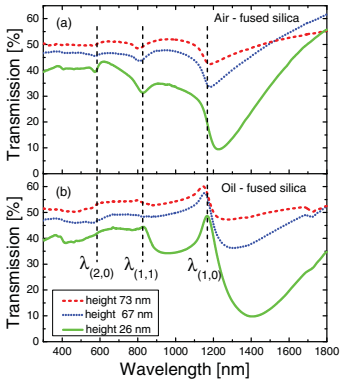

FIG. 6. (Color online) Transmission spectra of almost identical particles with an array period of 800 nm, width around 500 nm, and different heights. In (a), the superstrate is air and in (b) it is index-matched oil.

array period in agreement with Eq. (1). The theoretical slope values given by $n_2/\sqrt{n^2+m^2}$ with $n_2 = 1.46$ are shown in the figure and, by comparison, it is seen that the experimental and theoretical slopes agree within the uncertainties. It should be noted that although the shape and size of the particles vary in the arrays represented in Fig. 5 (inset), this does not affect the position of the dips.

In order to investigate the effect of the particle height on the optical transmission we compare in Fig. 6 the transmission spectra of square Sn particles with an array period of 800 nm and heights of 73, 67, and 26 nm. The nanoparticle side lengths are nearly identical for the three samples, being 470, 500, and 510 nm, respectively. It appears from the three spectra that the depth of the dips increases with the particle height while the position of the dips is nearly unaffected, as already observed in Fig. 5. This height dependence can be caused by the difference in particle volume; decreasing the height reduces the particle volume and hence the magnitude of the polarizability and scattering cross section of the particles. At a fixed lattice spacing, a reduction in polarizability reduces the dipole coupling, which gives rise to a reduced optical fingerprint. An alternative explanation might be that as the particle height is reduced, the center of the particles moves closer to the substrate. This could give rise to a larger suppression of the Rayleigh-Wood anomaly due to the reflecting surface as described by Auguié *et al.*[15] By depositing an index-matched oil on the three samples shown in Fig. 6(a), the reflecting surface and hence this effect is eliminated. As can be seen from Fig. 6(b) a pronounced influence of the particle height on the spectral variation is still observed, which shows that the observed height dependence is most likely due to the change in particle volume. Interestingly, as can be seen in Fig. 6(b), at $\lambda_{(1,0)}$ we now find peaks in the transmission instead of dips, and indications of peaks at $\lambda_{(1,1)}$ and $\lambda_{(2,0)}$ are also observed. The reason why the dips change into peaks when index matching is at present not understood.

In summary, Rayleigh-Wood anomalies were observed in the transmission spectra of periodic arrays of 120 nm Sn particles when placed in an index-matched environment. Angle-resolved transmission measurements using polarized light revealed splitting and shifting peaks as the angle increased, in excellent agreement with the peaks in the theoretically calculated dipole-lattice sums. Investigations of larger Sn particles showed that these did not require an index-matched environment to show anomalies in the transmission spectra. This difference between the small and the large particles supports the theoretical predictions by Auguié *et al.*[15] The anomalies for the large particles with array period 800 nm were very strong. Up to 92% of the incident light was extinguished by the array, even though the Sn particles only covered 33% of the surface revealing a resonant extinction process.

We acknowledge financial support by the project "Localized surface plasmons and Si thin-film solar cells—PLATOS" financed by the Villum Foundation.

[1] H. A. Atwater and A. Polman, Nat. Mater. **9**, 205 (2010).
[2] Y. A. Akimov, W. S. Koh, and K. Ostrikov, Opt. Express **17**, 10195 (2009).
[3] K. R. Catchpole and A. Polman, Opt. Express **16**, 21793 (2008).
[4] T. L. Temple and D. M. Bagnall, J. Appl. Phys. **109**, 084343 (2011).
[5] T. G. Pedersen, P. Modak, K. Pedersen, N. E. Christensen, M. M. Kjeldsen, and A. N. Larsen, J. Phys.: Condens. Matter **21**, 115502 (2009).
[6] G. Weyer, A. N. Larsen, B. I. Deutch, J. U. Andersen, and E. Antoncik, Hyperfine Interact. **1**, 93 (1975).
[7] J. Jung, T. G. Pedersen, T. Søndergaard, K. Pedersen, A. N. Larsen, and B. B. Nielsen, Phys. Status Solidi (RRL) **4**, 292 (2010).
[8] V. G. Kravets, F. Schedin, and A. N. Grigorenko, Phys. Rev. Lett. **101**, 087403 (2008).
[9] Y. Chu, E. Schonbrun, T. Yang, and K. B. Crozier, Appl. Phys. Lett. **93**, 181108 (2008).
[10] N. Félidj, G. Laurent, J. Aubard, G. Lévi, A. Hohenau, J. R. Krenn, and F. R. Aussenegg, J. Chem. Phys. **123**, 221103 (2005).
[11] C. P. Burrows and W. L. Barnes, Opt. Express **18**, 3187 (2010).
[12] L. Zhao, K. L. Kelly, and G. C. Schatz, J. Phys. Chem. B **107**, 7343 (2003).
[13] R. W. Wood, Philos. Mag. **4**, 396 (1902).
[14] Lord Rayleigh, Philos. Mag. **14**, 60 (1907).
[15] B. Auguié, X. M. Bendaña, W. L. Barnes, and F. J. García de Abajo, Phys. Rev. B **82**, 155447 (2010).
[16] W. L. Barnes, W. A. Murray, J. Dintinger, E. Devaux, and T. W. Ebbesen, Phys. Rev. Lett. **92**, 107401 (2004).
[17] F. J. García de Abajo, Rev. Mod. Phys. **79**, 1267 (2007).
[18] B. Auguié and W. L. Barnes, Phys. Rev. Lett. **101**, 143902 (2008).

ISSN (online): 2446-1636
ISBN (online): 978-87-7210-554-3 AALBORG UNIVERSITY PRESS